Thermodynamic Modeling of a ^{3}He-^{4}He Cold Cycle Dilution Refrigerator

by

Bryant W. Mueller

A thesis submitted in partial fulfillment of

the requirements for the degree of

Master of Science

(Mechanical Engineering)

at the

UNIVERSITY OF WISCONSIN – MADISON

2012

Approved:

Franklin K. Miller, Assistant Professor (Advisor)	Date
John M. Pfotenhauer, Professor (Co-Advisor)	Date

Abstract

Sub-Kelvin refrigeration cycles are critically important for astrophysics space missions that rely on particle detection to study the nature of the universe. Devices built to observe such particles must operate at sub-Kelvin temperatures in order to achieve the resolution necessary to measure the relatively small particle energy with useful accuracy. One existing method for attaining sub-Kelvin temperatures is helium dilution refrigeration – a continuous cooling cycle relying on the endothermic mixing of two helium isotopes, ^{3}He and ^{4}He, that occurs at temperatures less than 860 mK. The topic of this thesis, a proposed modified version of the traditional helium dilution cycle, termed the *cold-cycle* ^{3}He-^{4}He dilution refrigerator, attempts to overcome limitations of the existing cycle by replacing and altering several key components in an effort to improve the thermodynamics and reliability of the machine. This work investigates the design, feasibility, and performance of the proposed cold-cycle ^{3}He-^{4}He dilution refrigerator as a method to provide sub-Kelvin cooling for space applications. To accomplish this, a thermodynamic model of the cold cycle ^{3}He-^{4}He dilution refrigerator is developed in this thesis and used to predict the cooling capacities and temperatures for multiple sets of refrigerator design parameters and operating set points. Proof-of-concept simulations completed using this model estimate that 80 μW of cooling capacity can be achieved at a temperature of 100 mK, while a minimum temperature of about 50 mK is attainable at no cooling load.

Acknowledgements

I would like to first thank my thesis advisor, Professor Franklin Miller, for the opportunity to work on this project and for the thoughtful guidance he provided throughout. Working with ^{3}He-^{4}He dilution refrigerators has been a unique, challenging, and rewarding experience just as you explained it would be in our first meeting. Professor John Pfotenhauer, my co-advisor for this project, is also deserving of my gratitude; always asking thought-provoking questions, he has been an invaluable resource as I learned about helium cryogenics. I also thank Professor Sandy Klein, the third member of my thesis committee, for not only his willingness to serve on the committee but also for the excellent experience I had in his thermodynamics courses – it is in no small part due to his energetic and informative undergraduate lectures that I decided to pursue the thermal sciences and work in the Solar Energy Lab for my graduate studies. Additionally, I thank Professor Kevin Turner for providing multiple undergraduate research opportunities that led me onward to graduate school, and Professor Jaal Ghandhi for his help and suggestions during the time I was a teaching assistant for his course.

I thank my parents, Wayne and Nancy, for their support throughout my entire educational career, and my older sister Heidi for providing ample motivation for me to succeed in school by setting such high academic standards. I also thank my grandparents – Roger, Joyce, Wallace, and Bernice – for their endless encouragement as I pursued both of my collegiate degrees. I also must thank my colleagues in the Solar Energy Lab – Amir Jahromi, Dan Shick, Dan Potratz, Rodrigo Barazza, and Soenke Teichel – for our many stimulating discussions (and shared agonies with EES and Matlab). I emphasize my thanks to Amir – he has been immensely helpful in explaining

the bizarre behavior of superfluid helium and, with his experimental background in helium cryogenics, challenging or supporting my many modeling ideas with real experimental evidence.

Finally, I greatly appreciate the financial the support of the University of Wisconsin Mechanical Engineering Department for providing funding for my work through the Alexander Cowie Fellowship and a teaching assistant appointment.

Table of contents

List of figures

List of tables

Nomenclature

B	Magnetic field strength (Tesla)
$C_{\mu 4}$	Molar specific heat capacity at constant ^{4}He chemical Potential (J/K-mol-^{3}He)
C_{p3He}	Molar specific heat capacity of ^{3}He at constant pressure (J/K-mol-^{3}He)
D, d	Diameter (mm)
D_h	Hydraulic diameter (mm)
E	Photon energy (J)
E_{BP}	Bandpass energy (J)
ΔE	Photon energy resolution (J)
g	Molar specific Gibb's free energy (J/mol-^{3}He)
h_{os}	Osmotic enthalpy (J/mol-^{3}He)
h	Molar specific enthalpy (J/mol-^{3}He)
k	Thermal conductivity (W/m-K)
L	Length (m)
MM	Molar mass (mol/g)
n	Number of moles (mol)
Nu	Nusselt number (-)
$\dot{n}_{3He}$	^{3}He molar flow rate (mole-^{3}He/s)
$\dot{n}_{4He}$	^{4}He molar flow rate (mole-^{4}He/s)
P	Pressure (kPa)
ΔP	Superleak pressure difference (kPa)
$\dot{Q}$	Heat transfer rate (W)
S	Entropy (J/K)
s	Molar specific entropy (J/K-mol-^{3}He)
$\dot{S}_{gen}$	Entropy generation rate (W/K)
T	Temperature (K)
t	Time (s)
t_{pump}	Pump period (s)
$th_{wall,psc}$	Phase separation chamber wall thickness (mm)
u	Molar specific internal energy (J/mol-^{3}He)
U	Internal energy (J)
UA	Heat transfer conductance/area product (W/K)
V	Volume (m^3)
x	^{3}He molar concentration (mol-^{3}He/mol-He) or (-)
v	Molar specific volume (m^3/mol)
y	Axial heat exchanger position (m)

γ	GGG porosity or void volume (-)
μ_{4He}	^{4}He chemical potential (J/mol-^{4}He)
ρ	Density (kg/m^3)
σ	Stefan-Boltzmann constant (W/m^2-K^4)

1 Introduction

Sub-Kelvin refrigeration cycles are critically important for astrophysics space missions that rely on particle detection to study the nature of the universe. Devices built to observe such particles must operate at sub-Kelvin temperatures in order to achieve the resolution necessary to measure the relatively small particle energy with useful accuracy. One existing and well established method for attaining sub-Kelvin temperatures is helium dilution refrigeration – a continuous cooling cycle relying on the endothermic mixing of two helium isotopes, ^{3}He and ^{4}He, that occurs at temperatures below 860 mK. Traditional helium dilution refrigeration, however, has several limitations that severely restrict its use for space applications. The topic of this thesis, a proposed modified version of the helium dilution refrigerator termed the *cold-cycle* ^{3}He-^{4}He dilution refrigerator, attempts to overcome these limitations by replacing several key components in the tradition dilution refrigerator design to improve the thermodynamics and reliability of the machine. This work investigates the design, feasibility, and performance of this proposed cold-cycle ^{3}He-^{4}He dilution refrigerator as a method to provide sub-Kelvin cooling for space applications.

1.1 Motivation and applications for sub-Kelvin refrigeration

State-of-the-art particle sensing equipment used in X-ray astrophysics space missions must be cooled to sub-Kelvin temperatures for accurate detection of single, incident photons. One type of cryogenic sensor used for this purpose is called a microcalorimeter, which measures energy changes using solid state semiconducting devices via the same principle as a more typical room temperature calorimeter, but on a much smaller scale (Deiker 1998). A schematic of a simple microcalorimeter is shown in Figure 1-1, which consists of an absorber plate, a thermometer, and

a weak thermal link connecting the plate to a platform maintained at a constant sub-Kelvin temperature.

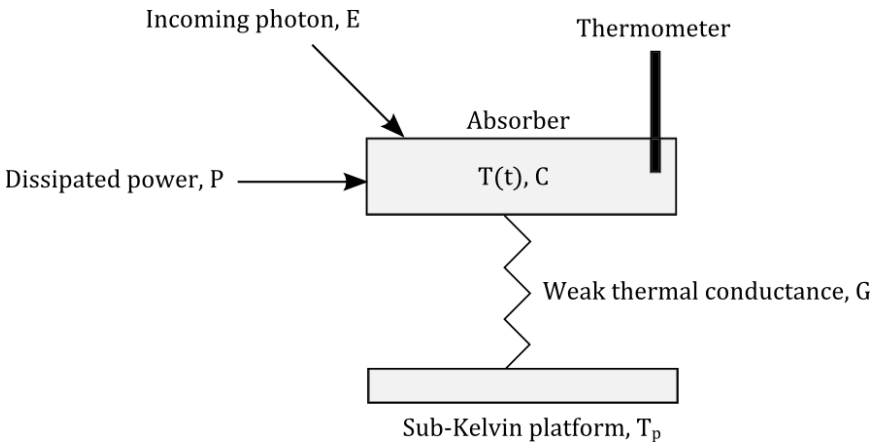

Figure 1-1: Schematic of a simple microcalorimeter adapted from ECAL-MIT (2009)

The microcalorimeter measures the energy of an incoming photon as follows. When an incoming photon strikes the absorber plate, its energy raises the internal energy of the plate, causing an increase in the absorber plate temperature. A sensitive thermometer then measures this temperature rise before the energy is transferred to the sub-Kelvin platform through the weak thermal link. Once the absorber plate is cooled back to the sub-Kelvin platform temperature it is ready to receive another photon for measurement. This process can be described by applying the first law to the absorber plate

$$C\frac{dT}{dt} = P - G\big(T(t) - T_p\big) + E\delta(t) \tag{1.1}$$

where C is the heat capacity of the absorber, $T(t)$ is the temperature of the absorber, P is the power dissipated in the absorber, G is the conductance of the weak thermal link, T_p is the sub-Kelvin platform temperature, E is the energy of the of the incident photon at the initial time, and

$\delta(t)$ is the step function in time (ECAL-MIT 2009). Solving this differential energy balance allows the incoming photon energy to be determined from the transient temperature history of the absorber plate following a proton collision, assuming the sub-Kelvin plate temperature and material properties are known.

A microcalorimeter must be designed specifically for both the maximum photon energy level, known as the bandpass, and energy resolution required for the application of interest. X-ray energy levels fall in the range of 0.1 keV and 10 keV, so a typical bandpass for such an application might be 10keV – the upper limit of this range (ECAL-MIT 2009). The measurement uncertainty of the microcalorimeter is an equally important design parameter for the calorimeter, estimated as

$$\Delta E = 2.35\sqrt{4\sigma\, T_p E_{BP}} \tag{1.2}$$

where ΔE is the energy resolution, σ is the Stefan-Boltzmann constant (5.67 x 10^{-8} W/m^2-K^4), T_p is the sub-Kelvin platform temperature, and E_{BP} is the bandpass energy (ECAL-MIT 2009). For a constant bandpass, it is easily seen that lower sub-Kelvin platform temperatures result in less measurement uncertainty and thus energy resolution. It is therefore of interest to drive the temperatures of the absorbers as low as possible in order to increase the resolution of the sensors. Figure 1-2 shows that an 80 percent improvement in energy resolution can be attained at a bandpass of 10 keV by lowering the temperature of the absorber from the outer space background temperature of 2.7 K, where the energy resolution is 7.2 eV, to 100 mK, where the energy resolution is 1.4 eV.

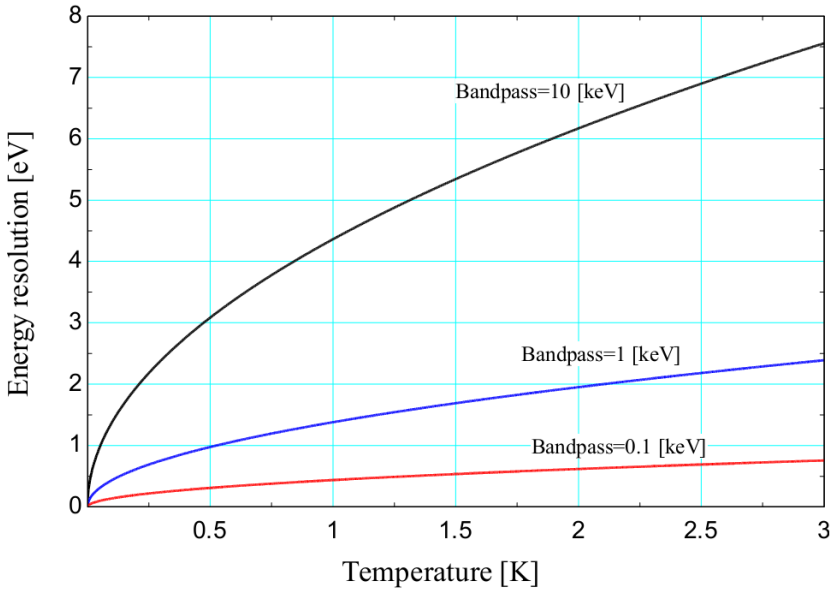

Figure 1-2: Microcalorimeter energy resolution as a function of temperature for constant bandpass energies (Jahromi 2011)

In addition to maintaining low microcalorimeter temperatures to achieve high energy resolutions, it is also desirable to maximize the available cooling capacity at this low temperature. Doing so allows multiple single photon microcalorimeter sensors to be compiled onto a single array, essentially forming a camera with each microcalorimeter acting as a single pixel. Figure 1-3 is an image of such an array, built by NASA, comprised of 64 individual microcalorimeters (ECAL-MIT 2009). Increases in the cooling power provided by the refrigeration cycle that maintains the sub-Kelvin platform temperature correspond directly to increases in the density of microcalorimeters in the arrays – since more sensors require more heat removal – and in turn allow more detailed X-ray images to be captured for previously-mentioned astrophysics experiments.

Figure 1-3: An 8x8 array of 250μm^2 single photon microcalorimeters (ECAL-MIT 2009)

For the application of maintaining sub-Kelvin temperatures for microcalorimeter photon sensors, it is clear that a sub-Kelvin refrigerator should have two main goals – minimizing the lowest attainable temperature, and maximizing the cooling capacity at this low temperature. The cold cycle ^{3}He-^{4}He dilution refrigerator investigated in this thesis aims to improve on both of these fronts in comparison to traditional helium dilution refrigerators and other comparable cryogenic refrigeration cycles, with hopes to allow larger arrays of high resolution photon sensors to be successfully operated.

1.2 ^{4}He

Before discussing the thermodynamics of ^{3}He-^{4}He solutions and their application to helium dilution refrigerators, it is worthwhile to review the pure fluid properties of the individual helium isotopes comprising the mixture. ^{4}He is by far the most abundant, stable isotope of helium existing on Earth and will therefore be discussed first.

1.2.1 Phase diagram

^{4}He is a light, colorless, and odorless gas at room temperature that occurs naturally due to radioactive decay of elements within Earth's crust, even though its density is too low to be bound to the atmosphere. Because it can easily escape the atmosphere, ^{4}He is obtained almost exclusively from natural gas wells, where it occurs in concentrations of up to 7 percent (Enss 2005). ^{4}He has the lowest critical point of the common cryogenic liquids, at 5.2 K, which can be observed on its pressure-temperature phase diagram shown in Figure 1-4.

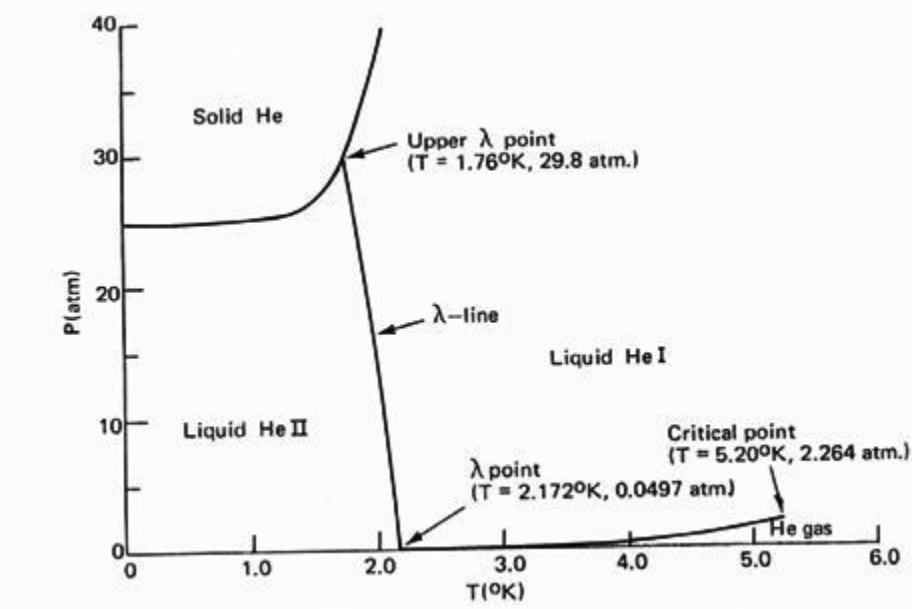

Figure 1-4: Phase diagram for ^{4}He in pressure-temperature space (University of Alaska – Fairbanks Physics Department 2011)

Liquid helium can exist in one of two phases at a given pressure below 25 atm, depending on the degree of subcooling. These two liquid phases can be observed in the phase diagram, labeled as He I and He II. The higher temperature phase – He I – is a viscous Newtonian fluid that can be described like most typical inorganic cryogenic or room temperature fluids. From this point forward, a liquid of this phase type – that is, one characterized by finite viscosity – will be

referred to as a ‘normal’ fluid. Decreasing the temperature of liquid He I past the so-called lambda temperature, which varies nearly linearly between 2.177 K and 1.78 K depending on the pressure, causes a change in phase to the other liquid phase of ^{4}He known as He II.

^{4}He demonstrates remarkably strange properties within this cold temperature He II phase due the macroscopic manifestation of quantum effects, known as Bose-Einstein condensation (Enss 2005). Of these peculiar properties, the most important in terms of cold cycle dilution refrigeration is the rapid loss of viscosity with decreasing temperature; at temperatures below about 1.8 K, the viscosity of He II can be considered negligible in comparison to that of a normal fluid He I (Jahromi 2011 and Enss 2005). This lack of viscosity has earned the He II phase the title of a superfluid, and is analogous to the loss of electrical resistance in a superconducting material. With negligible viscosity, He II can flow easily through very small capillaries and narrow channels that are impassible by a normal viscous fluid at the same temperature. Such a phenomenon is exploited by the cold cycle helium dilution refrigerator as a mechanism to efficiently separate the helium isotopes while keeping the solution in a liquid state. The other important characteristic of He II is its negligible resistance to heat transport. The apparent thermal conductivity of He II is orders of magnitude higher than common metals at room temperature, and has been estimated to be as high as 100 kW/m-K (Van Sciver 1986). Due to its extremely low resistance to heat transfer, measureable temperature gradients in a bath of pure He II cannot be developed experimentally. Such high values of effective thermal conductivity have obvious effects on the design of heat exchange equipment for sub-Kelvin refrigeration systems.

1.2.2 Two fluid model for liquid ^{4}He

The transition from normal fluid He I to superfluid He II does not occur in a stepwise event when traversing the lambda temperature. Instead, the lambda point marks the highest temperature at which ^{4}He exhibits any sign of superfluidity, with the superfluid effects increasing exponentially as the temperature is suppressed further from the lambda point. Microscopically, this behavior is caused by an increasing amount of the helium 'condensing' into its lowest energy level as the temperature approaches absolute zero, as described by Landau (1941). Macroscopically, this effect can be described by the two fluid model developed by Tisza (1938), which states that the He II density can be determined by modeling the phase as a two fluid mixture of pure superfluid and pure normal fluid, even though He II is actually a single phase of pure ^{4}He. The mass density ratios of the superfluid and normal fluid components predicted by the two fluid model are shown in Figure 1-5.

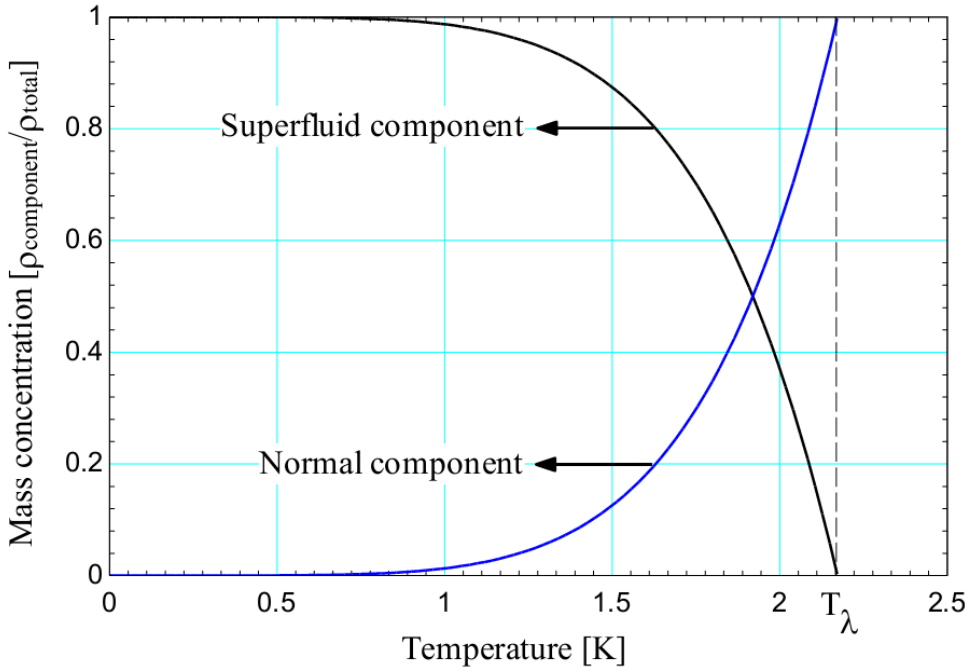

Figure 1-5: Mass concentration of superfluid and normal fluid components below the lambda temperature predicted by the two fluid model (Jahromi 2011)

From the figure, it can be seen that He II behaves completely as a superfluid at absolute zero and exponentially transitions to normal fluid behavior starting around 1 K, with the transition complete at the lambda temperature of 2.177 K. Note that the below 1 K, He II essentially behaves as a pure superfluid.

1.2.3 Superleaks

Superfluid ^{4}He, as previously mentioned, has the ability to easily flow through narrow channels and capillaries as a result of its negligible viscosity. The minimum channel diameter required for flow of superfluid ^{4}He is on the scale of nanometers, through which a normal viscous fluid cannot pass when subjected to the low pressure differentials developed in a cold cycle helium dilution refrigeration cycle. Such a device is termed a superleak, owing to the fact that only superfluids can pass through them, and can be constructed practically by securing a plug of porous glass using epoxy within a circular tube (Miller 2005). Superleaks of this form play a critical role in the cold cycle dilution refrigerator modeled in this thesis due to their ability to block the passage of normal fluid while maintaining flow of superfluid.

1.2.4 Fountain effect

Another unique phenomenon that occurs in the He II phase and is critical for the operation of a cold cycle dilution refrigerator is the fountain (or thermomechanical) effect, which directly couples temperature and pressure differences imposed over a superleak. To best understand this effect, observe the experiment depicted in Figure 1-6.

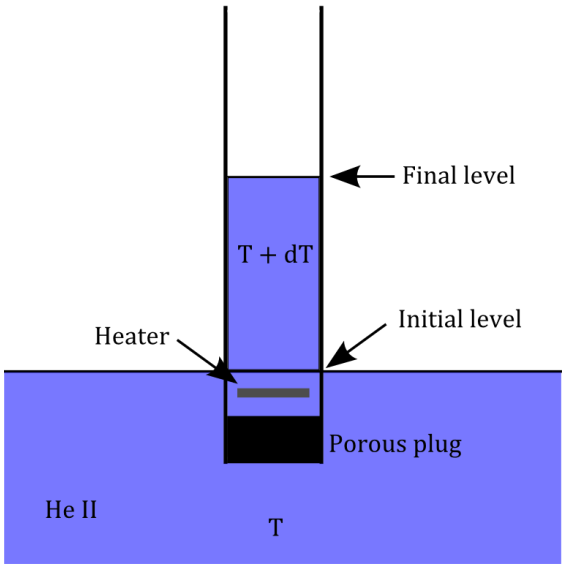

Figure 1-6: System demonstrating the fountain effect in pure He II

The setup consists of a tube, plugged on one end with a superleak made of porous glass, partially submerged in a He II bath held at constant temperature. A resistance heater is also contained within the tube, submerged in the helium. Initially, the superleak allows the helium level inside the tube to equilibrate to the same level of the surrounding bath. If a temperature gradient is imposed over the superleak by heating the helium within the tube using the resistance heater, however, some portion of the superfluid in the tube is 'converted' to normal fluid as it warms to a higher temperature, as stated by the two fluid model. Since superfluid flows to balance gradients in the superfluid 'concentration' of the two fluid 'mixture', superfluid helium travels through the superleak, from the colder surrounding bath into the tube, when the temperature of the helium in the tube increased (NASA 2004). This results in a change in level within the tube, since the normal component is too viscous to flow back through the superleak. If sufficient heat is supplied in the tube, the pressure will rise such that helium is ejected from the opening at the top of the tube, creating the fountain for which the effect is named. The cold cycle dilution

refrigerator modeled in this thesis makes use of this effect to pump the helium working fluid through the refrigeration cycle without the need for moving parts.

1.3 ^{3}He

The other mixture component required for helium dilution refrigeration – ^{3}He – is also a stable isotope, just like ^{4}He. It differs in that it has one less neutron, and exists naturally on Earth in much smaller quantities than ^{4}He. A typical sample of naturally occurring terrestrial helium contains less than one percent ^{3}He (NASA 2004), a concentration too small to practically isolate ^{3}He from naturally occurring helium reserves. Useful supplies of ^{3}He are obtained for laboratory and commercial uses through the nuclear decay of products from fission reactors or hydrogen bombs (Enss 2005). As a prerequisite for discussing solutions of ^{3}He and ^{4}He, it is necessary to understand some of the key thermodynamic differences between the two pure isotopes at the temperatures and pressures required for dilution refrigeration operation.

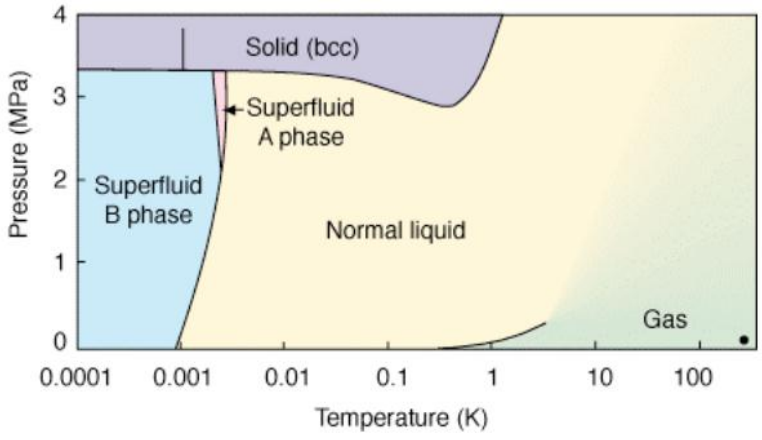

Figure 1-7: Phase diagram for ^{3}He in pressure-temperature space (Chalmers University of Technology 2011)

The phase diagram for ^{3}He, shown in Figure 1-7, is quite different from that of ^{4}He (shown previously in Figure 1-4) over the same temperature range. First, note that the critical point of ^{3}He, occurring at 3.2 K, is about 2 K lower than that of ^{4}He. Secondly, superfluid phases of ^{3}He do not exist at temperatures higher than about 1 mK, a much lower temperature than the 2.177 K needed for ^{4}He to transition into its superfluid phase. For refrigeration systems that cool only to around 50 mK – such as the cold cycle dilution refrigerator in this work – ^{3}He exists only as a normal fluid. This has implications for the design of the refrigerator components. For example, because ^{3}He is a normal viscous fluid, it cannot penetrate superleaks at temperatures below the ^{4}He lambda temperature. In mixtures of ^{3}He and ^{4}He then, superleaks can be utilized to block both the flow of ^{3}He and the normal component of ^{4}He while allowing the superfluid component of ^{4}He to pass through unimpeded. This ability to restrict passage of normal fluid ^{3}He via superleaks is critical for the operation of the cold cycle dilution refrigerator, as will be illustrated in upcoming sections.

Along with its large viscosity in comparison to superfluid ^{4}He, ^{3}He has a finite thermal conductivity associated with a normal fluid, whereas the superfluid ^{4}He thermal conductivity is effectively infinite at temperatures below the ^{4}He lambda temperature. These large discrepancies in thermal conductivity affect the performance and design of heat exchangers that deal with transferring thermal energy between streams of normal fluid ^{3}He and superfluid ^{4}He. As with the viscosity effects already discussed, such circumstances occur within the cold cycle dilution cycle that is the topic of this work and must be considered in the design of the refrigerator.

1.4 ^{3}He-^{4}He mixtures

With the properties of the individual constituents now introduced, the thermodynamics of ^{3}He-^{4}He mixtures – the working fluid for the cold cycle dilution refrigerator studied in this work – can be properly discussed. ^{3}He-^{4}He mixtures fall into the category of binary mixtures, named to reflect the fact that there are only two pure fluid components comprising the mixture. In addition to the two intensive properties that are needed to fix the thermodynamic state of a single phase pure fluid, a binary mixture requires a third property – typically the molar concentration of one of the mixture components within the overall mixture – to fix the state of the system. For ^{3}He-^{4}He mixtures, it is common to use the molar concentration of ^{3}He for this purpose. At temperatures below the lambda point of pure ^{4}He, mixtures of these helium isotopes exhibit many interesting properties owing to the fact that one of the components is a superfluid in its pure form while the other is not.

Mixtures of ^{3}He-^{4}He are most commonly defined thermodynamically by a phase diagram with coordinates of temperature and ^{3}He molar concentration on a plane of constant (zero) pressure. Figure 1-8 shows this phase diagram, also referred to as a T-x plot, constructed using the Chaudhry (2009) equation of state. There are several important features to note on the diagram. First, the mixture is a liquid over the entirety of the plotted temperature range, with the ^{3}He molar concentration varying from zero on the left vertical axis – indicating pure ^{4}He – to unity on the right vertical axis – indicating pure ^{3}He. There are three distinct regions on the diagram, each corresponding to a different phase of the liquid mixture, that behave quite different thermodynamically.

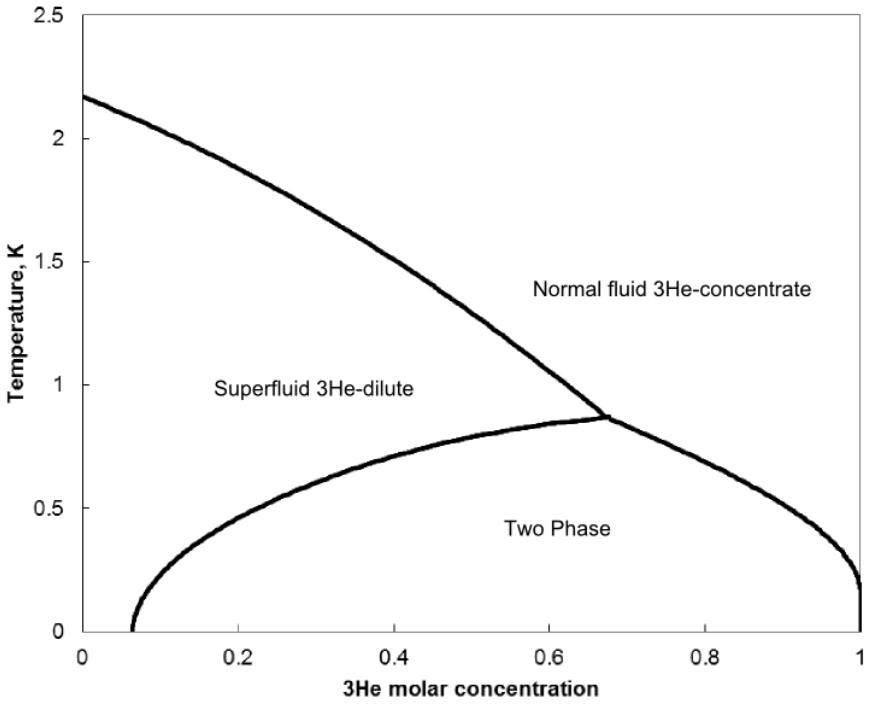

Figure 1-8: ^{3}He-^{4}He phase diagram in temperature-^{3}He molar concentration space on a plane of constant (zero) pressure

At high concentrations and high temperatures, the mixture is a normal viscous fluid in what is called the normal fluid ^{3}He-concentrate phase. This phase extends from the lambda point of pure ^{4}He (T=2.177 K, x=0) almost linearly to the tricritical point (T=0.867 K, x=0.674). On the left side of the lambda line is the superfluid ^{3}He-dilute phase. This phase can essentially be described as ^{3}He gas suspended in an inert background of liquid ^{4}He in its superfluid He II phase. Like pure ^{4}He in its superfluid phase, it has negligible viscosity compared to the normal fluid ^{3}He-concentrate phase existing on the other side of the lambda line. Unlike pure ^{4}He superfluid in the He II phase, however, the thermal conductivity is not always effectively infinite but rather a strong function of the ^{3}He molar concentration. This dependence of thermal conductivity on the ^{3}He molar concentration will be addressed when analyzing the heat exchangers later in this work.

The last remaining region on the phase diagram is the two phase region, which is critical for the operation of dilution refrigerators. This region occurs at temperatures below the tricritical temperature, bounded by the dilute saturation curve on the left and the concentrate saturation curve on the right. Unlike the superfluid and normal fluid phases already described, this region does not contain a third unique phase. Instead, a mixture at a temperature below the tricritical point whose ^{3}He molar concentration lies within the two phase region separates into a normal fluid ^{3}He rich phase and a superfluid ^{3}He poor phase, whose ^{3}He molar concentrations are defined by the concentrate and dilute saturation curves at the temperature of the mixture, respectively. These two phases are immiscible and can be separated by buoyancy when in a gravitational field due to small differences in densities or by differences in surface tension when in microgravity. The transfer of ^{3}He atoms at constant temperature across this miscibility gap from the ^{3}He-concentrate phase to the ^{3}He-dilute phase is an endothermic process, analogous to evaporating a pure fluid at constant temperature. Such processes require an input of thermal energy to succeed. Helium dilution refrigerators take advantage of this mechanism to provide cooling at temperatures below the tricritical point. Since the ^{3}He-dilute phase exists even at absolute zero if concentrations are less than about 6.5 percent, dilution refrigeration can theoretically be used to reach temperatures approaching absolute zero (Radebaugh 1967).

Although the phase diagram shown in Figure 1-8 is valid only for a plane of constant (zero) pressure, it can be used to find thermodynamic properties at other mixture pressures because lines of constant ^{4}He chemical potential in the zero pressure plane represent the intersection lines, projected back to the plane of zero pressure, of a constant ^{4}He chemical potential surface with planes of higher pressure. Figure 1-9 illustrates this relationship between the zero pressure

lines of constant ^{4}He chemical potential and the projected intersection lines of constant ^{4}He chemical potential surfaces with higher pressure planes back onto the zero pressure T-x diagram.

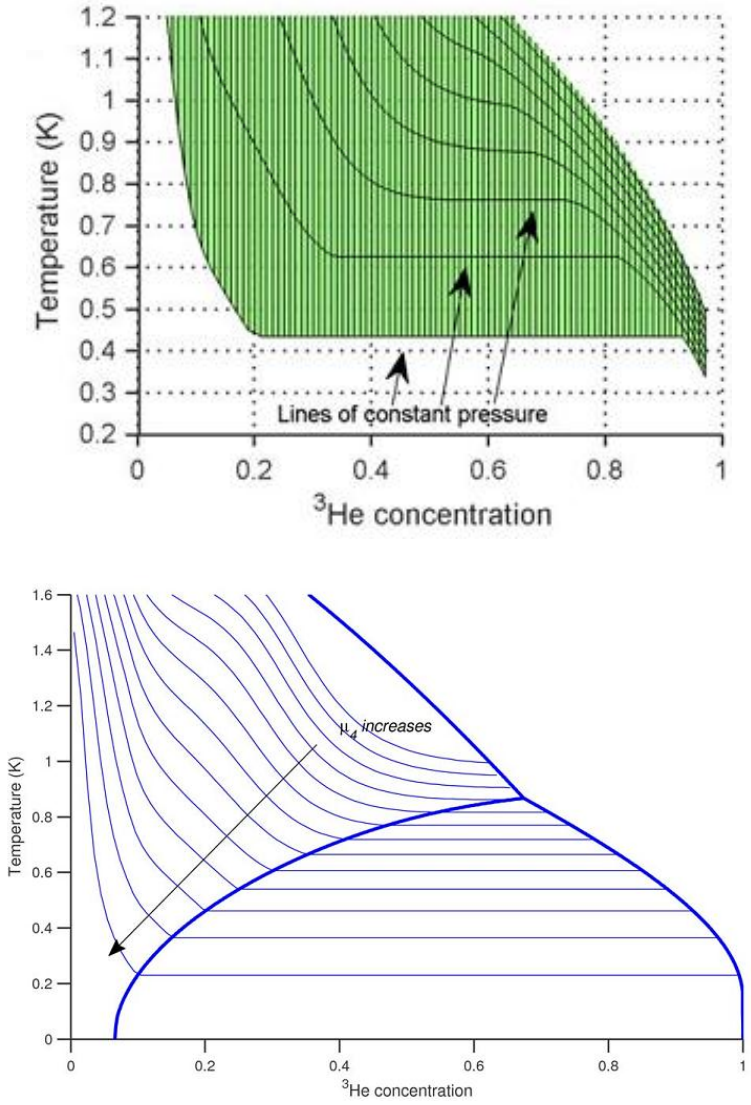

Figure 1-9: (a) the zero pressure T-x diagram with a projected surface of constant ^{4}He chemical potential shown in green and lines of constant pressure indicated and (b) the zero pressure T-x diagram showing lines of constant ^{4}He chemical potential (Chaudhry 2009)

Figure 1-9a shows a surface of constant ^{4}He chemical potential (in green) projected onto the zero pressure T-x plot. Overlaid are the intersection lines of the constant ^{4}He chemical potential surface with multiple planes of constant pressure, as projected back onto the zero pressure T-x

plane. Figure 1-9b also shows the zero pressure T-x diagram, in this case with lines of constant ^{4}He chemical potential at zero pressure overlaid. It can be seen by comparing Figures 1-9a and 1-9b that lines of constant ^{4}He chemical potential in the zero pressure T-x plane coincide with unique constant pressure intersections on the constant ^{4}He chemical potential surface projected onto the same zero pressure T-x plane. Another way to look at this is that a line of constant ^{4}He chemical potential in the zero pressure T-x plane represents a projection of a *different* line of ^{4}He chemical potential at a *different* pressure back onto the zero pressure T-x plane.

The usefulness of this relationship becomes apparent when evaluating properties at the same ^{4}He chemical potential but at two different pressures, which, as will be seen in the upcoming chapters, is important for dilution refrigerator analysis. In such a case, properties at each pressure can be obtained using only the zero pressure T-x plot, with two different zero pressure ^{4}He chemical potential lines representing the projected intersections of the constant ^{4}He chemical potential surface with the two pressure planes of interest. Figure 1-10 illustrates this, showing two lines of constant pressure at constant ^{4}He chemical potential represented by two different ^{4}He chemical potential lines on the zero pressure T-x plot.

It is important to note that the projected ^{4}He chemical potential lines – as they will be referred to for the remainder of this work – in the zero pressure plane used in this analysis method do not directly represent the actual ^{4}He chemical potential at each pressure. Instead they indirectly represent different pressures on a plane of constant ^{4}He chemical potential. This method of using the T-x plot at zero pressure to estimate properties at higher pressure is used by Miller (2005), Radebaugh (1967), and others, as ^{3}He-^{4}He property data at high pressures are not available. The

model developed in this work will also apply this method to obtain ^{3}He-^{4}He properties at high pressures.

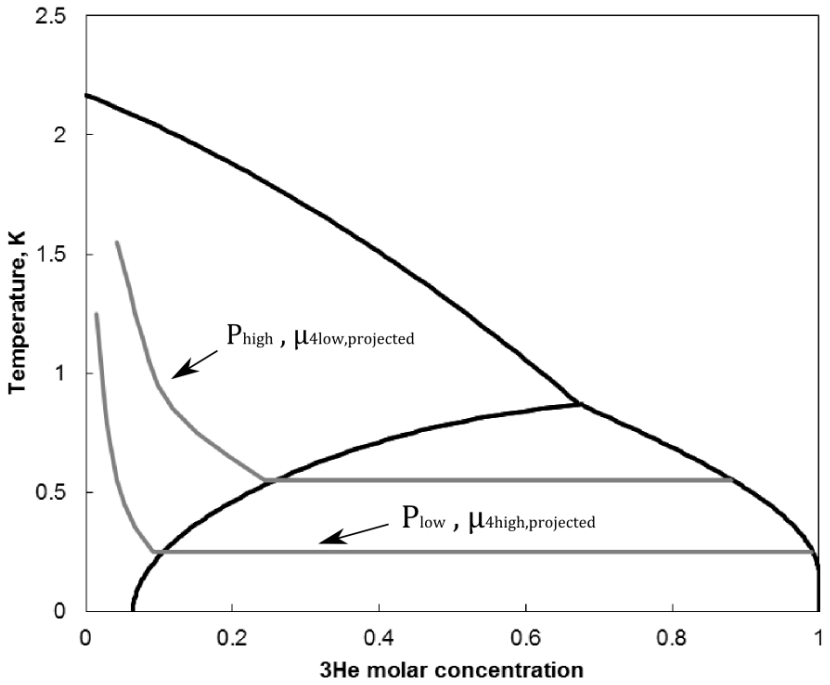

Figure 1-10: A zero pressure T-x plot showing two lines of constant pressure at the same ^{4}He chemical represented by two different zero pressure ^{4}He chemical lines

A final important topic for ^{3}He-^{4}He mixtures, which has already been briefly discussed, is the effect of the normal fluid ^{3}He present in the mixture on the pressure differential developed over a superleak. For a mixture of ^{3}He-^{4}He, the normal fluid ^{3}He component behaves similarly to the normal component of the ^{4}He – both are too viscous to pass through a superleak. Due to this, the experiment used to describe the superfluid ^{4}He fountain effect in Figure 1-6 becomes slightly more complex if a superfluid mixture of ^{3}He-^{4}He is used instead. Consider a hypothetical experiment using the same setup shown in Figure 1-6, but with a ^{3}He-^{4}He mixture as the fluid; in this new experiment, both the initial ^{3}He molar concentration and liquid level in tube is the same as in the surrounding bath. When the temperature of the mixture in the tube is increased, the liquid level in the tube rises as superfluid ^{4}He flows in through the superleak to balance the

gradient in superfluid concentration. Since the fluid is now a mixture of the two isotopes, the inflow of superfluid ^{4}He reduces the ^{3}He molar concentration in the tube because the viscous ^{3}He cannot enter through the superleak. This difference in ^{3}He molar concentration results in an additional osmotic pressure difference across the superleak that amplifies the level rise in the tube from what would be expected if using pure ^{4}He for a the same induced temperature rise. Depending on the temperature and ^{3}He molar concentrations imposed on each side of the superleak, the total resulting pressure difference can be dominated by either the fountain effect caused by the superfluid concentration differential of the ^{4}He or the osmotic pressure difference caused by the ^{3}He molar concentration differential.

1.5 Traditional ^{3}He-^{4}He dilution refrigeration

Helium dilution refrigeration, as stated previously, utilizes the endothermic mixing of the ^{3}He-concentrate and ^{3}He-dilute phases of ^{3}He-^{4}He mixtures to provide cooling at temperatures approaching absolute zero. The traditional helium dilution cycle has been around for many years, being implemented successfully for the first time by Das and De Bruyn Ouboter in 1965 (Enss 2005). The operation of the machine is best explained by following the working fluid through the cycle, stepping through the important processes. To do so requires referral to Figure 1-11, a simplified schematic of a typical traditional dilution refrigeration machine.

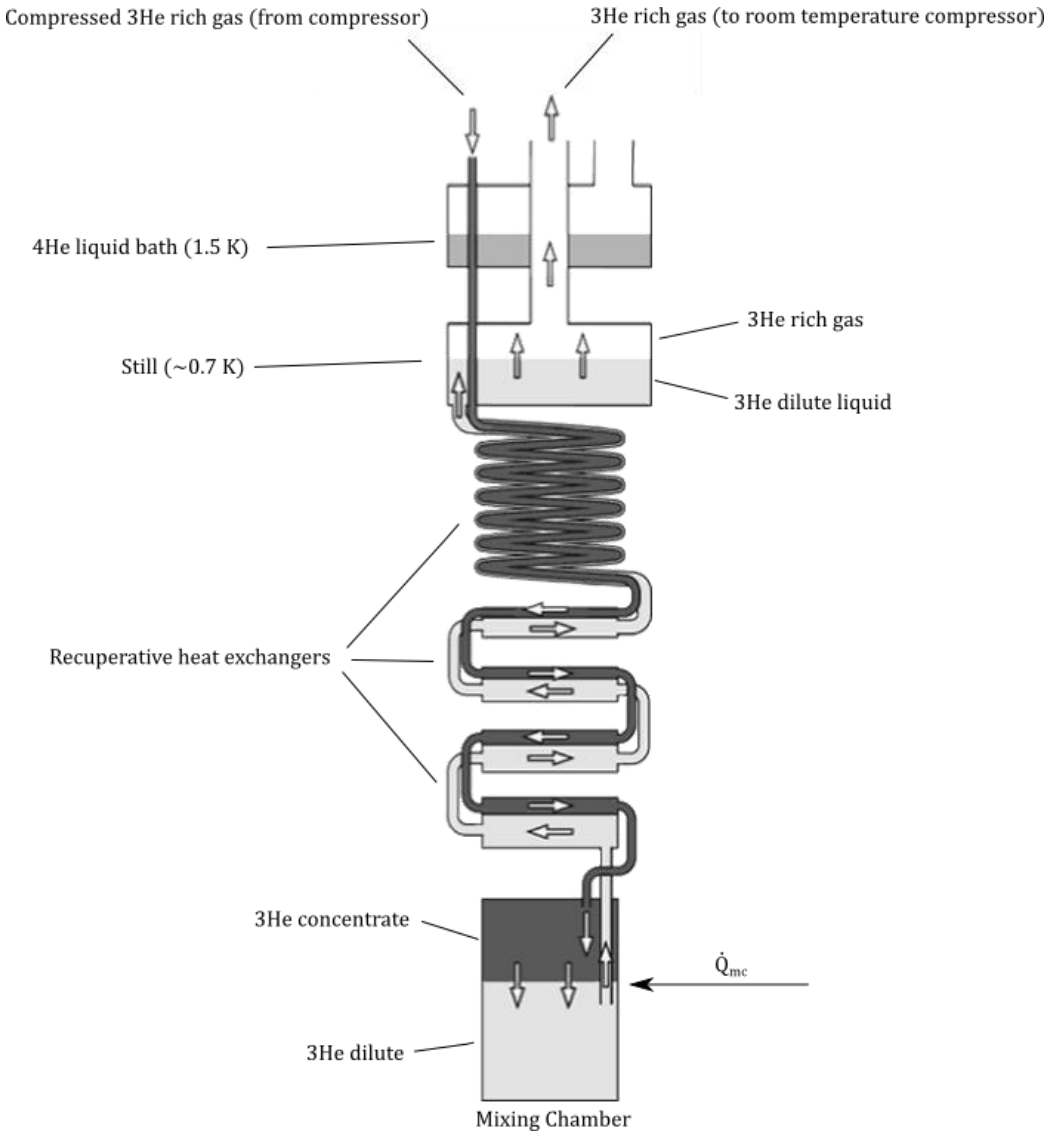

Figure 1-11: Schematic of a traditional ^{3}He-^{4}He dilution refrigerator, modified from Lancaster University Physics Department (2010) and Enss (2005)

The refrigerator depicted in Figure 1-11 operates in a continuous steady state by circulating ^{3}He throughout the machine. High pressure, ^{3}He rich gas enters the hot end of the machine from a room temperature compressor, where it expanded and condensed into a ^{3}He rich liquid (residing in the normal fluid ^{3}He-concentrate phase of the ^{3}He-^{4}He phase diagram) by dissipating thermal energy to a 1.5 K ^{4}He bath through a heat exchanger. After condensing, the ^{3}He-concentrate is subcooled by the stream returning from the mixing chamber through a series of recuperative heat

exchangers. Following the recuperators, the ^{3}He-concentrate enters the mixing chamber, where the phase of the helium mixture lies in the two phase region. Here, the lighter ^{3}He-concentrate floats on top of the heavy superfluid ^{3}He-dilute phase; atoms of ^{3}He must cross the boundary from the ^{3}He-concentrate phase to the ^{3}He-dilute phase before exiting the chamber, requiring an input of heat because this process is endothermic. After crossing the phase boundary, the ^{3}He exits the mixing chamber in the superfluid ^{3}He-dilute phase, cooling the incoming hot ^{3}He-concentrate stream as it passes through the recuperators before reaching the still. Maintained at approximately 700 mK within the still, the ^{3}He vapor preferentially evaporates from the superfluid ^{3}He-dilute liquid mixture due to its higher vapor pressure. The gas above the liquid mixture in the still is approximately 90 percent ^{3}He, which is returned to room temperature for compression before returning to the hot side of the cycle.

The dilution refrigeration cycle has many advantages that make it an attractive choice for cooling to sub-Kelvin temperatures. The cycle operates continuously, allows for higher cooling capacities than evaporative ^{3}He cooling at temperatures lower than about 300 mK, and is fairly well studied (Enss 2005). There are two main drawbacks to using this traditional dilution refrigeration cycle for space applications, however, with both relating to the compression needed to circulate the ^{3}He through the cycle. First, and perhaps most importantly, are the reliability concerns associated with a mechanical compressor aboard an unmanned space flight. Should problems develop after launch with the compressor machinery the entire refrigerator may prove useless, potentially wasting the entire cost of the mission. Secondly, typical helium dilution refrigeration requires compression of high temperature ^{3}He rich gas, consuming large amounts of power due to the large volume changes necessary to increase its pressure. This process makes

traditional helium dilution refrigeration incredibly inefficient, even for space applications where the high temperature of the gas will be much lower than room temperatures experienced by the same cycle back on Earth.

1.6 Cold cycle ^{3}He-^{4}He dilution refrigeration

The subject of this thesis – cold cycle dilution refrigeration – is a modified version of the traditional ^{3}He-^{4}He dilution refrigeration cycle which seeks to remedy the drawbacks of the latter and make helium dilution refrigeration more feasible for space applications. Cold cycle dilution refrigeration essentially makes one critical change to the traditional cycle that remedies both drawbacks mentioned previously. Instead of evaporating the ^{3}He gas, compressing it at high temperature, and condensing it past a ^{4}He bath to produce the ^{3}He-concentrate, the cold cycle machine maintains the ^{3}He-^{4}He mixture in its liquid state, making clever use of superleaks and the fountain effect to form the ^{3}He-concentrate from the ^{3}He-dilute returning from the mixing chamber. No active mechanical components are need to drive this process since the fountain effect allows pressure gradients to be developed in the liquid mixture by simply inducing temperature differences over a superleak. Such temperature gradients can be imposed by heating or cooling the helium with a paramagnetic salt, whose temperatures can be controlled by the controlled application of a magnetic field. Due to these modifications, the cold cycle dilution refrigerator does not require a still because no evaporation is not necessary, but instead requires a set of passive check valves to direct the helium flows as well as an additional chamber for the ^{3}He-concentrate phase to separate from the ^{3}He-dilute phase before entering the mixing chamber.

The details of the cold cycle dilution refrigeration cycle concept introduced here are presented in detail over the upcoming sections of this thesis, yet it is important to recap the benefits of the modified cycle as they relate to space applications before continuing. By replacing the mechanical compressor with a magnetic pump, both the reliability and thermal efficiency issues plaguing the traditional dilution refrigerator design are addressed simultaneously. A magnetic pump requires only the application of current to a superconducting magnet – a process with much less chance of failure when compared with the moving pistons or bellows of a mechanical compressor. Furthermore, since the helium mixture never enters its low density gas phase in the cold cycle machine, the cooling capacities for a given amount of pumping power should theoretically increase over the traditional design. Overcoming the reliability and efficiency issues are the key advantages of the cold cycle dilution refrigerator over the traditional dilution cycle and provide strong motivation for the model developed in this thesis.

1.7 Objective of this work

The purpose of this thesis is to develop a thermodynamic model for the proposed cold cycle ^{3}He-^{4}He dilution refrigerator that predicts performance over a range of design conditions. The goals of the model are as follows, in order of importance:

1. Prove that the cold cycle helium dilution refrigeration cycle is viable
2. Characterize the performance of the refrigerator over a range of design and operating conditions
3. Provide suggestions for the initial sizing of various refrigerator components to be used in the construction of a cold cycle dilution refrigerator prototype.

The remainder of this work will be focus on developing the model and using it to address these goals.

1.8 References

Chalmers University of Technology – Department of Microtechnology and Nanoscience website, 2011.

Chaudhry, G., Thermodynamic properties of liquid ^{3}He-^{4}He mixtures between 0.15 K and 1.8 K, Ph.D. Dissertation, Massachusetts Institute of Technology, 2009.

Deiker, S. et al., "First results from a suborbital flight of a 36 pixel microcalorimeter array", Proceedings of the 7th International Workshop on Low Temperature Detectors, 1997.

ECAL-MIT (Experimental Cosmology and Astrophysics Laboratory at the Massachusetts Institute of Technology) website, 2009.

Enss, C. and Hunklinger, S., Low temperature physics, Springer, New York, 2005.

Jahromi, A., Development of a 1 K facility and modeling of a superfluid magnetic pump with no moving parts, Master's Thesis, University of Wisconsin – Madison, 2011.

Lancaster University – Department of Physics website, 2011.

Landau, L., "The theory of superfluidity of helium II", Physical Review 60, 356-358, 1941.

Miller, F., The development of a proof of principle superfluid Joule-Thomson refrigerator for cooling below 1 Kelvin, Ph.D. Dissertation, Massachusetts Institute of Technology, 2005.

NASA Goddard Space Flight Center website, 2005.

Radebaugh, R, Thermodynamic properties of ^{3}He-^{4}He solutions with applications to the ^{3}He-^{4}He dilution refrigerator, NBS Technical Note 362, 1967.

Tisza, L., "Transport Phenomena in Helium II", Nature 141, 913, 1938.

University of Alaska – Fairbanks Physics Department website, 2001.

Van Sciver, S., Helium cryogenics, Plenum Press, New York, 1986.

2 Refrigerator design and operation

2.1 Design overview

The thermodynamic model developed in this thesis is based heavily on the cold cycle ^{3}He-^{4}He refrigerator proposed by Miller (2010), with a small number of minor modifications applied to the core design. This slightly modified version of Miller's design is sketched in Figure 2-1. A brief walkthrough of the schematic shown in Figure 2-1, given in this overview section, broadly highlights the design and purpose of the key components in the refrigerator system, while the details of the design and operation are addressed in subsequent sections of this chapter.

Driving the cold cycle ^{3}He-^{4}He dilution refrigerator – and separating the cycle from traditional ^{3}He-^{4}He dilution refrigerators – is the reversible superfluid magnetic pump. Developed previously by Miller and Brisson (2009) for use in superfluid pulse tube refrigerators that also use ^{3}He-^{4}He mixtures as the working fluid, the pump leverages the superfluid fountain effect to separate the helium isotopes and circulate the helium mixture without the need to evaporate the ^{3}He from the liquid mixture and compress it at room temperature. The pump supplies and removes heat from the helium mixture by manipulating the entropy of a paramagnetic salt, placed in excellent thermal contact with the helium, through the use of an applied magnetic field via the magnetocaloric effect. Adjacent to the pump is a set of heat exchangers that allow rejection of the load and pumping heat from the helium mixture to a precooling stage controlled at a constant temperature by upstream cryocoolers. Since the helium mixture flow rates produced by the pump oscillate in time due to finite limits on the magnitude of the magnetic field applied to the cylinders, a set of check valves is required to rectify the flow and provide a continuous directional flow of helium mixture to the remaining components in the cycle.

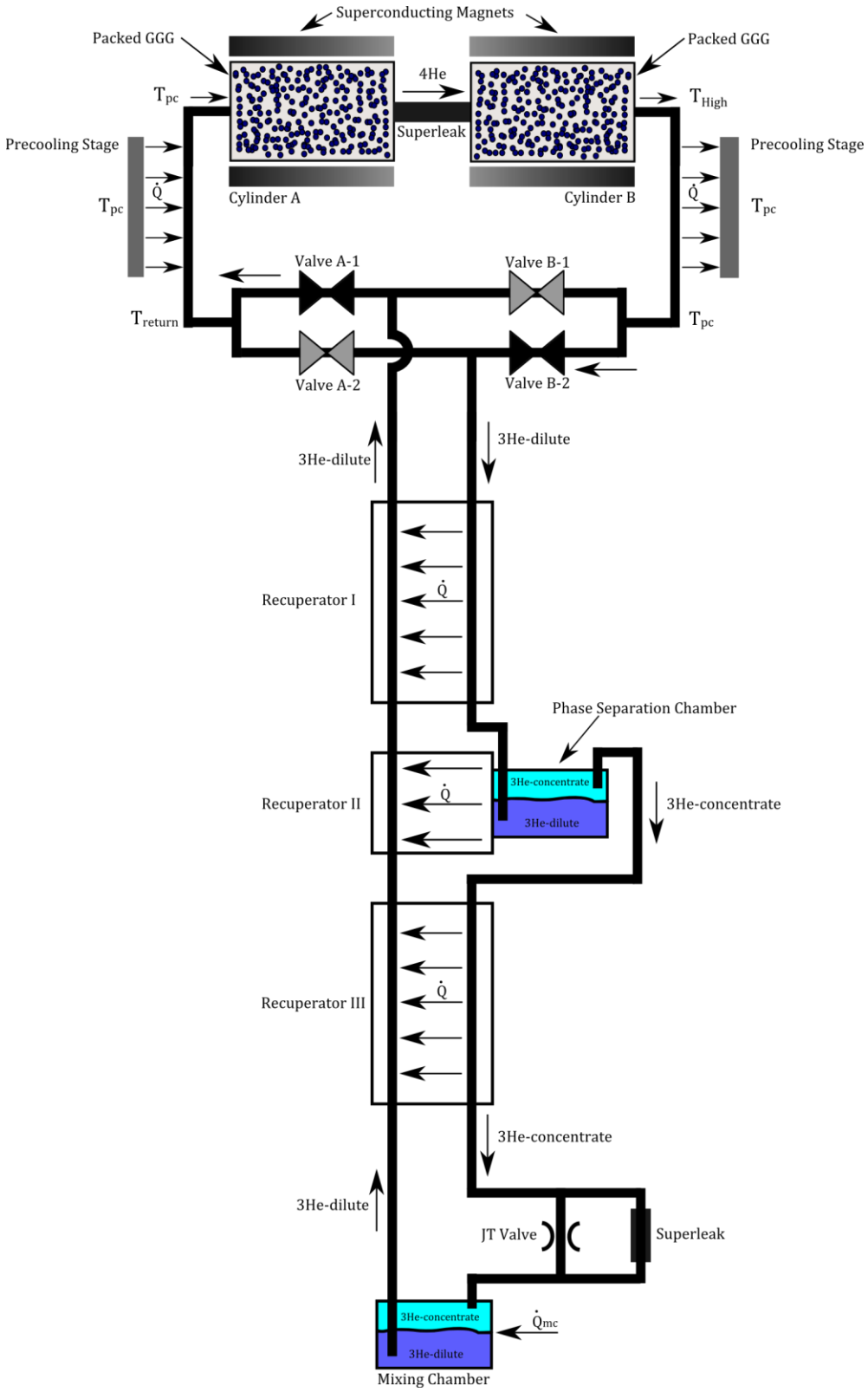

Figure 2-1: Overview schematic of the cold cycle ^{3}He-^{4}He dilution refrigerator modeled in this work. ^{3}He flow directions shown are representative of just one of four processes in the pumping cycle.

In the section of the refrigerator experiencing continuous directional flow (the loop below the four check valves in Figure 2-1), a phase separation chamber is positioned between two recuperative heat exchangers. These components serve the purpose of further increasing the ^{3}He molar concentration of the high pressure stream, entering from pump through the check valves, to the normal fluid ^{3}He-concentrate phase by cooling it using the colder low pressure stream returning from the mixing chamber. After exiting the coldest recuperator, the flow enters a Joule-Thomson valve in parallel with a superleak that expands the normal fluid ^{3}He-concentrate while maintaining constant ^{4}He chemical potential throughout the refrigerator. Downstream of the Joule-Thomson valve, the mixing chamber houses the endothermic process of mixing the incoming normal fluid ^{3}He-concentrate stream with the outgoing ^{3}He-dilute stream while facilitating the heat transfer from the external load.

2.2 Reversible superfluid magnetic pump

The reversible superfluid magnetic pump, identical to that developed previously by Miller and Brisson (2009), has a simple, elegant design that allows it to take advantage of the fountain effect to pump the mixture through the cycle and concentrate ^{3}He on the high pressure side of the refrigerator without the need for mechanical actuation. The pump physically consists of two stainless steel cylinders, each packed with spheres of a paramagnetic salt, connected together via a superleak made from porous Vycor glass. Superconducting coils wrapped around the exterior of the cylinders allow a controllable magnetic field to be applied to the paramagnetic salt contained within. Each cylinder also has a port to either supply or remove helium mixture to the check valve network, depending on the process in the pumping cycle. Figure 2-2 is a detailed schematic of this pump design.

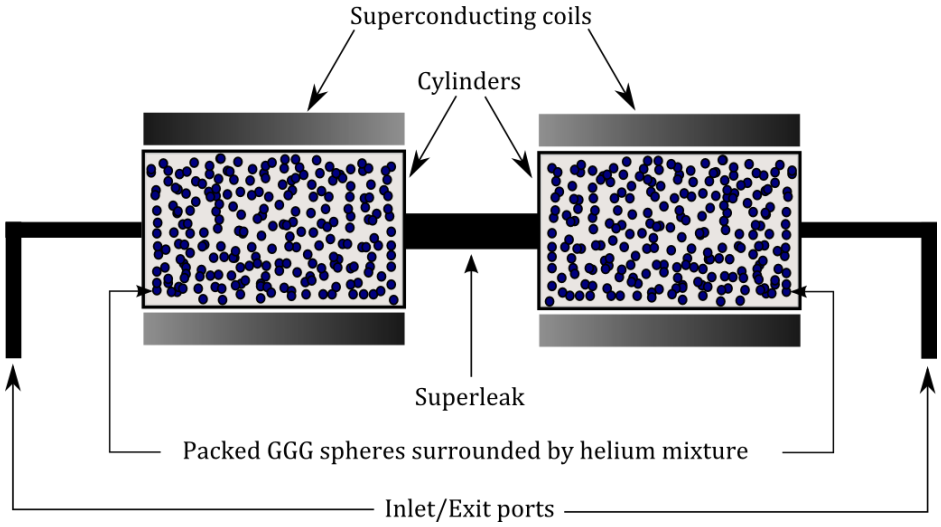

Figure 2-2: Detailed schematic of the reversible superfluid magnetic pump

To develop a pressure differential over the superleak via the fountain effect, a temperature differential must be imposed by raising the temperature in one cylinder relative to the temperature in the other. The magnetocaloric effect – that is, the dependence of the paramagnetic salt entropy on the applied magnetic field as well as on the temperature – is employed to induce this temperature differential between the cylinders. The paramagnetic salt gadolinium gallium garnet (GGG) is used for the pump design in this work because its thermodynamic properties are known at the temperatures and applied magnetic field strengths expected for typical operating conditions of the cold cycle dilution refrigerator. For the remainder of this work, the salt will be referred to simply as "GGG". To better illustrate the dependence of entropy on the applied magnetic field for a magnetocaloric material, Figure 2-3 shows the entropy of GGG as a function of applied field strength for several values of temperature.

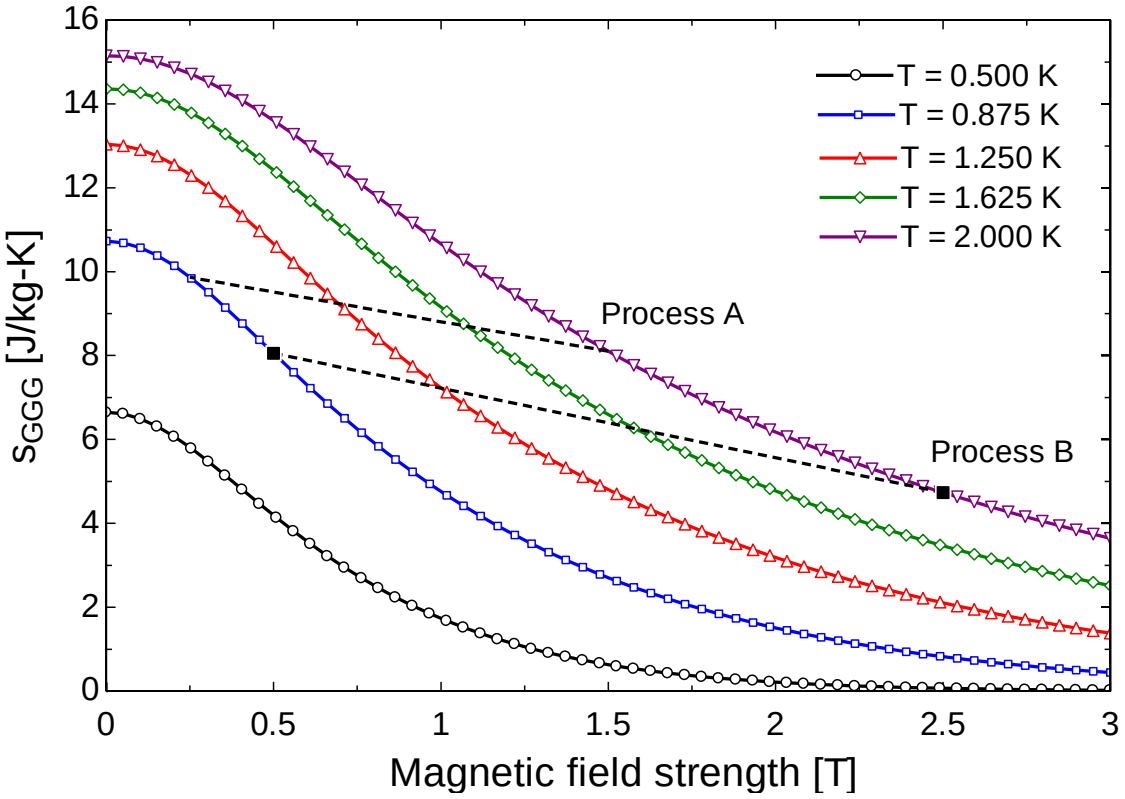

Figure 2-3: Gadolinium gallium garnet (GGG) entropy as a function of applied field strength at temperatures relevant to cold cycle dilution refrigeration operation. Based on the Lounasmaa (1974) general equation of state for paramagnetic salts.

Two example processes, relevant to the superfluid magnetic pump, are overlaid on the property plot. Process A illustrates a decrease in GGG entropy and increase in temperature resulting from an increase in magnetic field strength while process B shows an increase in GGG entropy and decrease in temperature resulting from a decrease in magnetic field strength. The former requires heat transfer *out of* the GGG while the latter requires heat transfer *into* the GGG, as shown in Equation 2.1. This equation applies the second law to a closed system containing a mass of GGG, with the reversible heat transfer defined as positive for flows out of the system.

$$Q = -TdS_{GGG} \tag{2.1}$$

If Equation 2.1 is applied to a system of GGG spheres contained in a pump cylinder and the cylinder walls are assumed to be perfect insulators, the heat transfer is then exclusively with the ^{3}He-^{4}He mixture surrounding the spheres within the cylinder. Since there is excellent thermal contact between the GGG and the helium due to both the large heat transfer area provided by the small diameter spheres and high thermal conductivity of the superfluid liquid, temperature gradients between the GGG and helium mixture are negligible for such processes at the rates of magnetic field change of interest for this pump (Miller 2009). It follows that the temperature of the helium mixture tracks the temperature of the GGG instantaneously in time for such processes. Control of the GGG entropy in each cylinder with independent applied magnetic fields therefore allows the pump to develop a temperature difference across the superleak by heating the helium mixture and GGG in one cylinder through an *increase* in its applied magnetic field strength while simultaneously cooling the mixture and GGG in the opposing cylinder by a *decrease* in its applied magnetic field strength.

Although it is rather straightforward to deduce that the pressure gradient developed over the superleak can be used to circulate the helium mixture through the refrigeration cycle, the process that allows concentration of ^{3}He atoms in the high pressure cylinder requires further explanation. This utilization of the induced pressure gradient across the superleak for both pumping and concentration of the ^{3}He in the high pressure cylinder is best explained through the narration of the idealized four step cycle by which the pump operates. The following description of the pumping cycle is summarized by Table 2-1, which describes each process in the cycle, and Table 2-2, which lists the state of the cylinder contents between each process. Additionally, Figure 2-4 illustrates the relative variation of temperature, ^{3}He concentration, and applied field strength in

each cylinder during each of these four processes. Note that the temperature, ^{3}He concentration, and magnetic field strength are all required to define the state of the cylinder contents because both the helium mixture and GGG spheres are included in the system.

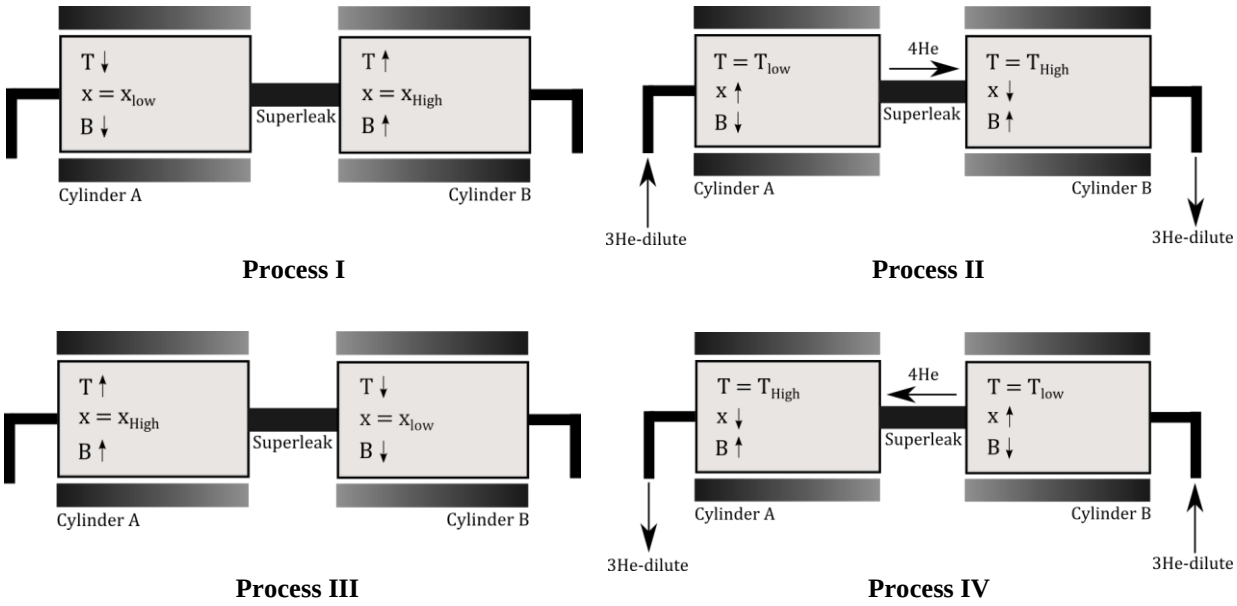

Figure 2-4: The relative thermodynamic states of the helium and GGG within each cylinder for each process in the pumping cycle

Process	Initial State	Final State	Description
I	i	ii	Constant concentration temperature increase/decrease
II	ii	iii	Constant temperature pumping/intake
III	iii	iv	Constant concentration temperature increase/decrease
IV	iv	i	Constant temperature pumping/intake

Table 2-1: Cycle processes for the superfluid magnetic pump

	Cylinder A			Cylinder B		
State	**x**	**T**	**B**	**x**	**T**	**B**
i	x_{low}	T_{high}	B_{max}	x_{high}	T_{low}	B_{min}
ii	x_{low}	T_{low}	$B_{inter,down}$	x_{high}	T_{high}	$B_{inter,up}$
iii	x_{high}	T_{low}	B_{low}	x_{low}	T_{high}	B_{max}
iv	x_{high}	T_{high}	$B_{inter,up}$	x_{low}	T_{low}	$B_{inter,down}$

Table 2-2: Thermodynamic states for the contents of each cylinder between pumping processes

Process I begins with cylinder A at concentration $x_{low,}$ depleted of its ^{3}He charge and at the high temperature, T_{high}. Cylinder B is at concentration x_{high} and the low temperature, T_{low}. Process I raises the temperature of the high concentration charge in cylinder B to T_{high} by increasing the applied field strength in cylinder B from the minimum value to some intermediate value $B_{inter,up}$ while simultaneously decreasing the temperature of the low concentration charge in cylinder A to T_{low} by decreasing the applied field strength in cylinder A to some intermediate value $B_{inter,down}$. The ^{3}He charge in each cylinder remains constant for this process because the helium is prevented from exiting or entering the cylinders through the ports by the check valve network, while the superleak prohibits movement of ^{3}He directly between the cylinders. Further details on the check valve operation are provided in an upcoming section.

Process II is a pumping process during which the temperature in each cylinder is held constant as helium mixture is pumped out through the port of cylinder B, replenished by superfluid ^{4}He flowing from cylinder A through the superleak, and returned to the pump through the port of cylinder A. As this process proceeds, the charge of ^{3}He in cylinder B is depleted since the ^{3}He cannot travel through the small pores of the superleak, thus the fluid replacing the ^{3}He-^{4}He mixture leaving the port is pure superfluid ^{4}He. The opposite effect occurs in cylinder A, where ^{3}He accumulates because ^{3}He-^{4}He mixture enters the cylinder but only ^{4}He leaves through the superleak to cylinder B. To drive such a pumping process, the applied field is increased in cylinder B, where ^{3}He is being depleted, and decreased in cylinder A, where ^{3}He is being accumulated. Unlike process I, which uses the heat transfer from the GGG to raise or lower the internal energy – and thus the temperature – of the helium contained within the cylinders, this

process uses the heat transfer to *maintain* the GGG and helium temperature as a convective flow of ^{3}He-^{4}He mixture transports energy into or out of the cylinder ports.

It is worth to note here that the model developed for the pump in this work is purely thermodynamic – that is, flow rates and pressure drops are calculated from the first and second laws – and thus completely neglects the dependence of the pump operation on the fluid dynamics in the components of the refrigerator away from the pump. To ensure all of the heat transferred from the GGG results in convective flow into or out of the cylinder ports during process II rather than internal energy (and thus temperature) changes of the cylinder contents, the flow resistance between the two pump ports caused by the other refrigerator components must be designed to accommodate the flow rate and pressure drop predicted by the thermodynamic pump model. Since the resistance to flow in the refrigerator is almost entirely determined by the Joule-Thomson valve at the entrance to the mixing chamber, the issue will be addressed further in the section pertaining to that component.

Process II finishes when the applied field in cylinder B reaches the maximum value, B_{max}, and the applied field in cylinder A reaches the minimum value, B_{min}. When this condition occurs, the system is at state iii, which is identical to state i with the cylinders reversed. In other words, at state iii cylinder B has the maximum applied field strength, lowest concentration, and high temperature; at state i, cylinder A has the maximum applied field strength, lowest concentration, and high temperature. To continue circulating helium, processes I and II must be repeated in reverse. Processes III and IV, then, are identical to processes I and II except that the processes occurring in the opposing cylinder. It follows that states iii and iv in cylinder B are identical to

states i and ii, respectively, in cylinder A. A consequence of this pump design and operating scheme is that the directionality of the ^{3}He-^{4}He flow with respect to the pump during process IV is reversed from that of process II, causing a cyclic helium flow rate that must be rectified to operate a dilution refrigeration cycle continuously over the entire series of pump processes.

The reversibility of the magnetic pump relies on the fact that all of the entropy transferred to the helium during the high temperature pumping results from a decrease in the magnetic entropy of the GGG caused by the increase in applied magnetic field. In the theoretical limit with no hysteresis loss, all of the entropy transferred to the helium can be returned to the GGG by reducing the magnetic field to its initial strength (Miller 2009). This advantage becomes more apparent when compared to other possible methods of utilizing the fountain effect to pump the helium mixture. For instance, a resistance heater in cylinder B could be activated during process II to provided heat to the helium mixture; however, cylinder A would have no mechanism to simultaneously cool the returning helium, instead requiring a thermal link from the cylinder to a precooling stage at a lower temperature to remove the entropy from the returning stream while maintaining the temperature difference of the superleak. Using the magnetic pump, this low temperature in cylinder A can be maintained by simply reducing the applied magnetic field on the GGG without the need for an additional external cooling mechanism. While the magnetic pump design also necessarily requires the helium mixture to be thermally linked to a precooling stage to reject heat from pumping and the cooling load, the precooler can be at a relatively high temperature compared to that required if the pumping heat was provided by a resistance heater, since this heat can be removed from the helium at high temperature after it exits the high pressure cylinder rather than in the low temperature, low pressure cylinder.

2.3 Precooling heat exchangers

In order to satisfy the first and second laws, all refrigerators must reject the refrigeration load and pumping heat at a high temperature relative to that at which cooling is provided. For the dilution refrigerator in this thesis, this heat is rejected to a relatively high temperature stage through a set of heat exchangers referred to from now on as the precooling heat exchangers, or simply the precoolers. Figure 2-5 shows the placement of the precoolers and illustrates their function during each of the processes in the pumping cycle that involve helium flows through the pump ports.

The precooling stage is thermally linked to the refrigerator through the helium lines that connect to the ports of both pump cylinders, as shown in Figure 2-5. In process II, the ^{3}He-concentrate forced from cylinder B at temperature T_{high} immediately enters the adjacent precooler, where it is cooled to the temperature of the precooling stage, T_{pc}, by the exit of the heat exchanger. Simultaneously, ^{3}He-dilute returns from the refrigerator at temperature T_{return}, routes through the opposite precooler, and enters cylinder A at the precooler temperature T_{pc}. Since the returning cold ^{3}He-dilute is used to cool the outgoing ^{3}He-concentrate in counterflow recuperators away from the pump not shown in Figure 2-5, T_{return} must be equal to or lower than T_{pc} due to second law considerations in the recuperators. Therefore the cold ^{3}He-dilute is actually *preheated* by the precooler adjacent to cylinder A before being returned to the cylinder during process II. For process IV, the operation of the precoolers is simply inverted since all of the flow direction and temperatures in the pump cylinders are opposite of those for process II.

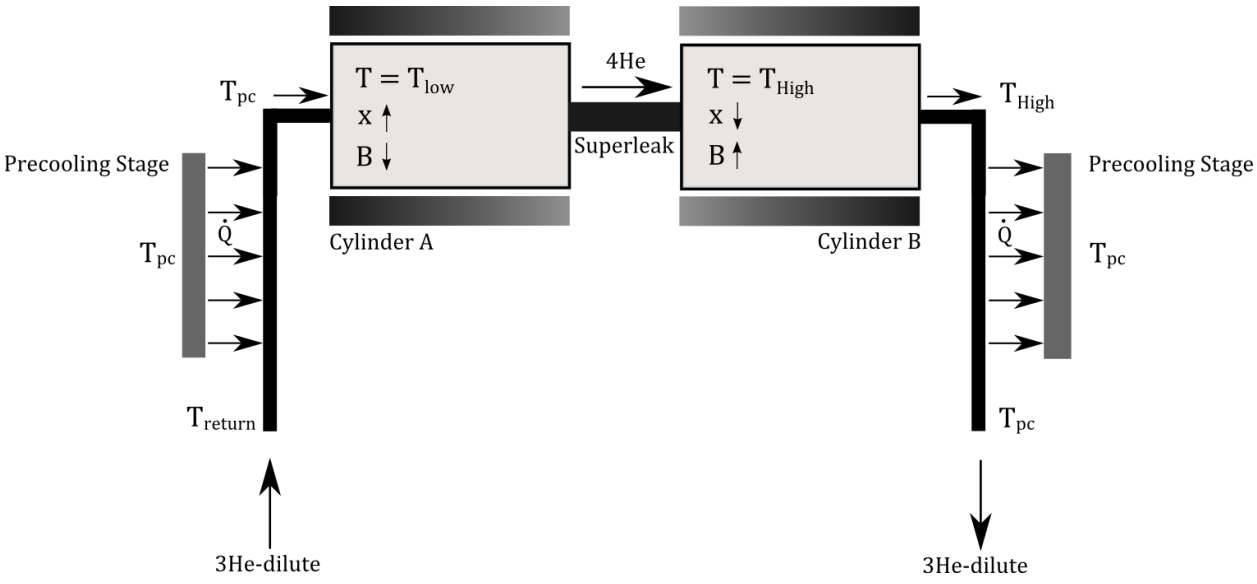

Process II

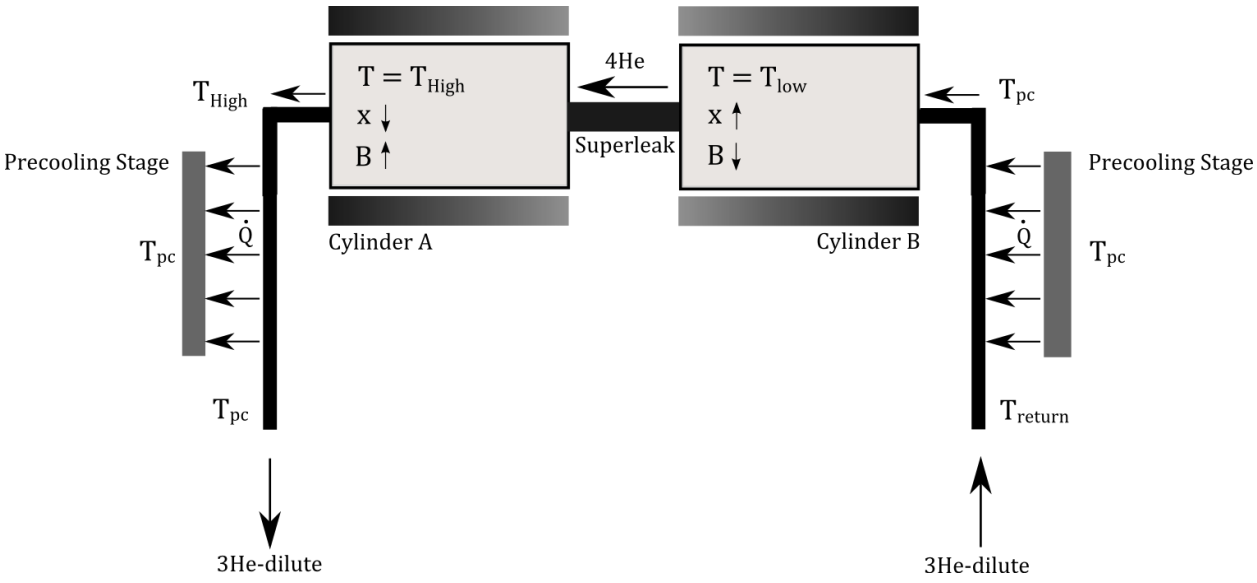

Process IV

Figure 2-5: The function of the precooling heat exchangers during each process of the pumping cycle

While the precooler name may be a bit of a misnomer due to the fact that one of the two precooling heat exchangers is heating the helium stream returning from the mixing chamber during both processes II and IV, the naming convention references the desirable increase in ^{3}He

concentration caused by lowering the temperature, at constant ^{4}He chemical potential, of the superfluid ^{3}He-dilute stream leaving the high pressure cylinder. The superfluid ^{3}He-dilute stream leaving the high pressure cylinder is forced to higher ^{3}He concentrations and closer to the phase separation temperature by 'precooling' prior to entering the first recuperator. Furthermore, there must be a net heat removal from the refrigerant to the precooling stage over the entire cycle, giving additional motive for the name. The precooling heat exchangers will thus be referred to as the 'precoolers' instead of the 'preheaters' because of these important effects.

The model developed in this work does not focus on the details of the precooling heat exchanger design. This is due to the fact that the complexity of these heat exchangers are somewhat trivial compared with other components in the model. Several key assumptions are made with regards to the precoolers, however, that cannot be overlooked. First, the precooling heat exchangers are assumed to be perfectly effective. This implies that the helium mixture leaving the precoolers is brought to the temperature of the precooling stage before leaving the device. Such behavior can be ensured by overdesigning the length of tubing connected to the precooling stage that contains the helium flow. Secondly, the precooler temperature, $T_{pc,}$ is assumed to be constant in time throughout the duration of the cycle. This could be accomplished by building the precooling stage with sufficient thermal mass or by controlling the stage temperature with the cryocooler that removes heat from the precooling stage. As will be become apparent from the simulations analyzed in the discussion section, the performance of the dilution refrigerator is very sensitive to the temperature of the precooling stage, making these assumptions fairly important when analyzing the model.

2.4 Check valves

In order to operate the dilution refrigeration continuously, the oscillating flow of the ^{3}He-dilute flow produced by the magnetic pump must be rectified before being sent to the remaining components in the cycle that require flow in a continuous direction. A set of four check valves located between the precooling and recuperative heat exchangers are employed to accomplish this rectification. Figure 2-1 shows the placement of these valves in the overall refrigerator setup and Figure 2-6 illustrates their function during each of the pumping processes. Referring to Figure 2-6, valves A-1 and B-1 open only when the corresponding cylinder pressure is equal to or *less* than that of the low pressure ^{3}He-dilute stream returning to the pump. Valves A-2 and B-2 open only when the corresponding cylinder pressure is equal to or *greater* than that of the stream of high pressure ^{3}He-dilute leaving the pump on its way to the mixing chamber. Table 2-3 summarizes the actuation of the valves with different system pressure scenarios.

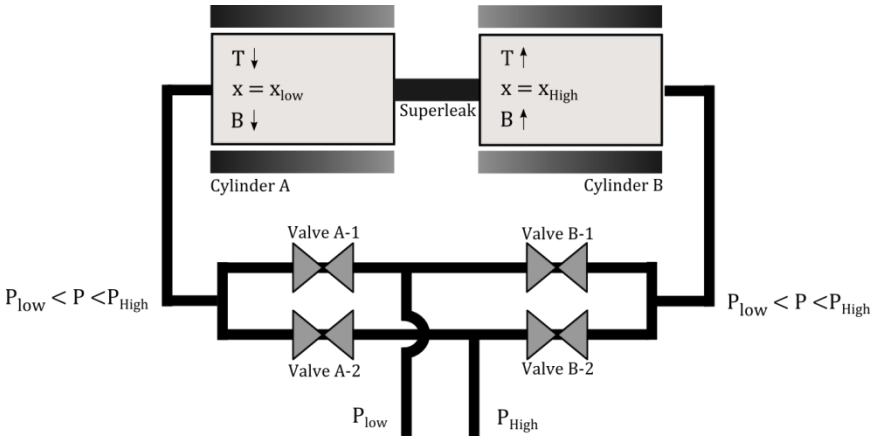

Process I

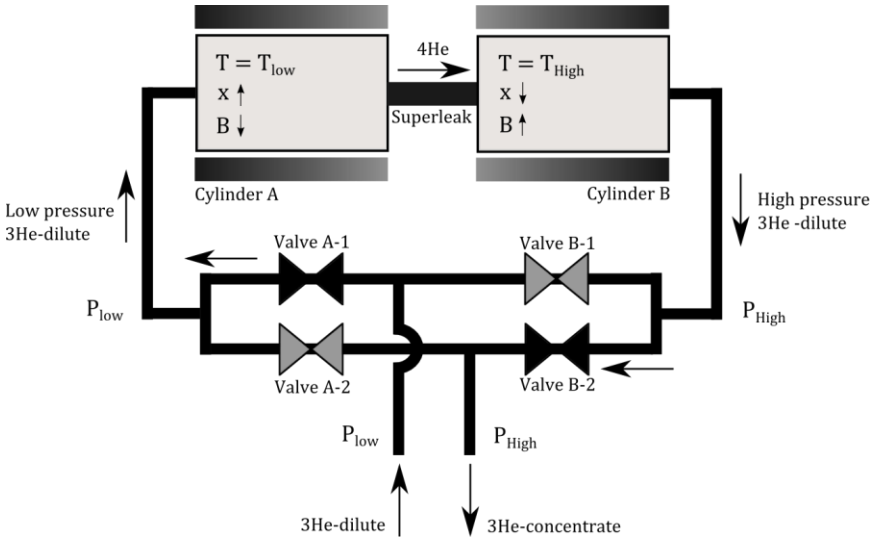

Process II

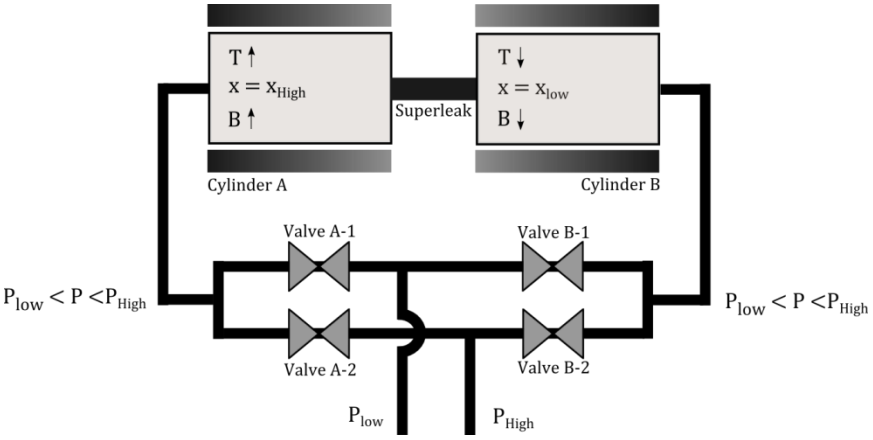

Process III

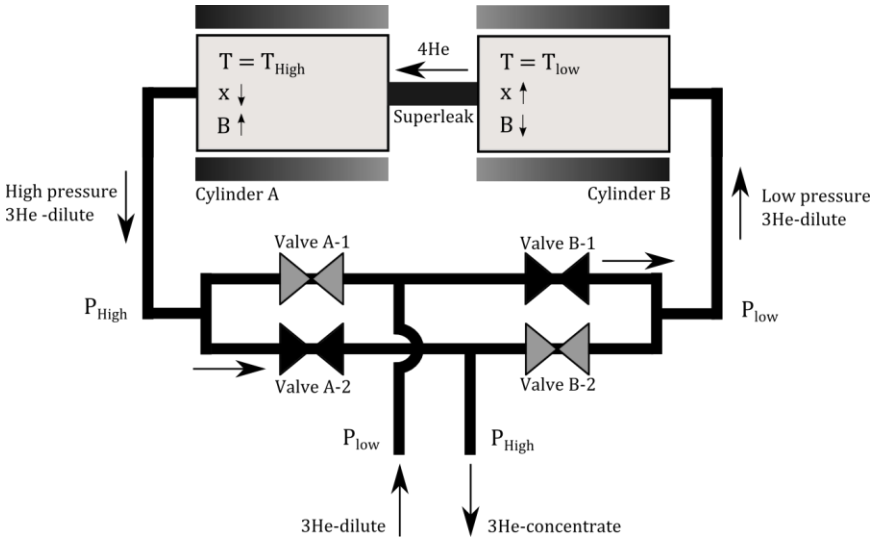

Process IV

Figure 2-6: Schematic illustrating check valve operation during the four pumping processes. Black fill indicates an open valve and grey fill indicates a closed valve

Valve	Criteria for check valve opening
A-1	$P_{\text{Cylinder A}} \leq P_{\text{3He-dilute stream return}}$
A-2	$P_{\text{Cylinder A}} \geq P_{\text{3He-dilute stream out}}$
B-1	$P_{\text{Cylinder B}} \leq P_{\text{3He-dilute stream return}}$
B-2	$P_{\text{Cylinder B}} \geq P_{\text{3He-dilute stream out}}$

Table 2-3: Check valve actuation with pressures in the system

During process I, in which both cylinders experience a change in temperature and pressure at constant concentration, all four of the check valves are closed, trapping the helium charge inside the cylinders. In this process, the pressure rises in cylinder B and is always greater than that of the returning low pressure ^{3}He-dilute stream. Valve B-1 is closed during this process to prevent flow from the high temperature cylinder to the returning low pressure ^{3}He-dilute stream. Although the pressure in cylinder B is higher than the low pressure stream, it is still less than that in the outgoing high pressure stream, however, so valve B-2 is also shut. The behavior of the valves corresponding to cylinder A during this process is the exact opposite of those corresponding to cylinder B, since cylinder A is decreasing in temperature and pressure during

process I. In this case, valve A-1 is closed because the pressure in cylinder A has not dropped below the pressure of the returning low pressure ^{3}He-dilute stream, while valve A-2 is shut to prevent flow of the high pressure ^{3}He-dilute back into the relatively low pressure cylinder A. It follows that all of the check valves are also closed for process III, which is identical to process I except the roles of cylinders are reversed.

Process II is a pumping-intake process at constant cylinder temperatures and pressures, so one valve associated with each cylinder must be open to allow flow out of cylinder B and into cylinder A. In this process, valves B-2 and A-1 are open, allowing high pressure ^{3}He-dilute to flow from cylinder B to the high pressure side of the refrigeration loop while low pressure ^{3}He-dilute simultaneously returns to cylinder A. Valves B-1 and A-2 are shut to prevent high pressure ^{3}He-dilute from cylinder B from bleeding into the low pressure ^{3}He-dilute stream and being directly returned to cylinder A. For process IV, which is identical to process II except that the role of the cylinders is reversed, it follows that valves are again in the opposite states.

For the model developed in this work, the check valves are assumed to actuate perfectly in each of the processes. This means that all four valves maintain perfect seals and completely prevent flow during the constant concentration cylinder temperature changes of processes I and III and that the two closed valves during processes II and IV completely prevent the high pressure ^{3}He-dilute stream from bleeding into the low pressure ^{3}He-dilute stream. Real valves will obviously not perform with such perfection, yet assuming perfect valve seals and actuation greatly reduces the complexity of the model and allows for palatable simulation times while still providing a reasonably accurate description of the pumping process. Since the purpose of the model

developed in this work is for proof-of-concept and initial component sizing, the penalty in accuracy incurred by making this assumption is acceptable compared with the benefit of the simplifications made to the governing equations. Furthermore, assuming perfectly sealed and actuated valves also allows the fluid dynamics associated with the physical design of the valves to be abstracted out of the model. The actual valve design is therefore beyond the scope of this work and will not be discussed here in detail. Details on valve designs suitable for use with superfluid helium mixtures can be found in Miller (2005) and (2010).

2.5 Recuperative heat exchangers and phase separation chamber

After leaving the high temperature cylinder, passing through precooler, and emerging from the check valve network, the rectified flow of high pressure superfluid ^{3}He-dilute must be further cooled to enter the two phase region of the ^{3}He-^{4}He equation of state and fully concentrate to the normal fluid ^{3}He-concentrate phase. Before elaborating on how this cooling – and thus concentrating – is achieved, it is necessary to make two assumptions regarding the operation of the refrigerator. First, the system is assumed to be in a quasi-steady state at all times during the pumping-intake stages of the pumping cycle, processes II and IV. This simply means that helium mass and energy storage in the machine components other than the pump can be neglected for these transient pump processes. Additionally, the high and low pressure sides of the system are joined by superleaks, which allows the ^{4}He superfluid component to flow unimpeded throughout the system. Thermodynamically this means that the ^{4}He chemical potential is maintained at a constant value throughout the machine at all times during the quasi-steady pumping-intake process, with gradients developed during the pumping-intake process canceled instantly by the flow of the ^{4}He superfluid through the superleaks as the pumping-intake proceeds.

This condition of constant ^{4}He chemical potential constrains (and increases) the ^{3}He concentration as the stream is cooled to lower temperatures. Figure 2-7 is a ^{3}He-^{4}He phase diagram that overlays the relative states of the helium mixture between each of the refrigerator components. Note that both the high and low pressure streams follow lines of constant ^{4}He chemical potential (as projected onto the zero pressure T-x diagram) as their temperatures vary throughout the system. Observing the cycle on the phase diagram, it is apparent that the precooling stage alone cannot fully concentrate the high pressure superfluid ^{3}He-dilute mixture to the normal fluid ^{3}He-concentrate phase. To accomplish this, a series of recuperative heat exchangers are employed that use the relatively cold low pressure ^{3}He-dilute stream returning from the mixing chamber to cool and concentrate the high pressure stream.

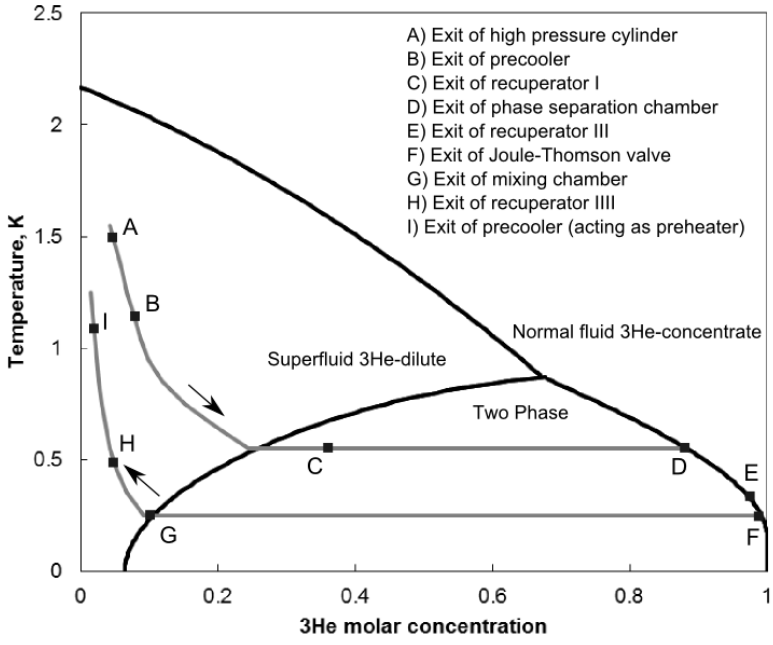

Figure 2-7: Phase diagram showing the relative states of the helium mixture between each of the components in the refrigerator

Three recuperators and a phase separation chamber are required to fully concentrate and cool the high pressure stream before it expands in the Joule-Thomson valve and enters the mixing

chamber. A schematic of these units is shown in Figure 2-8. The first unit encountered by the high pressure ^{3}He-dilute stream upon leaving the check valve network from the high temperature cylinder, labeled recuperator I in Figure 2-8, is a concentric tube counterflow heat exchanger with the high pressure ^{3}He-dilute at high temperature from the pump flowing in the inner tube and the low pressure ^{3}He-dilute returning from the mixing chamber flowing in the annulus. The purpose of this recuperator is to cool the high pressure concentrated ^{3}He-dilute stream to the saturation temperature corresponding to its projected ^{4}He chemical potential before it enters the phase separation chamber. Depending on the operating conditions and cooling load, the high pressure stream may be cooled to its saturation temperature before exiting the recuperator, resulting in two phase flow within the inner tube. This two phase flow regime, unlike more typical two phase flows that are characterized by large density differences between liquid and vapor phases, has a relatively small density difference between the two phases but may, under certain conditions, have significant discrepancies in thermal conductivities since one component is a superfluid and the other is normal fluid. Due to this situation, estimation of the heat transfer coefficients will require careful attention in this recuperator. This issue will be addressed further in the upcoming chapter on model development and theory.

After exiting recuperator I, the high pressure two phase mixture enters immediately into the phase separation chamber. The chamber enables the normal fluid ^{3}He-concentrate phase to physically separate from the superfluid ^{3}He-dilute phase, allowing the former to be preferentially circulated to the mixing chamber. For operation in a gravitational field, the density difference between the phases can be leveraged to perform this separation since the normal fluid ^{3}He-concentrate is less dense than the superfluid ^{3}He-dilute phase. If the schematic of Figure 2-8 is

positioned with the gravitational force directed towards the bottom of the page, the normal fluid ^{3}He-concentrate phase would separate and rise to the top of the chamber, allowing a port near the top of the chamber to preferential remove it from the chamber. In a microgravity environment, differences in surface tension forces between the two phases can be utilized to separate the phases (Roach 2009). In either case, the overall ^{3}He molar concentration and temperature of the phase separation chamber change in time because the saturation condition changes as the pressures (and thus projected ^{4}He chemical potentials) for both streams change as the pumping-intake cycle progresses. This issue is unimportant for the purposes of the simple model developed in this work because the recuperators and phase separation chamber are analyzed at steady state using time averaged pressures and flow rate. In such analysis, which is detailed in subsequent sections, the amount of ^{3}He stored within the phase separation chamber is also averaged in time.

Recuperator II in Figure 2-8 is necessary because both the gravitational and surface tension phase separation methods require heat removal if operating at quasi-steady state. Physically, the low pressure ^{3}He-dilute returning from the mixing chamber runs through a tube wrapped around and brazed to the phase separation chamber. The schematic does not accurately represent this practical geometry, but it does indicate the required thermal contact between the phase separation chamber and the low pressure ^{3}He-dilute stream. The necessity for this recuperator, arising from the difference in effective enthalpies between the incoming two phase flow and outgoing normal fluid ^{3}He-concentrate, will be discussed in further detail as the governing equations are derived in the next chapter.

Following removal from the phase separation chamber, the normal fluid ^{3}He-concentrate phase enters recuperator III, also shown in Figure 2-8, for further cooling before entering the Joule-Thomson valve and expanding into the mixing chamber. Cooling the normal fluid ^{3}He-concentrate as close as possible to the temperature of the ^{3}He-dilute phase returning from the mixing chamber is advantageous as it decreases the lowest possible temperature achievable in the mixing chamber (Enss 2005). Due to this behavior, this recuperator is intentionally oversized to ensure the lowest possible temperature difference between the low pressure ^{3}He-dilute returning from the mixing chamber and the normal fluid ^{3}He-concentrate traveling to the Joule-Thomson valve.

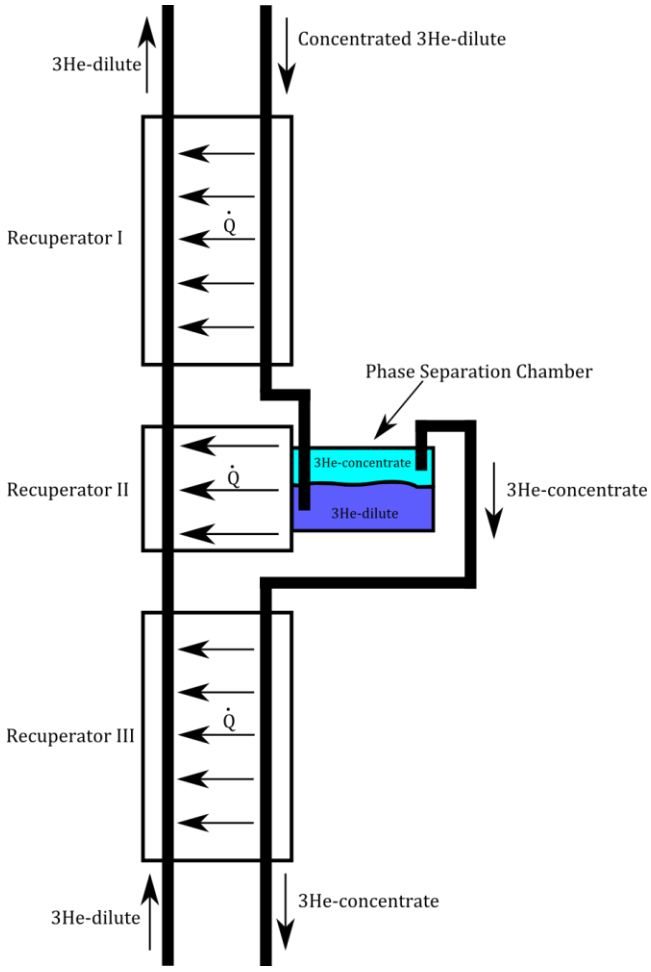

Figure 2-8: Detailed schematic of the recuperative heat exchangers and phase separation chamber

It is important here to also briefly touch on the thermodynamics of the helium mixture and the related issues with solving the governing heat exchanger equations for the recuperators. Of highest importance for the analysis of the recuperators are the transient projected ^{4}He chemical potentials and ^{3}He molar flow rates produced by the pump. These quantities are periodic in time due to the nature of the pump design and present challenges in modeling the recuperative heat exchangers. To avoid solving the recuperator governing equations at unsteady conditions, the model developed in this work solves for the temperature distribution in the heat exchangers at a steady state condition using root mean square (RMS) values in time for both the ^{3}He molar flow rate and each stream's projected ^{4}He chemical potential. This simplification allows both the temperature distribution in the recuperators and the refrigerator cooling power to be estimated with RMS values, which means the time dependent solution is never computed and thus some information about the behavior of the system is unavailable when using this technique. Without such a simplification however, the complexity of the governing equations quickly escalates, greatly increasing the amount of setup and computational time needed to solve the problem. Since the RMS estimates are sufficient to characterize performance for a proof-of-concept design, such a simplification is acceptable for this work. This topic will be discussed in further detail in the model development section.

Another important issue with the recuperator analysis is the strong ^{3}He molar concentration dependence of the helium mixture thermal conductivity. This relationship is curve fit from experimental data at several ^{3}He concentrations given by Lounasmaa (1974) and shown in Figure 2-9. A clear power low dependence on ^{3}He molar concentration can be seen in the figure, asymptoting to an effectively infinite value for pure ^{4}He. The curve is valid for all temperatures

less than 1K since the thermal conductivity does not change significantly with temperature in this temperature range. Since the ^{3}He concentration of both the hot and cold streams may experience large changes in concentration throughout the length of the recuperators, it is clear that the thermal conductivity, and thus the local heat transfer coefficient, will vary noticeably with axial position in each of the recuperators. Furthermore, the specific heat of the mixture at constant ^{4}He chemical potential is also a strong function of concentration. These issues make the analysis of heat exchangers using ^{3}He-^{4}He mixtures as the working fluid more complex compared to a more typical situation where a pure fluid is used as the working fluid. Owing to this added complexity, direct numerical integration of the governing differential equations for the heat exchangers is employed to find the temperature distribution in the recuperators instead of a numerical approach based on the effectiveness – thermal transfer units method.

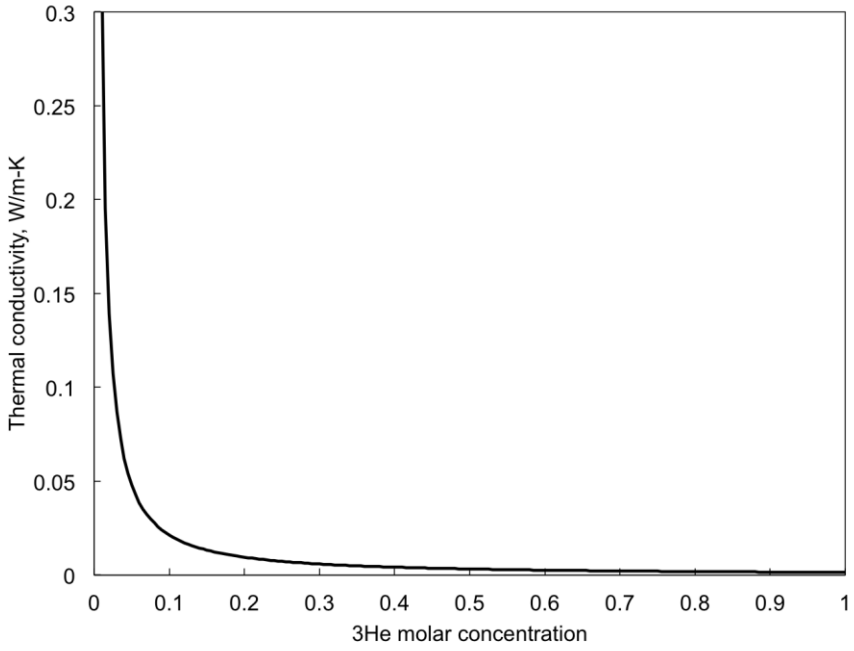

Figure 2-9: Thermal conductivity of ^{3}He-^{4}He mixtures as a function of ^{3}He concentration, fitted to experimental data from Lounasmaa (1974)

2.6 Mixing chamber and Joule-Thomson valve

After leaving recuperator III cooled to nearly the temperature of the mixing chamber, the high pressure normal fluid ^{3}He-concentrate is expanded through a Joule-Thomson valve, in parallel with a superleak which maintains constant ^{4}He chemical potential on both sides of the valve, prior to entering the mixing chamber. Once in the mixing chamber, the ^{3}He atoms flow from the normal fluid ^{3}He-concentrate phase to the superfluid ^{3}He-dilute phase, requiring a thermal energy input to do so. Figure 2-10 is a schematic of valve, superleak, and mixing chamber magnified from Figure 2-1.

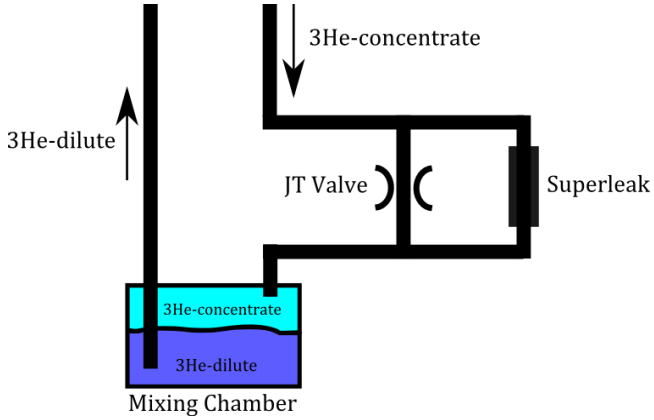

Figure 2-9: Schematic of the Joule-Thomson valve, superleak, and mixing chamber

The model developed in this work makes several assumptions about these components in an effort to simplify the analysis. The first involves the sizing of the flow resistance provided by the Joule-Thomson valve. As discussed previously, the flow rates predicted by the pump model depend purely on the thermodynamics of the system, ignoring the fluid dynamics entirely. Since the Joule-Thomson valve is the largest flow resistance in the system by far due to the relatively high viscosity of the low temperature normal fluid ^{3}He-concentrate phase flowing through it, the valve sizing must be matched with the pressure differential developed in the pump to allow the

same ^{3}He molar flow rates as predicted previously by the pump energy balances. If this matching is not done correctly, the model breaks down because the ^{3}He molar flow rates predicted by the pump model will not be correct. In such a situation, the Joule-Thomson valve would provide flow resistance that the pump model, as developed here, does not account for. For the model developed in this work, the flow resistance of the Joule-Thomson valve is assumed to always restrict the helium flow rate to that predicted by the thermodynamic pump model.

The second important assumption made with regards to this set of components is that of perfect effectiveness for the mixing chamber heat exchanger. Operating at design conditions, the minimum mixing chamber temperature will be less than 100 mK, which heavily impacts the rate of heat exchange between the superfluid helium and the mixing chamber casing. At such low temperatures, the mismatch in phonon velocities between the superfluid helium and solid casing, which is typically a metal such as copper, causes a significant thermal resistance, known as the Kapitza resistance (Enss 2005). Consequently, large heat exchange areas are needed to sufficiently exchange heat between the helium mixture and chamber casing. For this thesis, the mixing chamber is assumed to have a large enough heat transfer area such that the cooling load and the mixing helium are always at the same temperature.

2.7 Startup operation

The steady state model developed in this thesis assumes the refrigerator operates as a dilution refrigerator at the design conditions. During initial cool down, however, the refrigerator must operate first as superfluid Joule-Thomson refrigerator to drop the refrigerator components to a temperature low enough for phase separation to occur. Prior to startup, the entire dilution

refrigerator assembly is cooled by a vapor compression ^{4}He cycle to the temperature of the precooling stage, which is typically around 1.1 K. It is clear from the ^{3}He-^{4}He phase diagram in Figure 2-7 that the dilution refrigeration cooling mechanism of transferring ^{3}He atoms from the normal fluid ^{3}He-concentrate phase to the superfluid ^{3}He-dilute phase – which requires traversing the two phase region in the figure – cannot occur above 0.8 K because the two phase region does not exist above this temperature. The refrigerator must operate solely as a Joule-Thomson cycle with superfluid ^{3}He-dilute phase in *all* recuperator passages until the mixing chamber reaches this temperature. When the critical temperature is attained in the mixing chamber, the normal fluid ^{3}He-concentrate phase can be harvested and the dilution cycle can take over. The transient startup as a superfluid Joule-Thomson refrigerator is not addressed in this work since relevant modeling of the superfluid Joule-Thomson cycle has already been completed by Miller (2005).

2.8 References

Enss, C. and Hunklinger, S., Low temperature physics, Springer, New York, 2005.

Lounasmaa, O., Experimental principles and methods below 1 K, Academic Press, 1974.

Miller, F., "A cold cycle dilution refrigerator for space applications", NASA SBIR phase I proposal, 2010.

Miller, F. and Brisson, J., "A superfluid pulse tube driven by a thermodynamically reversible magnetic pump", International Cryocooler Conference proceedings, 2009.

Miller, F., The development of a proof of principle superfluid Joule-Thomson refrigerator for cooling below 1 Kelvin, Ph.D. Dissertation, Massachusetts Institute of Technology, 2005.

Roach, P., "Progress on a microgravity dilution refrigerator", Cryogenics, 39, 1015-1019, 1999.

3 Model development, theory, and solution procedure

With the design and operational details of the cold cycle ^{3}He-^{4}He dilution refrigerator fully explained, a thermodynamic model that describes the cycle and its associated governing equations can be now be derived. As noted previously, the model developed in this thesis is based solely on the application of the first and second laws to the relevant components and processes in the refrigerator. Applying the laws of thermodynamics allows the key measures of refrigerator performance to be related to the controllable design and operating parameters, thus allowing the performance of the machine to be predicted and studied for a wide range of component designs and control schemes. Table 3-1 is an abbreviated list of important design parameters and performance indicators of interest for the refrigerator setup used in this thesis.

Design and operating parameters		**Performance indicators**	
T_{pc}	Precooling stage temperature	$\dot{Q}_{mc}$	Mixing chamber cooling capacity
γ	GGG porosity (void volume)	T_{mc}	Mixing chamber temperature
B_{max}	Maximum applied field strength	$\dot{Q}_{reject}$	Precooler reject heat
t_{pump}	Pumping period (time required for process II or IV)	$\dot{n}_{3He}$	^{3}He molar flow rate
V_{cyl}	Cylinder volume		
L_{R-I}	Length of recuperator I		

Table 3-1: A non-comprehensive list of important design parameters and performance indicators for the cold cycle ^{3}He-^{4}He dilution refrigerator design used in this work

For example, one may be interested in determining the lowest mixing chamber temperature achievable for a number of different pump cylinder volumes, or finding the variation of cooling capacity with changes in the precooling stage temperature. Understanding the relationship between such design parameters and measures of refrigerator performance through the use of the

model developed in this chapter will be critical for the initial design of a proof-of-concept machine.

3.1 Submodel approach to building the overall system model

To reduce the complexity of the equation set and shorten simulation times, the model of the overall cycle is constructed using two submodels consisting of decoupled equations sets – one representing the components that experience cyclic helium flows – the pump cylinders, precoolers, and check valves – and the another that represents the remainder of the components subjected only to the rectified, unidirectional flows. By splitting the model as such, the governing equations for the pump processes can be solved independently from those governing the recuperator network for a given set of operating conditions. Decoupling the submodels is made possible by the fact that the system is being modeled at a periodic steady state, which *by definition* requires that all the ^{3}He leaving the high pressure cylinder during a pumping process returns to the low pressure cylinder by the end of that same pumping process. The recuperator submodel can then be solved using the results from pump submodel solution. Figure 3-1 highlights the components composing each submodel in the overall refrigerator schematic.

Each of the components within the pump submodel experience unrectified, time-dependent helium flow. The pump submodel describes a single sequence of pumping processes I-IV when the system is operating in a periodic steady state. The analysis of a single sequence of these processes is adequate to describe continuous periodic operation because all additional cycles will be identical in the periodic steady state. For a given set of design and operating parameters, the pump model predicts the ^{3}He molar flow rate and projected ^{4}He chemical potentials as functions

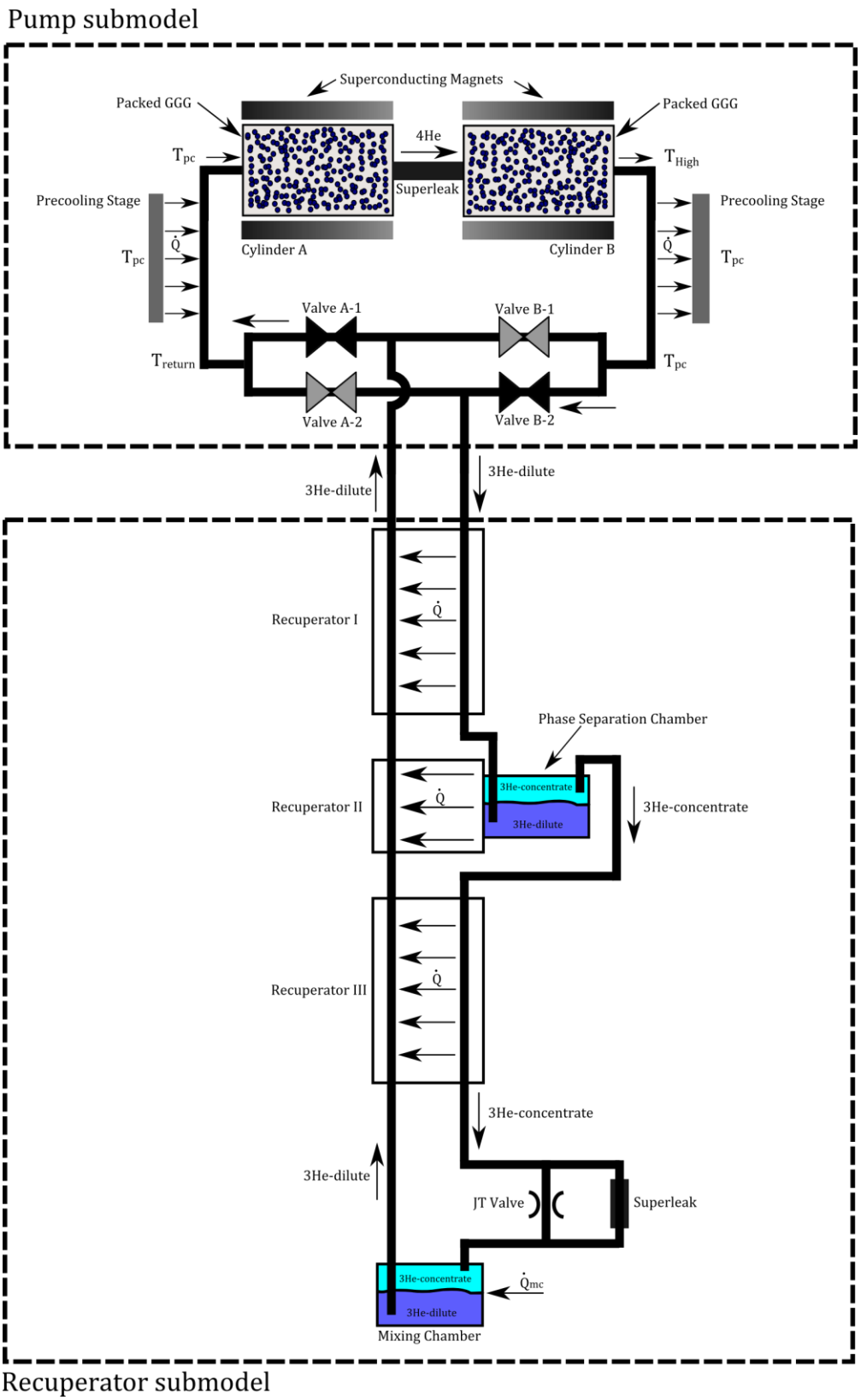

Figure 3-1: Schematic of the refrigerator depicting the components grouped into the two submodels

of the applied magnetic field, all of which change in time. Consequently, the pump submodel computes a time accurate solution for all calculated parameters.

The components within the recuperator submodel, unlike those contained in the pump submodel, experience only rectified, unidirectional helium flows. Even though these flows are rectified, the magnitude of the ^{3}He molar flow rate and projected ^{4}He chemical potentials change in time as the pump completes the discharge-intake processes II and IV. As discussed previously, due to constraints on simulation time and to reduce the model complexity, a time dependent solution to the heat exchanger temperature profiles is not provided by the recuperator submodel. Instead, the time-accurate ^{3}He molar flow rates and projected ^{4}He chemical potentials computed by the pump submodel are used to calculate RMS values with respect to time for their respective quantities. The recuperator submodel is then solved at steady state using the RMS ^{3}He molar flow rate and projected ^{4}He chemical potentials. As a result of this simplification, the recuperator submodel does not predict a time accurate solution as does the pump submodel, but rather an estimate of the solution at the RMS pump conditions.

Finally, the equations developed for the submodels in the upcoming sections contain many references to the equations of state for ^{3}He-^{4}He mixtures and Gadolinium Gallium Garnet. All thermodynamic properties for the helium mixture, except for the internal energy, are tabulated from the equation of state developed by Chaudhry (2009). The internal energy for the helium mixture is calculated from the simple equation of state developed by Miller (2001). The two are compatible because the reference states for both equations of state are the same. GGG properties are determined by state equation for paramagnetic salts as reported by Lounasmaa (1974).

3.2 Development of the pump submodel

To derive the governing equations for the time accurate pump submodel, the first and second laws are applied to targeted control volumes in a single pump cylinder during each of four pumping processes. This leads to a set of equations, which depend on the design and targeted operating parameters, which must be solved simultaneously to obtain the time dependent ^{3}He molar flow rate and projected ^{4}He chemical potentials. Cylinder B (chosen arbitrarily from the two – cylinder A just has easily been picked) will be used to define the control volumes and derive the equations for each of the processes. This approach provides sufficient information to solve for the entire two cylinder pumping cycle due to the symmetry of the problem. Figure 2-4, Table 2-1, and Table 2-2 describe the four pumping processes and serve as a useful references for the following derivations; however, the schematics of Figure 2-4 will be reproduced here in tandem with their corresponding control volumes for completeness.

3.2.1 Process I

Figure 3-2 shows a schematic of the entire pump assembly with the relative changes in the states of both the helium mixture and GGG occurring during process I. Also shown is a control volume containing the helium mixture and GGG in cylinder B during the same process.

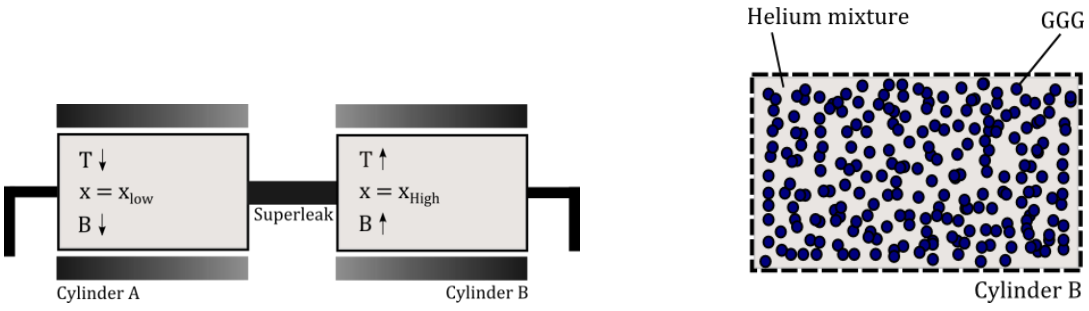

Figure 3-2: (a) Schematic showing the relative states of the helium mixture and GGG in both cylinders during process I and (b) control volume containing the helium mixture and GGG in cylinder B. GGG not shown in (a) for clarity

Equation 3.1 is the general form of the second law for a control volume with one inlet and one exit using a superfluid mixture as the working fluid, as shown by Miller (2001). Although similar to the second law for a control volume with a normal fluid as the working fluid, the convective entropy flow for the superfluid is only associated with *normal* fluid ^{3}He component of the mixture, so the total molar flow rate is replaced by the ^{3}He molar flow rate, $\dot{n}_{3He}$, for the superfluid case. Note that the specific entropy of the mixture, s_{He}, in the convective terms must be expressed on ^{3}He molar basis for this form to be valid.

$$\dot{n}_{3He,in}s_{He,in} - \dot{n}_{3He,out}s_{He,out} + \frac{\dot{Q}}{T_{boundry}} + \dot{S}_{gen} = \frac{dS_{CV}}{dt} \tag{3.1}$$

The following information and assumptions for process I have been discussed previously and are applied here to produce an expression of the second law describing the control volume of Figure 3-2b during that process:

1. No helium enters or leaves the control volume during process I because the valves are closed
2. No heat transfer occurs with the surroundings
3. Thermal gradients within the control volume are negligible, so the process is reversible and thus has no entropy generation

With this knowledge, the second law is simplified from its general form and applied to the control volume, resulting in Equation 3.2.

$$\dot{S}_{gen} = 0 = \frac{dS_{CV}}{dt} = \frac{dS_{He}}{dt} + \frac{dS_{GGG}}{dt} \tag{3.2}$$

This equation shows that the temperature increase at constant concentration occurring during process I requires the net change in entropy within the control volume to be zero. For this to be the case, the decrease in entropy of the GGG caused by increasing the magnetic field strength during process I must be accompanied by an equal increase in entropy of the helium mixture. In other words, process I results in a transfer of entropy from the GGG spheres to the helium mixture in the cylinder.

To evaluate Equation 3.2 in terms of the applied field strength B, cylinder temperature T, and ^{3}He molar concentration x, thermodynamic properties for both the GGG and the helium mixture must be known. The Chaudhry ^{3}He-^{4}He equation of state used for this model allows the molar specific entropy of the mixture (J/K-mole-^{3}He) to be obtained from the temperature (K) and ^{3}He molar concentration (dimensionless), as shown in Equation 3.3.

$$s_{He} = s_{He}(x, T) \tag{3.3}$$

Likewise, the Lounasmaa paramagnetic salt equation of state allows the molar specific GGG entropy to be expressed in terms of the temperature and applied magnetic field, as given in Equations 3.4.1 and 3.4.2. Combining these equations gives the specific molar entropy of the

GGG (J/mol-K) in terms of the temperature (K), the applied magnetic field (Tesla), and a number of both universal and salt-specific constants.

$$s_{GGG} = s_{GGG}(B,T) = R\left[\frac{x_c}{2J}\coth\left(\frac{x_c}{2J}\right) - \frac{(2J+1)x_c}{2J}\coth\left(\frac{(2J+1)x_c}{2J}\right) + \ln\left[\frac{\sinh\left(\frac{(2J+1)x_c}{2J}\right)}{\sinh\left(\frac{x_c}{2J}\right)}\right]\right] \quad (3.4.1)$$

$$x_c = \frac{\beta J g}{kT}\sqrt{b^2 + B^2} \quad (3.4.2)$$

The universal constants in these equations include the universal gas constant R (8.314 J/K-mol), the Bohr magneton constant β (9.274 x 10^{-24} J/Tesla), and Boltzmann's constant k (1.381 x 10^{-23} J/K). Salt-specific constants for GGG are the intrinsic internal magnetic field b (0.481 Tesla), J (7/2), and g (2).

With the equations of state for the helium mixture and GGG available to relate the specific entropies to the temperature, applied magnetic field, and ^{3}He molar concentration, the second law statement of Equation 3.2 can be rewritten in terms of these latter properties. Considering also that the applied field strength and cylinder temperature are functions of time during process I, Equation 3.2 can be written as

$$0 = \frac{d\left(n_{3He,i}s_{He}\left(x_i, T(t)\right)\right)}{dt} + \frac{d\left(n_{GGG}s_{GGG}\left(B(t), T(t)\right)\right)}{dt} \quad (3.5)$$

where $n_{3He,i}$ is the molar charge of ^{3}He in the cylinder that is constant throughout process I and n_{GGG} is the number of moles of GGG contained within the cylinder (which remains constant over *all* of the pump processes). Knowing that the amount of ^{3}He and GGG within the control volume

is constant in time, these values can be pulled out of the integrand for the time integration over process I from state i to state ii, shown in Equation 3.6.

$$0 = n_{3He,i} \int_{i}^{ii} \frac{d\left(s_{He}\left(x_i, T(t)\right)\right)}{dt} + n_{GGG} \int_{i}^{ii} \frac{d\left(s_{GGG}\left(B(t), T(t)\right)\right)}{dt} \tag{3.6}$$

Before integrating, expressions for the molar charges of ^{3}He and GGG can be obtained in terms of the pump design parameters and properties of the system. The ^{3}He molar charge during process I can be determined from the volume of the cylinder occupied by the helium mixture and the specific ^{3}He molar volume of the mixture,

$$n_{3He} = \frac{\gamma V_{cyl}}{v_{3He}} \tag{3.7}$$

where the total cylinder volume V_{cyl} (m^3) is multiplied by the dimensionless GGG porosity γ, which is simply the fraction of the total cylinder volume *not* occupied by the GGG, to give the volume of the cylinder occupied by the helium mixture. The specific molar ^{3}He volume (m^3/mol-^{3}He) is a function of ^{3}He molar concentration in Equation 3.8, as shown in Equation 3.8 given by Radebaugh (1967).

$$v_{3He} = \left(\frac{27.58}{x} + 7.60x + 1.65x^2\right) 10^{-6} \tag{3.8}$$

With these relations, the ^{3}He molar charge in the cylinder can now be expressed in terms of the total cylinder volume V_{cyl}, GGG porosity γ, and ^{3}He molar concentration x.

$$n_{3He} = n_{3He}(x, V_{cyl}, \gamma) \tag{3.9}$$

Similarly, the number of GGG moles contained in the cylinder can be computed with Equation 3.10.

$$n_{GGG} = \frac{(1-\gamma)V_{cyl}\rho_{GGG}}{MM_{GGG}} \tag{3.10}$$

Here the total cylinder volume occupied by the GGG is multiplied by the molar density to obtain the number GGG moles contained in the system. Since the GGG is solid and incompressible, its molar density is constant over all the pumping processes. The molar density can be found by dividing the GGG mass density ρ, which is 7080 kg/m^3 (Perry 1995), by the GGG molar mass MM_{GGG}, which is 1.01235 kg/mol. With these constants and Equation 3.10, the molar amount of GGG contained in the cylinder is a function of only the cylinder volume and GGG porosity – both design parameters.

$$n_{GGG} = n_{GGG}(V_{cyl}, \gamma) \tag{3.11}$$

Knowing that the ^{3}He molar charge is a function of the ^{3}He molar concentration, cylinder volume, and GGG porosity, substituting Equations 3.11 and 3.9 into Equation 3.6 and carrying out the integration results in Equation 3.12.

$$\begin{aligned} 0 = {} & n_{3He,i}(x_i, V_{cyl}, \gamma)[s_{He}(x_i, T_{ii}) - s_{He}(x_i, T_i)] \\ & + n_{GGG}(V_{cyl}, \gamma)[s_{GGG}(B_{ii}, T_{ii}) - s_{GGG}(B_i, T_i)] \end{aligned} \tag{3.12}$$

Equation 3.12 is the final form of the second law for process I in cylinder B. With the GGG porosity and cylinder volume fixed by the design of the pump, the equation defines a relation between states i and ii specified by the temperatures, applied field strengths, and constant ^{3}He molar concentration. Note that the series of assumptions applied to the control volume allowed the time to be integrated out of the problem for this process, transforming the second law from an ordinary differential equation to an algebraic equation.

3.2.2 Process III

Although straying from the chronological order of the pumping cycle, the governing in equation for process III is derived next because process III is essentially the inverse of process I. Due to this, this derivation will closely parallel that for process I. Figure 3-3 shows a schematic of the entire pump assembly with the relative changes in the states of the helium mixture and GGG occurring during process III. Also shown is a control volume containing the helium mixture and GGG in cylinder B during the same process.

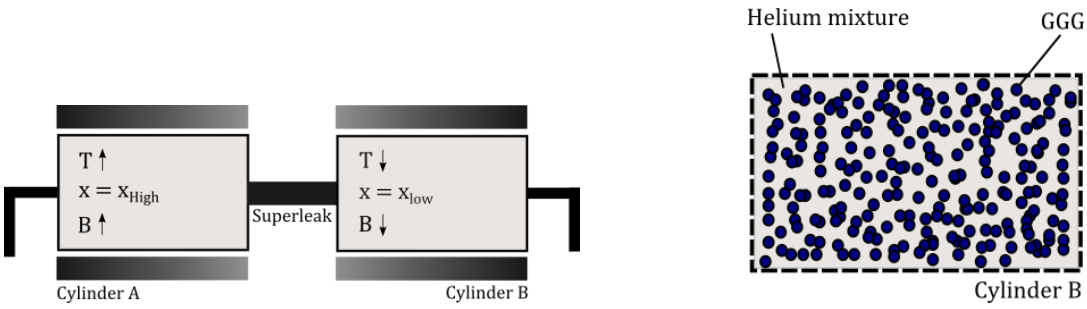

Figure 3-3: (a) Schematic showing the relative states of the helium mixture and GGG in both cylinders during process III and (b) control volume containing the helium mixture and GGG in cylinder B. GGG not shown in (a) for clarity

The control volume used for process III is identical to that used for process I – both the helium mixture and GGG spheres in cylinder B are included. The only differences between the processes are the initial and final states of the system and the reverse direction of the change in applied magnetic field. Due to the similarities to process I, the second law for process III is also described by Equation 3.2, repeated here for completeness.

$$\dot{S}_{gen} = 0 = \frac{dS_{CV}}{dt} = \frac{dS_{He}}{dt} + \frac{dS_{GGG}}{dt} \tag{3.13}$$

With the equations of state for the helium mixture and GGG available as discussed previously, Equation 3.13 can be rewritten as follows.

$$0 = \frac{d\left(n_{3He,iii} s_{He}\left(x_{iii}, T(t)\right)\right)}{dt} + \frac{d\left(n_{GGG} s_{GGG}\left(B(t), T(t)\right)\right)}{dt} \tag{3.14}$$

This statement is nearly identical to that of Equation 3.5 which describes process I except the ^{3}He molar charge is based on the amount of ^{3}He in the cylinder at the state iii rather than state i. With the molar charge of ^{3}He and GGG constant through the process, Equation 3.14 can be integrated in time from state iii to state iv as Equation 3.15.

$$0 = n_{3He,iii} \int_{iii}^{iv} \frac{d\left(s_{He}\left(x_{iii}, T(t)\right)\right)}{dt} + n_{GGG} \int_{iii}^{iv} \frac{d\left(s_{GGG}\left(B(t), T(t)\right)\right)}{dt} \tag{3.15}$$

Using the same substitutions for the ^{3}He and GGG molar charges that were developed previously for process I, the integration of Equation 3.15 results in Equation 3.16.

$$0 = n_{3He,iii}(x_{iii}, V_{cyl}, \gamma)[s_{He}(x_{iii}, T_{iv}) - s_{He}(x_{iii}, T_{iii})] + n_{GGG}(V_{cyl}, \gamma)[s_{GGG}(B_{iv}, T_{iv}) - s_{GGG}(B_{iii}, T_{iii})] \quad (3.16)$$

Equation 3.16 is the final form of the second law for process III in cylinder B. Similar to Equation 3.12 for process I, the equation defines a relation between states iii and iv specified by the temperatures, applied field strengths, and constant ^{3}He molar concentration, as the GGG porosity and cylinder volume are fixed by the design of the pump.

3.2.3 Process II

With processes I and III adequately described, the governing equations for the constant temperature pumping-intake processes can be developed. The pumping process will be analyzed first, which for cylinder B occurs in process II. Figure 3-4 shows a schematic of the entire pump assembly with the relative changes in the states of the helium mixture and GGG occurring during this process in addition to the direction of the helium flows. Figure 3-5 shows two control volumes important for this derivation – one containing only the *GGG spheres* within cylinder B and the other containing only the *helium mixture* within cylinder B.

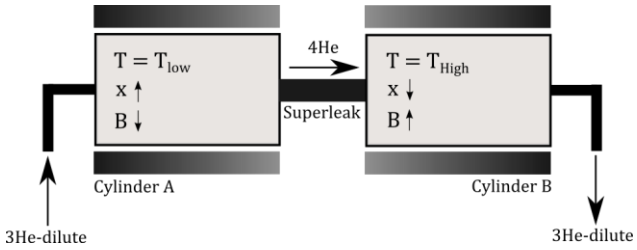

Figure 3-4: Schematic showing the relative states of the helium mixture and GGG in both cylinders during process II. Also shown are the helium flow directions. GGG not shown for clarity

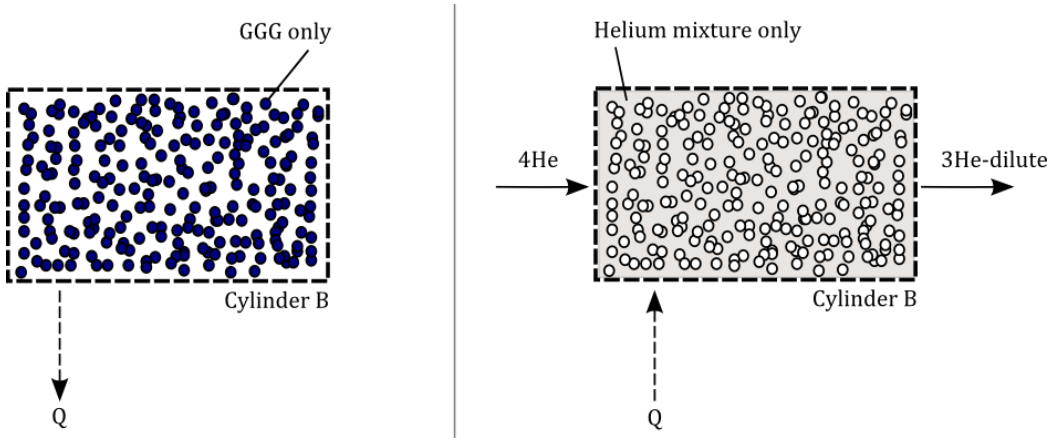

Figure 3-5: (a) Control volume containing only the GGG spheres contained in cylinder B and (b) control volume containing only the helium mixture in cylinder B, both for process II.

Unlike processes I and III, process II has convective flows of helium entering and leaving the cylinder. Since the pure superfluid ^{4}He that replenishes the ^{3}He-^{4}He mixture leaving through the exit port essentially results in a dilution of the mixture remaining in the cylinder, entropy must be generated during this event. Consequently, a single control volume cannot be used in conjunction with the second law to fully describe this process because the entropy generation cannot be set to zero. Instead, the governing equation for process II is derived by splitting the helium mixture and GGG contained within cylinder B into two separate control volumes. Doing this allows the irreversiblities to be isolated within the helium mixture control volume – which can be analyzed by applying the first law since there is no need to actually find the value of the entropy

generation – while the reversible process occurring in the GGG control volume can be described through the second law by taking advantage of the fact that the energy generation is zero. The analyses are then coupled using the heat transfer between the GGG and the helium mixture.

The following information and assumptions associated with process II, discussed previously in the design and operation chapter, can now applied to the energy balance on the helium control volume:

1. At any instant in time, the helium mixture is at the same ^{3}He molar concentration, temperature, and ^{4}He chemical potential at all spatial locations within the control volume. Additionally, the ^{4}He chemical potential is identical at the inlet and exit ports due to the quasi-steady state.
2. No heat transfer occurs between the pump cylinder walls and the helium mixture
3. The control volume surface in contact with the GGG spheres is at the temperature of the mixture
4. The temperature of the control volume is constant in time
5. The change in ^{3}He molar concentration through the entirety of process II is small enough that the specific molar volume of the mixture remains approximately constant.

To begin the derivation, the general control volume form of the first law is stated in Equation 3.17.

$$\dot{n}_{He,in}h_{He,eff,in} - \dot{n}_{He,out}h_{He,eff,out} + \dot{Q} = \frac{dU_{He}}{dt} \tag{3.17}$$

This form of the first law has limited usefulness in analyzing systems with superfluid mixtures as the working fluid, however, since the total helium molar flow rates $\dot{n}_{He,in}$ and $\dot{n}_{He,out}$ are net flow rates – the combination of a normal fluid and superfluid component that may have different velocities. To more easily analyze the system, the equation is modified to split the convective energy flux into separate terms – one for the normal component and one for the superfluid component. This approach was first used by Ebner (1971) and is now standard for the analysis of systems with superfluid working fluids (Miller 2005 and Chaudhry 2009). Equation 3.18 is the substitution for the effective energy flux at an inlet or exit of a control volume based on Ebner's method:

$$\dot{n}_{He} h_{He,eff} = \dot{n}_{3He} h_{os} + \dot{n}_{4He} \mu_{4He} \tag{3.18}$$

With this substitution, the molar flow rates of the normal fluid ^{3}He and superfluid ^{4}He have been clearly separated. The ^{4}He chemical potential appearing in Equation 3.18 is just the partial molar Gibbs free energy of the ^{4}He in the mixture, defined by the standard relation for binary solutions

$$\mu_{4He} = x g_{He} + x \left(\frac{\partial}{\partial x}\right)_{x,T} x g_{He} \tag{3.19}$$

where x is the ^{3}He molar concentration and g_{He} is the molar specific Gibbs free energy of the mixture. The osmotic enthalpy is a property of the mixture defined by the Ebner control volume analysis as follows

$$h_{os} = h_{He} + \left(\frac{1-x}{x}\right)\mu_{4He} \tag{3.20}$$

where h_{He} is the actual enthalpy of the mixture and x is again the ^{3}He molar concentration. Both the ^{4}He chemical potential and osmotic enthalpy are available from the Chaudhry equation of state as functions of the temperature and ^{3}He molar concentration at zero pressure.

Combining the energy balance of Equation 3.17 with relation in Equation 3.18, knowing that the ^{4}He chemical potential is identical at the inlet and exit, results in the following expression.

$$\dot{n}_{3He,in}h_{os,in} + \dot{n}_{4He,in}\mu_{4He} - \dot{n}_{3He,out}h_{os,out} - \dot{n}_{4He,out}\mu_{4He} + \dot{Q} = \frac{dU_{He}}{dt} \tag{3.21}$$

Since the analysis of the system is being completed on a basis of ^{3}He molar flow rates, it is necessary to eliminate the ^{4}He molar flow rate from the energy balance equation. To do this, the assumption must be employed that the change in ^{3}He molar concentration through all of process II is small enough that the specific molar volume of the mixture remains approximately constant. If true, this would in turn mean that the total number of atoms in the control volume, whether ^{3}He or ^{4}He, must also be constant in time, as the dimensions of the control volume are not changing in time. Another interpretation of the assumption is that no molar storage occurs in the control volume over time, so that the total inlet molar flow rate must equal the total exit molar flow rate at any instant. This mole balance is written as

$$\frac{dn_{He}}{dt} = 0 = \dot{n}_{4He,in} + \dot{n}_{3He,in} - \dot{n}_{4He,out} - \dot{n}_{3He,out} \tag{3.22}$$

Due to the superleak at the inlet port, however, no normal fluid ^{3}He can enter the control volume. Knowing this, Equation 3.22 reduces to the following relationship:

$$\dot{n}_{4He,in} = \dot{n}_{4He,out} + \dot{n}_{3He,out} \tag{3.23}$$

The inlet ^{3}He and ^{4}He molar flow rates can be eliminated from the energy balance of Equation 3.21 using the relation in Equation 3.23 along with the knowledge that no ^{3}He enters through the superleak.

$$(\dot{n}_{4He,out} + \dot{n}_{3He,out})\mu_{4He} - \dot{n}_{3He,out}h_{os,out} - \dot{n}_{4He,out}\mu_{4He} + \dot{Q} = \frac{dU_{He}}{dt} \tag{3.24}$$

Simplifying this expression allows ^{4}He molar flow rate at the exit to drop from the equation.

$$\dot{n}_{3He,out}(\mu_{4He} - h_{os,out}) + \dot{Q} = \frac{dU_{He}}{dt} \tag{3.25}$$

Since the assumption has been made that no heat transfer occurs between the helium mixture and the cylinder walls, the only heat transfer across the helium control volume surface is with the GGG spheres. This heat transfer can be determined by applying the second law to the GGG control volume defined in Figure 3-5. Similar to the assumption made for process I, the temperature gradients within the GGG are assumed to be negligible, so the spheres are isothermal at the same temperature as the helium mixture. Also, the GGG spheres are assumed to be insulated from the cylinder wall such that the thermal interactions of the GGG are limited to

be exclusively with the helium mixture. The second law for the GGG control volume can then be written as

$$\dot{S}_{gen} - \frac{\dot{Q}}{T_{ii}} = \frac{dS_{GGG}}{dt} \tag{3.26}$$

The temperature of the system boundary T_{ii} is the temperature of the GGG *and* helium mixture contained within cylinder B, held constant during process II. Isolating the heat transfer term, setting the entropy generation to zero (since the process is reversible), and substituting into the helium energy balance of Equation 3.25 yields

$$\dot{n}_{3He,out}\left(\mu_{4He} - h_{os,out}\right) - T_{ii}\frac{dS_{GGG}}{dt} = \frac{dU_{He}}{dt} \tag{3.27}$$

This is the governing differential equation for process II in cylinder B. Like the governing equations for the processes described earlier, the thermodynamic properties for the GGG and helium mixture are known and can be substituted into this equation to relate the ^{3}He molar concentration, temperature, and applied field strength of the cylinder. Knowing the helium mixture properties are functions of ^{3}He molar concentration and temperature while the GGG properties are functions of temperature and applied field strengths, Equation 3.27 may be written as Equation 3.28. Note the time dependence of the ^{3}He molar concentration and applied field strength, as well as the constant temperature during process II. Also, the internal energy of the helium has been rewritten in terms of the specific internal energy – found via the equation of state – and the molar charge of ^{3}He contained in the control volume found by Equation 3.9.

$$\dot{n}_{3He,out}\left[\mu_{4He}(x(t)_{II},T_{ii})-h_{os,out}(x(t)_{II},T_{ii})\right]-T_{ii}n_{GGG}\frac{d[s_{GGG}(B(t)_{II},T_{ii})]}{dt}$$
$$=\frac{d\left[n_{3He,cyl}\left(x(t)_{II},V_{cyl},\gamma\right)u_{He}(x(t)_{II},T_{ii})\right]}{dt} \tag{3.28}$$

Finally a mole balance can be performed on the control volume for the ^{3}He. Since ^{3}He cannot be replenished through the superleak, the time rate of change of ^{3}He contained within the control volume must equal the rate leaving the exit port.

$$\dot{n}_{3He,out}=\frac{dn_{3He,cyl}}{dt}=\frac{dn_{3He,cyl}\left(x(t)_{II},T_{ii},V_{cyl},\gamma\right)}{dt} \tag{3.29}$$

Equation 3.29 is then substituted into Equation 3.28, resulting in the final form of the governing differential equation for process II, Equation 3.30.

$$\frac{dn_{3He,cyl}\left(x(t),T_{ii},V_{cyl},\gamma\right)}{dt}\left[\mu_{4He}(x(t)_{II},T_{ii})-h_{os,out}(x(t)_{II},T_{ii})\right]$$
$$-T_{ii}n_{GGG}\frac{d[s_{GGG}(B(t)_{II},T_{ii})]}{dt} \tag{3.30}$$
$$=\frac{d\left[n_{3He,cyl}\left(x(t)_{II},V_{cyl},\gamma\right)u_{He}(x(t)_{II},T_{ii})\right]}{dt}$$

To fully model the process, this equation must be integrated in time from state ii to state ii.

$$\int_{ii}^{iii} \frac{dn_{3He,cyl}\left(x(t)_{II}, T_{ii}, V_{cyl}, \gamma\right)}{dt} \left[\mu_{4He,in}(x(t)_{II}, T_{ii}) - h_{os,out}(x(t)_{II}, T_{ii})\right]$$
$$- \int_{ii}^{iii} T_{ii} n_{GGG} \frac{d\left(s_{GGG}(B(t)_{II}, T_{ii})\right)}{dt} \tag{3.31}$$
$$= \int_{ii}^{iii} \frac{d\left[n_{3He,cyl}\left(x(t)_{II}, V_{cyl}, \gamma\right) u_{He}(x(t)_{II}, T_{ii})\right]}{dt}$$

Equation 3.31 is the final integral form of the governing equation for process II in cylinder B. Unlike the equations developed for the processes I and III, this process involves flow of ^{3}He from the control volume, which is not constant in time. Due to this, the ^{3}He molar charge appears within the time integrand, resulting in a differential equation that is implicit with respect to the ^{3}He molar concentration. If the time path of the applied magnetic field, $B(t)_{II}$, is known along with the other constants in the equation – and it is here because it is a controllable parameter in the refrigerator that can be changed by increasing or decreasing the current to the superconducting magnets – Equation 3.31 can be numerically integrated to solve for the ^{3}He molar concentration in the cylinder as a function of time. With the time dependent ^{3}He molar concentration known, its time derivative can also be computed, according to Equation 3.29. In addition, the projected ^{4}He chemical potential can be computed from solution using the equation of state and is known as a function of time since it depends only on the pump temperature and ^{3}He concentration. This is shown in Equation 3.32. Both the ^{3}He molar flow rate and the projected ^{4}He chemical potential are needed as inputs to solve the recuperator submodel that is developed in the upcoming section.

$$\mu_{4He} = \mu_{4He}(x(t)_{II}, T_{ii}) \tag{3.32}$$

Similar to the equations developed to represent processes I and III, the Equation 3.31 defines a relation between states ii and iii specified only by the constant cylinder temperature and applied field strength path during the process, as the GGG porosity and cylinder volume are fixed by the design of the pump.

3.2.4 Process IV

The intake process is the last remaining to be modeled. For cylinder B, this occurs during process IV. The derivation for this step closely parallels that just derived for the pumping step, since this process is essentially the inverse of process II. Figure 3-6 shows a schematic of the entire pump assembly with the relative changes in the states of the helium mixture and GGG occurring during this process in addition to the direction of the helium flows. Figure 3-7 shows two control volumes necessary for this derivation – one containing only the *GGG spheres* within cylinder B and the other containing only the *helium mixture* within cylinder B.

Process IV, just like process II, involves convective flows of helium entering and leaving the cylinder. In this case, the flow directions are reversed from process II – ^{3}He-^{4}He mixture enters cylinder B through the inlet port, while pure superfluid ^{4}He exits through the superleak. Since no ^{3}He escapes through the superleak, the ^{3}He molar concentration increases during this process as ^{3}He atoms accumulate in the cylinder. Like process II, non-reversible mixing of helium isotopes occurs in the cylinder during this process as the ^{3}He molar concentration changes, accompanied by a generation of entropy. Because of this, the two control volume approach that was utilized to model process II is again used here; one control volume contains only the helium mixture within

cylinder B and thus captures all the irreversiblities, while the second control volume contains only the GGG and undergoes a reversible process. Again as in process II, the control volumes are coupled by the heat transfer between the GGG and the helium mixture.

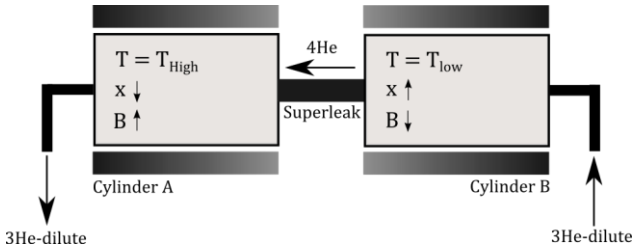

Figure 3-6: Schematic showing the relative states of the helium mixture and GGG in both cylinders during process IV. Also shown are the helium flow directions. GGG not shown for clarity

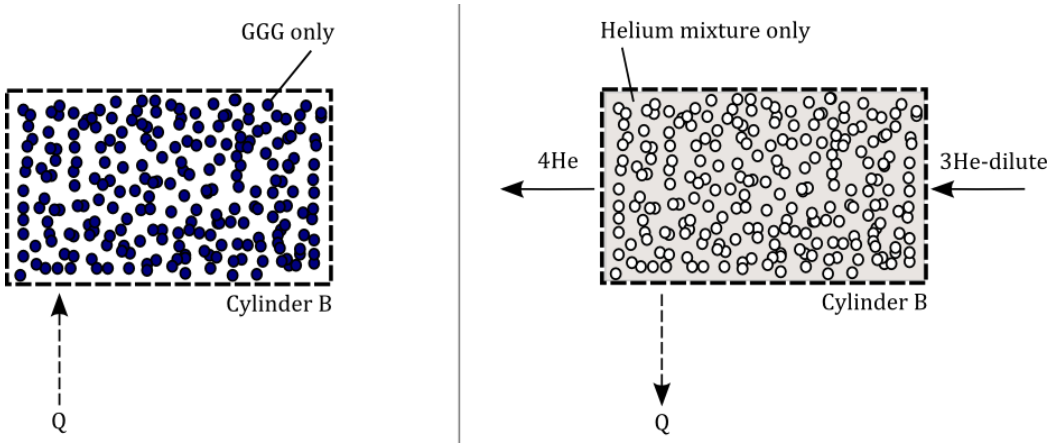

Figure 3-7: (a) Control volume containing only the GGG spheres contained in cylinder B and (b) control volume containing only the helium mixture in cylinder B, both for process IV.

Each of the assumptions listed previously for process II also apply for this intake process. In addition, it is assumed the helium enters the cylinder at the temperature of the precooling stage at all times during the process. This draws on the assumption made previously the precooling heat exchangers are perfectly effective. With this information, the governing equation for process IV

can be derived. Equation 3.31 is the general form of the first law applied to the helium control volume shown in Figure 3-7b.

$$\dot{n}_{He,in}h_{He,eff,in} - \dot{n}_{He,out}h_{He,eff,out} - \dot{Q} = \frac{dU_{He}}{dt} \tag{3.33}$$

Note that heat transfer here has been defined as positive for heat transfer *out* of the helium control volume, which differs from the definition for the analogous energy balance in process II. As discussed previously, a more useful form of the energy balance when using a superfluid isolates the energy fluxes associated with the superfluid and normal fluid flows. Again using Ebner's method, Equation 3.33 can be equivalently expressed as Equation 3.34 by substituting Equation 3.18 for the convective energy flux terms.

$$\dot{n}_{3He,in}h_{os,in} + \dot{n}_{4He,in}\mu_{4He} - \dot{n}_{3He,out}h_{os,out} - \dot{n}_{4He,out}\mu_{4He} - \dot{Q} = \frac{dU_{He}}{dt} \tag{3.34}$$

To eliminate the ^{4}He molar flow rates from the equation above, the same assumption that was made for process II holds here: the specific molar volume of the mixture remains approximately constant over the small range of ^{3}He molar concentration experienced in the cylinder. The consequence of this assumption is that no molar storage occurs in the control volume over time, so the total inlet molar flow rate must equal the total exit molar flow rate at any instant. This mole balance is written as

$$\frac{dn_{He}}{dt} = 0 = \dot{n}_{4He,in} + \dot{n}_{3He,in} - \dot{n}_{4He,out} - \dot{n}_{3He,out} \tag{3.35}$$

Since the exit port is a superleaked, however, no normal fluid ^{3}He can leave the control volume. Knowing this, Equation 3.35 reduces to

$$\dot{n}_{4He,out} = \dot{n}_{4He,in} + \dot{n}_{3He,in} \tag{3.36}$$

The outlet ^{3}He and ^{4}He molar flow rates can be eliminated from the energy balance of Equation 3.34 using the relation in Equation 3.36 and the knowledge that no ^{3}He exits through the superleak.

$$\dot{n}_{3He,in}h_{os,in} + \dot{n}_{4He,in}\mu_{4He} - \left(\dot{n}_{4He,in} + \dot{n}_{3He,in}\right)\mu_{4He} - \dot{Q} = \frac{dU_{He}}{dt} \tag{3.37}$$

Simplifying this expression allows the ^{4}He molar flow rate at the inlet to drop from the balance, leading to

$$\dot{n}_{3He,in}\left(h_{os,in} - \mu_{4He}\right) - \dot{Q} = \frac{dU_{He}}{dt} \tag{3.38}$$

With the assumption that no heat transfer occurs between the helium mixture and the cylinder walls, the only heat transfer across the helium control volume surface is with the GGG spheres. As with process II, the heat transfer between the GGG and the helium mixture can be obtained by writing the second law for the reversible process that occurs within the GGG control volume.

$$\dot{S}_{gen} + \frac{\dot{Q}}{T_{iv}} = \frac{dS_{GGG}}{dt} \tag{3.39}$$

The temperature of the system boundary T_{iv} is the temperature of the GGG *and* helium mixture contained within cylinder B, held constant during process IV. Isolating the heat transfer term, setting the entropy generation to zero (since the process is reversible), and substituting into the helium energy balance of Equation 3.38 gives the following relation

$$\dot{n}_{3He,in}\left(h_{os,in} - \mu_{4He}\right) - T_{iv}\frac{dS_{GGG}}{dt} = \frac{dU_{He}}{dt} \tag{3.40}$$

This is the governing differential equation for process IV in cylinder B. As in process II, the helium mixture properties are known functions of ^{3}He molar concentration and temperature while the GGG properties are known functions of temperature and applied field strengths, allowing Equation 3.40 to be written as

$$\dot{n}_{3He,in}\left[h_{os,in}\left(x(t)_{IV}, T_{iv}, T_{pc}\right) - \mu_{4He}(x(t)_{IV}, T_{iv})\right] - T_{iv}n_{GGG}\frac{d[s_{GGG}(B(t)_{IV}, T_{iv})]}{dt} = \frac{d\left[n_{3He,cyl}\left(x(t)_{IV}, V_{cyl}, \gamma\right)u_{He}(x(t)_{IV}, T_{iv})\right]}{dt} \tag{3.41}$$

Note that the inlet osmotic enthalpy is evaluated at the precooler temperature – since the precooling heat exchanger exit is assumed to be at a constant temperature T_{pc} at all times throughout processes I through IV – and at the same projected ^{4}He chemical potential as the mixture in the cylinder – since the projected ^{4}He chemical potential is assumed to be constant throughout the low pressure side of the system at all times due to the quasi-steady assumption. The projected ^{4}He chemical potential can be expressed as function of the cylinder ^{3}He molar

concentration and temperature, hence the dependence of the inlet osmotic enthalpy on three variables in this case.

Since the ^{3}He cannot exit through the superleak, the time rate of change of ^{3}He atoms within the control volume must equal the rate entering through the inlet port. This can be written as a ^{3}He mole balance on the helium control volume.

$$\dot{n}_{3He,in} = \frac{dn_{3He,cyl}}{dt} = \frac{dn_{3He,cyl}\left(x(t)_{IV}, T_{iv}, V_{cyl}, \gamma\right)}{dt} \tag{3.42}$$

Equation 3.42 is then substituted into Equation 3.41, resulting in the final form of the governing differential equation for process IV.

$$\begin{aligned} &\frac{dn_{3He,cyl}\left(x(t), T_{iv}, V_{cyl}, \gamma\right)}{dt}\left[h_{os,in}\left(x(t), T_{iv}, T_{pc}\right) - \mu_{4He}(x(t), T_{iv})\right] \\ &\quad - T_{iv} n_{GGG} \frac{d[s_{GGG}(B(t), T_{iv})]}{dt} \\ &\quad = \frac{d\left[n_{3He,cyl}\left(x(t), V_{cyl}, \gamma\right) u_{He}(x(t), T_{iv})\right]}{dt} \end{aligned} \tag{3.43}$$

To fully model the process, this equation must be integrated in time from state iv to state i.

$$\int_{iv}^{i} \frac{dn_{3He,cyl}\left(x(t)_{IV}, T_{iv}, V_{cyl}, \gamma\right)}{dt}\left[h_{os,in}\left(x(t)_{IV}, T_{iv}, T_{pc}\right) - \mu_{4He}\left(x(t)_{IV}, T_{iv}\right)\right]$$

$$- \int_{iv}^{i} T_{iv} n_{GGG} \frac{d[s_{GGG}(B(t)_{IV}, T_{iv})]}{dt} \tag{3.44}$$

$$= \int_{iv}^{i} \frac{d\left[n_{3He,cyl}\left(x(t)_{IV}, V_{cyl}, \gamma\right) u_{He}\left(x(t)_{IV}, T_{iv}\right)\right]}{dt}$$

Equation 3.44 is the final integral form of the governing equation for process IV in cylinder B. Its form is nearly identical to that of the equation developed for process II – differentiated only by sign changes caused by the opposite flow directions and the dissimilar boundary conditions – which is expected because they describe the same underlying physical process.

Unlike process II, where the time path of the applied magnetic field is a controllable parameter used to manipulate the ^{3}He molar flow rate, the time path of the applied magnetic field during process IV must be controlled such that the ^{3}He molar flow rate entering cylinder B is equal to the ^{3}He molar flow rate exiting cylinder A at all times during the cycle. This must occur in order to satisfy continuity, since the assumption is made that no helium mass storage occurs over time in the components outside of the pump cylinders. Due to the symmetry of the problem, this is the same as equating the ^{3}He molar flow rate leaving cylinder B during process II to the ^{3}He molar flow rate entering cylinder B during process IV at all times during the cycle. Equation 3.45 expresses this continuity relationship mathematically.

$$\frac{dn_{3He,cyl}\left(x(t)_{IV}, T_{iv}, V_{cyl}, \gamma\right)}{dt} + \frac{dn_{3He,cyl}\left(x(t)_{II}, T_{ii}, V_{cyl}, \gamma\right)}{dt} = 0 \tag{3.45}$$

Since the required time path of the ^{3}He molar flow rate is known from process II, Equation 3.44 can be numerically integrated to solve for the ^{3}He molar concentration in the cylinder as a function of time. Knowing this, the required time path of the applied magnetic field during process IV can then be determined. Also, as with process II, the projected ^{4}He chemical potential can be computed from solution using the equation of state – it is known as a function of time since it depends only on the pump temperature and ^{3}He concentration which both known at all times throughout the process. Both the ^{3}He molar flow rate and the projected ^{4}He chemical potential are needed as inputs, along with their corresponding values from process II, to solve the recuperator submodel that is developed in the upcoming section.

3.2.5 Additional constraints and definitions

Prior to solving the system of equations describing the pump submodel derived thus far, the number of variables in the system must be reduced by invoking known information about the pumping processes. In addition, a few variables of interest will be renamed in this section for more intuitive reference later in the paper.

To begin, the developed equation set refers to four temperatures, one for each state between the four processes. It has been discussed previously that the cylinder temperatures are constant during processes II and IV – the pumping and intake steps. Obviously it follows that, since the temperature is constant during these processes, the starting and ending temperatures must be equal as well. The temperatures at the start and end of process II and process IV are coupled by Equations 3.46 and 3.47, respectively. The pumping step, process II for cylinder B, occurs at the

maximum temperature T_{high} while the intake step, process IV for cylinder B, occurs at the minimum temperature T_{low}.

$$T_{ii} = T_{iii} = T_{high} \tag{3.46}$$

$$T_{iv} = T_{i} = T_{low} \tag{3.47}$$

Additionally, there are four ^{3}He molar concentrations explicitly present in the equation set, in addition to the unknown time dependent ^{3}He molar concentrations during the pumping and intake steps. Similar to the temperatures, the four ^{3}He molar concentrations in the equation set occur at the states between the four processes. It is known, however, that processes I and III occur at constant ^{3}He molar concentration. Due to this, the concentrations at the start and end of those cycles must identical. Equations 3.48 and 3.49 couple the ^{3}He molar concentrations at the start and end of process I and process III, respectively. Process I occurs after the intake process, so the ^{3}He molar concentration is at its highest value, while process III occurs after the pumping process, so the ^{3}He molar concentration is at its lowest value. The ^{3}He molar concentrations are relabeled to reflect this.

$$x_{i} = x_{ii} = x_{high} \tag{3.48}$$

$$x_{iii} = x_{iv} = x_{low} \tag{3.49}$$

Finally, it is known that the minimum applied magnetic field occurs at the end of the intake process (state i) and the maximum occurs at the end of the pumping process (state iii). The applied field strength variables at these states are relabeled appropriately.

$$B_i = B_{min} \tag{3.50}$$

$$B_{iii} = B_{max} \tag{3.51}$$

The four equations representing processes I through IV are now rewritten considering these constraints as Equations 3.52 through 3.55, respectively.

$$\begin{aligned} 0 = \; & n_{3He,i}(x_{high}, V_{cyl}, \gamma)\left[s_{He}(x_{high}, T_{high}) - \; s_{He}(x_{high}, T_{low})\right] \\ & + n_{GGG}(V_{cyl}, \gamma)\left[s_{GGG}(B_{ii}, T_{high}) - s_{GGG}(B_{min}, T_{low})\right] \end{aligned} \tag{3.52}$$

$$\begin{aligned} & \int_{ii}^{iii} \frac{dn_{3He,cyl}(x(t)_{II}, T_{high}, V_{cyl}, \gamma)}{dt}\left[\mu_{4He,in}(x(t)_{II}, T_{high}) - h_{os,out}(x(t)_{II}, T_{high})\right] \\ & \quad - \int_{ii}^{iii} T_{ii} n_{GGG} \frac{d\left(s_{GGG}(B(t)_{II}, T_{high})\right)}{dt} \\ & \quad = \int_{ii}^{iii} \frac{d\left[n_{3He,cyl}(x(t)_{II}, V_{cyl}, \gamma) u_{He}(x(t)_{II}, T_{high})\right]}{dt} \end{aligned} \tag{3.53}$$

$$0 = n_{3He,iii}(x_{low}, V_{cyl}, \gamma)\left[s_{He}(x_{low}, T_{low}) - s_{He}(x_{low}, T_{high})\right] + n_{GGG}(V_{cyl}, \gamma)\left[s_{GGG}(B_{iv}, T_{low}) - s_{GGG}(B_{max}, T_{high})\right] \tag{3.54}$$

$$\int_{iv}^{i} \frac{dn_{3He,cyl}(x(t)_{IV}, T_{low}, V_{cyl}, \gamma)}{dt}\left[h_{os,in}(x(t)_{IV}, T_{low}, T_{pc}) - \mu_{4He}(x(t)_{IV}, T_{low})\right] - \int_{iv}^{i} T_{iv} n_{GGG} \frac{d[s_{GGG}(B(t)_{IV}, T_{low})]}{dt} = \int_{iv}^{i} \frac{d\left[n_{3He,cyl}(x(t)_{IV}, V_{cyl}, \gamma) u_{He}(x(t)_{IV}, T_{low})\right]}{dt} \tag{3.55}$$

3.2.6 Implementation and solution procedure

The pump submodel, composed of the four coupled equations (3.52 through 3.55 above) derived for the pumping processes along with the constraints arising from the problem symmetry, must be solved simultaneously for a given set of operating and design parameters to obtain the associated time dependent ^{3}He molar flow rate and projected ^{4}He chemical potentials for the high and low pressure streams. Since the system is nonlinear, implicit in some of the unknown variables, and extremely stiff due to the characteristics of the equations of state, an iterative numerical method must be used to find the solution. Before discussing the solver details, however, it is worthwhile to review the set of unknown variables, design parameters, and controllable operating parameters needed to solve the system of equations. Table 3-2 organizes this information for reference.

Equation (and associated process)	Design parameters		Controllable operating parameters			[1]Unknown variables		
3.12 (I)	V_{cyl}	γ	B_{min}	T_{high}		B_{ii}	X_{high}	T_{low}
3.29 (II)	V_{cyl}	γ	$B(t)_{II}$	T_{high}		$x(t)_{II}$		
3.16 (III)	V_{cyl}	γ	B_{max}	[2]x_{low}	T_{high}	B_{iv}	T_{low}	
3.46 (IV)	V_{cyl}	γ	T_{pc}			T_{low}	$x(t)_{IV}$	$B(t)_{IV}$

Table 3-2: Summary of the variables and parameters occurring in each of the pump submodel equations

[1]The number of unknowns does not match the number of equations because $x(t)_{II}$ and $x(t)_{IV}$ are related by Eq. 3.45, which is not included in this table, and also because of the differential equations (the ^{3}He molar flow rate as a function of time falls out of the solution for the differential equations when the boundary conditions are satisfied).

[2]A value of x_{low} corresponds to a particular mixing chamber temperature/cooling power. For example, if all the controllable parameters are held constant and the load changes, x_{low} will shift, causing the unknowns to shift. The relation of x_{low} to the mixing chamber state will be discussed with the recuperator model derivation.

Table 3-2 organizes the variables in the pump submodel into three categories – design parameters that are constant over the entire pump cycle, controllable operating parameters, and the unknown values that are determined by the equation set. The cylinder volume and GGG porosity are design parameters that are constants over the entire pump cycle, whereas the controllable operating parameters are independent values that are specified to the pump submodel solver for a given operating condition. The choice of these independent parameters is driven practical control issues. For instance, the maximum and minimum applied field strengths (as well as the time rate of applied field strength increase during process II) can be directly controlled by varying the supply current to the superconducting magnets. The precooling temperature can also be independently adjusted, at least to some extent, by controlling the cryocooler refrigerating the stage. This is in contrast to the maximum cylinder temperature T_{high} and minimum concentration x_{low}, both of which are setpoints that can be independently varied if desired. With the design parameters and the controllable operating parameters set, the unknowns

are determined by solving the equation set. Most important for control of the system are the intermediate values of the applied magnetic field, B_{ii} and B_{iv}, required to maintain the specified operating conditions. The minimum pump temperature and maximum ^{3}He molar concentration, along with the time dependent cylinder concentrations and applied field strengths during the intake process, are also determined.

It is worthwhile to note here that one of the degrees of freedom provided by the independent setpoints T_{high} and x_{low} is removed when the system is coupled with the recuperator submodel and a cooling load is specified – that is, for a chosen T_{high} and cooling load, x_{low} is uniquely determined. The solution method used here accomplishes this calculation in reverse, rather, so the minimum pump concentration is independently varied while the remainder of the controllable operating parameters are held constant. This in turn varies the pump submodel solutions that are output into the recuperator submodel, resulting finally in a variation of the corresponding calculated cooling load. Since the minimum temperature achievable in the mixing chamber – the saturation temperature of the low pressure stream – is determined by the state of the helium in the low pressure side of the pump because of the constant ^{4}He chemical potential assumption, the mixing chamber temperature is also uniquely determined by varying x_{low} in such a procedure. Cooling power versus mixing chamber temperature curves for a set of constant controllable pump parameters developed in such a way will be discussed in the upcoming results section.

The procedure developed to solve the pump submodel must be capable of handling the implicit form and stiffness of the developed equation set in order to converge in within a reasonable time. To accomplish this, the model is implemented in Matlab and uses a combination of canned

numerical solution routines included with that software package and custom iterative solvers, the latter of which are developed to utilize known information specific to the problem at hand in an effort to reduce the computational time required as compared with simply using a generalized solution technique. The pump submodel solution procedure developed for this work is illustrated by the flow diagram in Figure 3-8.

To begin the solution process, all of the design and controllable operating parameters must be specified before the solver is invoked. This includes x_{low}, the lowest ^3He molar concentration occuring in the pump which has been broken out from the rest of the specified parameters in the chart because it is, as previously discussed, uniquely coupled to the mixing chamber cooling load and temperature if all of the remaining specified parameters are held constant. With these parameters specified, guess values are taken for the minimum pump temperature T_{low} and the maximum pump concentration x_{high}. At this point there is sufficient information to obtain the intermediate applied field strengths B_{ii} and B_{iv} by solving the equations for process I and process II. Matlab's fzero command – a routine included with the package to find the roots of non-linear equations – is used to solve these two equations since they are sufficiently continuous and non-stiff.

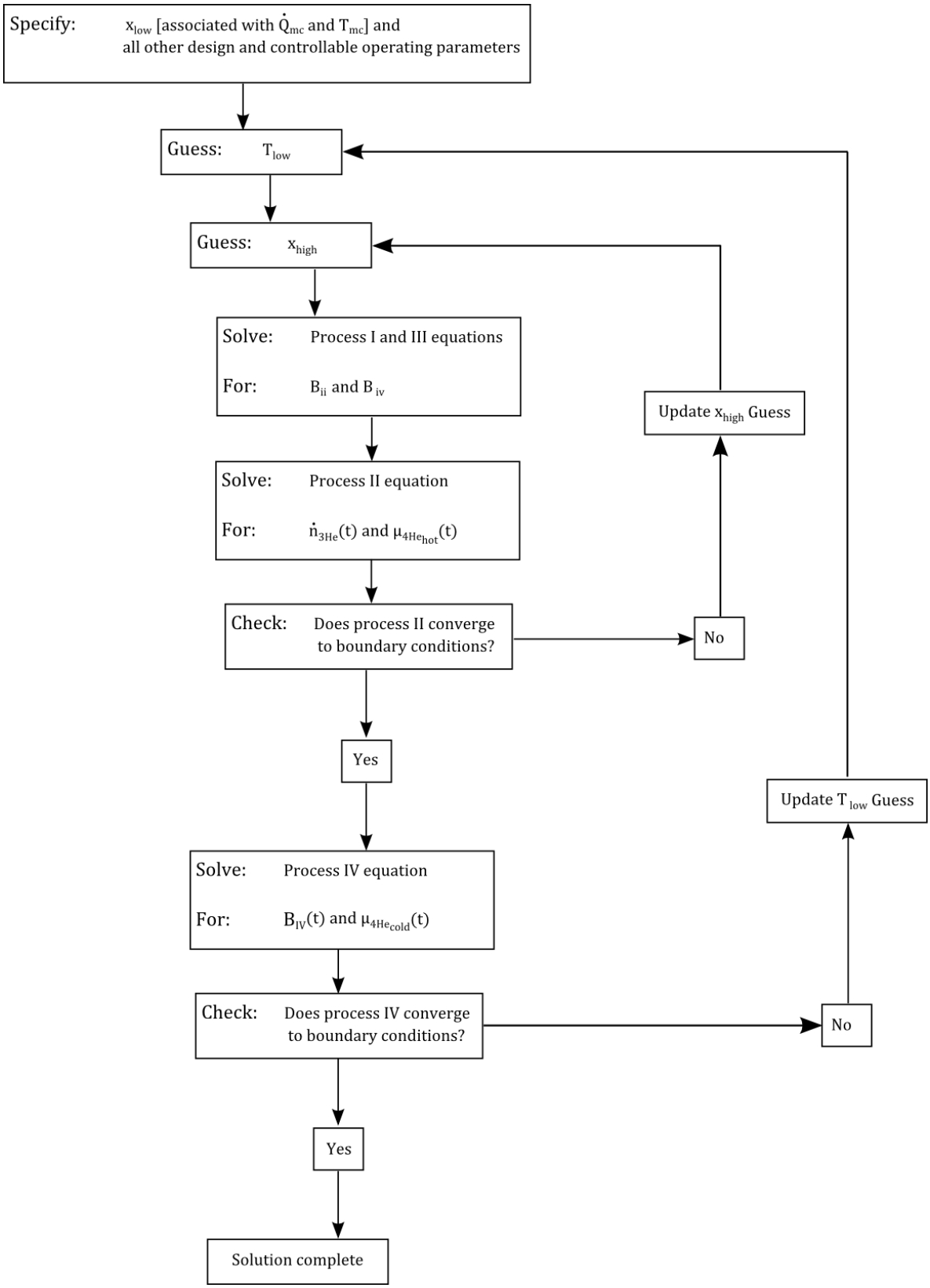

Figure 3-8: Flow diagram representing the iterative routine for the solution of the pump submodel

Following the determination of the intermediate applied field strengths, the equation for process II – the pumping step – is integrated. The chart abstracts the computational effort needed to perform this integration, which requires an implicit equation to be solved for *every time step* in the time integration. This duty is performed using Matlab's fmincon procedure – a routine included with the package to perform non-linear optimizations on non-continuous functions – since the procedure better handles the continuity issues that arise from the combination of bad guess values and the limited range of the helium mixture thermodynamic properties than does the fzero command. No matter the solver used here, this integration is the rate-limiting step for the pump model convergence time due to the complexity of the equation being solved. After the integration is completed, the computed boundary conditions are checked against the desired values. If the solution is not obtained, a new value of x_{high} is computed using a custom update routine; if the boundary conditions are satisfied, the solution to the equation for process III is converged and the correct value of x_{high} has been found. The ^{3}He molar flow rate and ^{4}He chemical potential for the high temperature stream are then determined as functions of time through the integration. Note that this computationally intensive step sits within two nested iterative solution schemes, compounding the solution time penalty incurred in this step.

The time path of the applied magnetic field for process IV and ^{4}He chemical potential for the low temperature stream are obtained next by solving the equation for process IV. This step again uses Matlab's fmincon optimization function to solve an implicit equation at each time step in the integration, although in this case the computational penalty is not as significant compared with process II because this step is contained within the outer solver loop rather than inside both loops. Upon completion of the integration, the computed boundary conditions are checked

against the desired values. If converged, the correct value T_{low} is found, concluding the solution process. If not, the guess value for T_{low} is updated a customized method and the routine is iterated until convergence is obtained.

3.3 Development of the recuperator submodel

The governing equations for the recuperator submodel are now derived for the refrigerator design, operation, and assumptions described in the previous chapter. Similar to the pump submodel, the governing equations are obtained by applying the first law to each of the components contained within the submodel. Unlike the pump submodel, however, the recuperator submodel is not analyzed as a transient system. Instead – as a means to reduce complexity of the problem – the recuperator submodel is solved at steady state using RMS values computed from the time dependent periodic pump submodel solution. As discussed previously, this will allow only an *estimate* of the RMS mixing chamber cooling power and temperature for a given set of specified pump operating parameters, rather than an exact solution at the RMS conditions, but will be adequate for the purposes of this proof-of-concept model.

Before deriving any governing equations, it is necessary to first define the RMS quantities required to apply the first law to the submodel components. The necessary information from the pump submodel solution to compute the RMS values includes the ^{3}He molar flow rate, high temperature stream projected ^{4}He chemical potential, and the low temperature stream projected ^{4}He chemical potential as functions of time throughout a single pumping-intake step. These known time dependent quantities are listed in the following equations.

$$\dot{n}_{3He} = \dot{n}_{3He}(t) \quad for\ 0 < t < t_{pump} \tag{3.56}$$

$$\mu_{4He_{hot}} = \mu_{4He_{hot}}(t) \quad for\ 0 < t < t_{pump} \tag{3.57}$$

$$\mu_{4He_{cold}} = \mu_{4He_{cold}}(t) \quad for\ 0 < t < t_{pump} \tag{3.58}$$

These time dependent values are valid for *all* pump cycles no matter which cylinder is providing the pumping, since the flow direction seen by the recuperator submodel is constant due to the rectification performed by the check valves. Note that the high pressure, high temperature stream will be referred to as the 'hot' stream and the low pressure, low temperature stream will be called the 'cold' stream from this point forward. The subscripts on the associated variables reflect this convention.

Knowing that each of the quantities listed in Equations 3.56 through 3.58 represents one cycle of a periodic waveform, the corresponding RMS values can be calculated according to Hayt (2007).

$$\dot{n}_{3He_{rms}} = \sqrt{\frac{1}{t_{pump}} \int_0^{t_{pump}} [\dot{n}_{3He}(t)]^2 dt} \tag{3.59}$$

$$\mu_{4He_{hot_{rms}}} = \sqrt{\frac{1}{t_{pump}} \int_0^{t_{pump}} \left[\mu_{4He_{hot}}(t)\right]^2 dt} \tag{3.60}$$

$$\mu_{4He_{cold_{rms}}} = \sqrt{\frac{1}{t_{pump}} \int_0^{t_{pump}} \left[\mu_{4He_{cold}}(t)\right]^2 dt} \tag{3.61}$$

The RMS subscript will be dropped from these variables in the derivations that follow for ease of reading.

3.3.1 Recuperator I

The first component of recuperator model to be developed is recuperator I, which is the heat exchanger closest to the pump assembly located adjacent to the check valve network. As noted in the design and operation section, the refrigerator design analyzed in this thesis employs concentric tube, counter flow heat exchangers for both recuperators I and III. Figure 3-9 shows the diameters necessary to define the cross-sectional geometry of such heat exchangers.

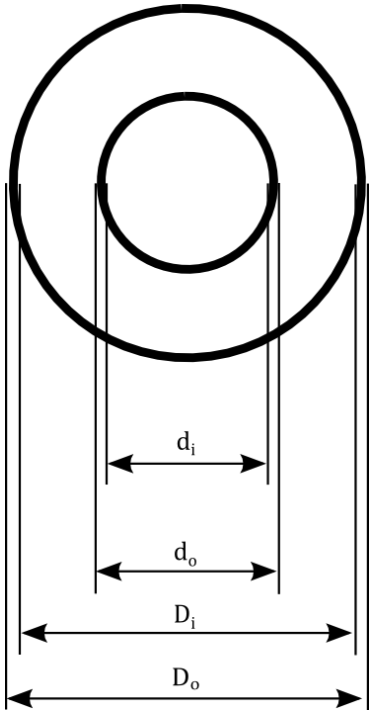

Figure 3-9: Definition of cross section geometry for recuperators I and III

Here d_i is the inner diameter of the inner tube, d_o is the outer diameter of the inner tube, D_i is the inner diameter of the outer tube, and D_o is the outer diameter of the outer tube. Additionally, the hydraulic diameter of the annulus is defined as

$$D_h = D_i - d_o \tag{3.62}$$

Because all simulations analyzed in this work use identical geometries for the cross sections of recuperators I and III, the values of the diameters are not subscripted to differentiate between the two recuperators. Also, the cold stream is designated to run through the annulus and the hot stream through the inner tube for both recuperators I and III.

With the cross sectional geometry defined, the governing equations for the recuperator can be derived by applying the first law to a set of differential control volumes within the recuperator. Figure 3-10 is a schematic that illustrates the overall geometry and helium flows of recuperator I, including the placement of the differential control volumes, while Figure 3-11 details the differential control volumes along with the quantities needed to apply the first law. For the following analysis, axial conduction and pressure drop are assumed to be negligible. While these assumptions are not explicitly checked in this work, the heat exchanger geometry, ^{3}He molar flow rates, ^{3}He molar concentrations, and thermal conductivity of the heat exchanger materials are all on the same order of magnitude used in the analysis of Miller (2005) for the modeling of heat exchangers in a superfluid Joule-Thomson refrigerator, in which case axial conduction and pressure drop were indeed found to be negligible.

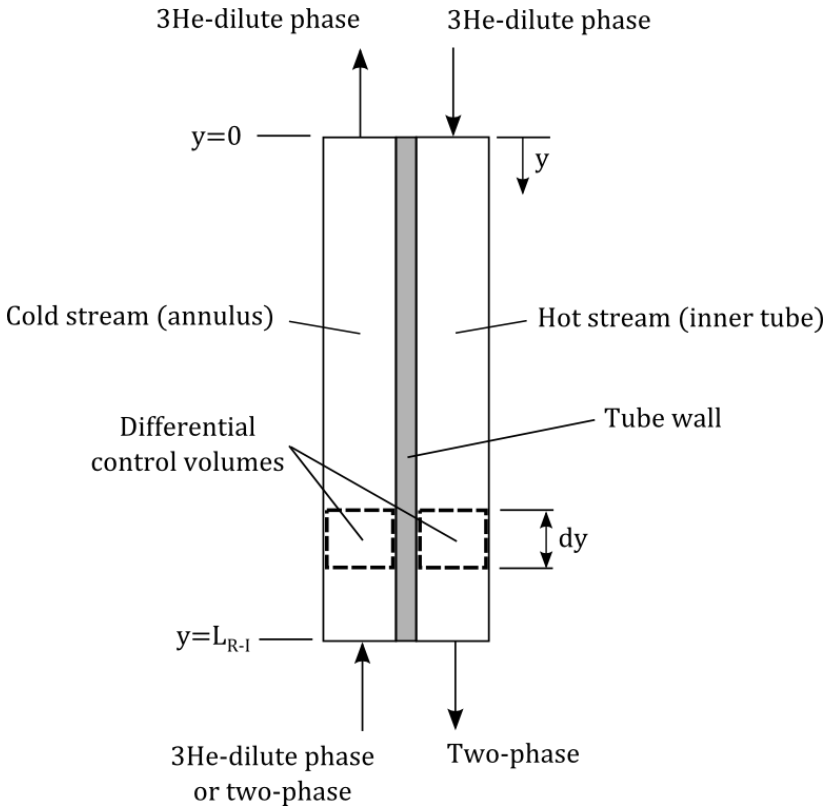

Figure 3-10: Schematic of the overall geometry profile and helium flows for recuperator I

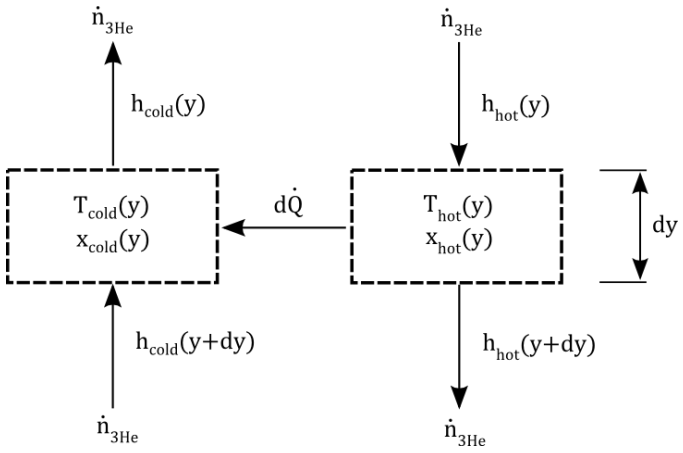

Figure 3-11: Differential control volumes for recuperator I

Observing the differential control volumes shown in Figure 3-11, the first law can be applied to the cold stream as

$$\frac{d\dot{H}_{cold}}{dy} = UA[T_{hot}(y) - T_{cold}(y)] \tag{3.63}$$

where $\dot{H}_{cold}$ is the enthalpy flow rate of the cold stream, U is the local overall heat transfer coefficient, A is the heat transfer area per unit length, T_{hot} is the temperature of the hot stream, T_{cold} is the temperature of the cold stream, and y is the axial position within the recuperator measured from the distance to the pump connection (the hot end of the recuperator, see Figure 3.10). In Equation 3.63, $d\dot{Q}$ from Figure 3-11 is replaced by the appropriate rate equation using the temperature difference between the two streams at axial position y. Rewriting in terms of the molar specific enthalpy, h_{cold}, and ^{3}He molar flow rate, $\dot{n}_{3He}$, gives

$$\frac{d[\dot{n}_{3He}h_{cold}]}{dy} = UA[T_{hot}(y) - T_{cold}(y)] \tag{3.64}$$

At steady state the ^{3}He molar flow rate is constant over all axial positions within the recuperator, allowing the ^{3}He molar flow rate to be removed from the derivative

$$\frac{d[h_{cold}]}{dy} = \frac{UA}{\dot{n}_{3He}}[T_{hot}(y) - T_{cold}(y)] \tag{3.65}$$

The local UA product, however, is a function of both geometry and the local heat transfer coefficients of both streams, owing to the convective resistance in each stream as well as the conductive resistance of the inner tube. The local UA product for a counterflow concentric tube heat exchanger is

$$UA = \frac{1}{\frac{1}{h_i(x_{hot})\pi d_i} + \frac{\ln\left(\frac{d_o}{d_i}\right)}{2\pi k_{ss}} + \frac{1}{h_o(x_{cold})\pi d_o}} \tag{3.66}$$

where h_i is the local heat transfer coefficient of the hot stream within the inner tube, h_o is the local heat transfer coefficient of the cold stream within the annulus, k_{ss} is the thermal conductivity of the stainless steel inner tube, and the diameters are as defined in Figure 3.9. The local heat transfer coefficients of both streams are highly dependent on their respective local ^{3}He molar concentrations since the thermal conductivity of the helium mixture is significantly depressed as the ^{3}He molar concentration increases. This dependence will be discussed in detail in an upcoming section; for now Equation 3.66 is used to rewrite the energy balance of Equation 3.65 showing the dependence of the local UA product on local ^{3}He molar concentrations.

$$\frac{d[h_{cold}]}{dy} = \frac{UA(x_{hot}, x_{cold})}{\dot{n}_{3He}}[T_{hot}(y) - T_{cold}(y)] \tag{3.67}$$

Expressing the molar specific enthalpy of the cold stream in terms of temperature, T_{cold}, and the molar specific heat capacity at constant ^{4}He chemical potential, $C_{\mu 4_{cold}}$, results in

$$\frac{d\left[C_{\mu 4_{cold}}(T_{cold}(y), \mu_{4He_{cold}})T_{cold}(y)\right]}{dy} = \frac{UA(x_{hot}, x_{cold})}{\dot{n}_{3He}}[T_{hot}(y) - T_{cold}(y)] \tag{3.68}$$

In this expression, the local value of the specific heat capacity at constant ^{4}He chemical potential of the cold stream depends on both the local cold stream temperature and its ^{4}He chemical potential that is constant throughout the heat exchanger.

Finally, if the fluid is in the superfluid ^{3}He-dilute phase, the local ^{3}He molar concentrations for each stream are determined as a function of the local stream temperature and projected ^{4}He chemical potential.

$$x_{cold} = x_{cold}\left(T_{cold}(y), \mu_{4He_{cold}}\right) \tag{3.69}$$

$$x_{hot} = x_{hot}\left(T_{hot}(y), \mu_{4He_{hot}}\right) \tag{3.70}$$

Substituting these relations, the differential energy balance takes its final form.

$$\frac{d\left[C_{\mu 4_{cold}}\left(T_{cold}(y), \mu_{4He_{cold}}\right)T_{cold}(y)\right]}{dy} = \frac{UA(T_{hot}(y), \mu_{4He_{hot}}, T_{cold}(y), \mu_{4He_{cold}})}{\dot{n}_{3He}}\left[T_{hot}(y) - T_{cold}(y)\right] \tag{3.71}$$

Equation 3.69 is the final form of the differential energy balance for the cold stream in recuperator I. An identical derivation is applied to the hot stream control volume in Figure 3.11, resulting in

$$\frac{d\left[C_{\mu 4_{hot}}\left(T_{hot}(y), \mu_{4He_{hot}}\right)T_{hot}(y)\right]}{dy} = \frac{UA(T_{hot}(y), \mu_{4He_{hot}}, T_{cold}(y), \mu_{4He_{cold}})}{\dot{n}_{3He}}\left[T_{hot}(y) - T_{cold}(y)\right] \tag{3.72}$$

Since the projected ^{4}He chemical potentials $\mu_{4He_{cold}}$ and $\mu_{4He_{hot}}$ are known from the pump submodel solution and are constant with axial position, Equations 3.71 and 3.72 are a set of coupled differential equations that can be integrated numerically over the length of recuperator I, $L_{R\text{-}I}$ in Figure 3-10, to find the temperatures of each stream as a function axial position within the recuperator.

Up to this point, the heat transfer coefficients for both the hot and cold streams have been simply stated as functions of the local ^{3}He molar concentration due the strong dependence of the thermal conductivity on the ^{3}He molar concentration. To see this dependence more clearly, the flow must first be characterized as laminar or turbulent in order to choose the proper heat transfer coefficient correlation. As was done to justify the neglect of axial conduction and pressure drop effects, the flow regime throughout the recuperator is assumed to be laminar due to the nearly identical design conditions when compared with the heat exchangers analyzed by Miller (2005), which were determined in that paper to be laminar. This assumption is based on the fact that the ^{3}He molar flow rates and tube diameters encountered in this work are comparable to within an order of magnitude to Miller's superfluid Joule-Thomson refrigerator. Miller finds that the maximum Reynolds numbers for the cold and hot stream are 92.1 and 63.7, respectively, for a ^{3}He molar flow rate of 100 μmole-^{3}He/s and nearly identical tube diameters as used in this work. As is evident from the simulations in the upcoming results section, ^{3}He molar flow rates of 100 μmole-^{3}He/s are typical for the cold cycle dilution refrigerator studied in this work, reinforcing the argument that the Reynolds numbers throughout recuperator system in this work are far below the critical value of 2300 and confirming the laminar flow assumption.

For fully developed laminar flow within concentric tubes – assuming that the outer tube surface is adiabatic, the inner tube is at constant temperature, and the ratio of the inner tube outer diameter to outer tube inner diameter d_o/D_i is equal to 0.5 – the Nusselt numbers for the inner tube (the hot stream) and annulus (the cold stream) are given according to Incropera (2007) as follows

$$Nu_i = Nu_{hot} = 5.74 \tag{3.73}$$

$$Nu_{annulus} = Nu_{cold} = 4.43 \tag{3.74}$$

The heat transfer coefficients for the inner tube and annulus can then be written in terms of the Nusselt number and thermal conductivity of the helium mixture by manipulating the Nusselt number definitions for the inner tube and annulus, again given by Incropera (2007).

$$h_{hot}(x_{hot}) = Nu_i \frac{k_{He}(x_{hot})}{d_i} = Nu_{hot} \frac{k_{He}(x_{hot})}{d_i} \tag{3.75}$$

$$h_{cold}(x_{cold}) = Nu_{annulus} \frac{k_{He}(x_{cold})}{D_h} = Nu_{cold} \frac{k_{He}(x_{cold})}{D_h} \tag{3.76}$$

The heat transfer coefficients defined in Equations 3.75 and 3.76 can be used with Equation 3.66 to define the local UA product as a function of the local ^{3}He molar concentrations in each stream. The functional dependence of the helium mixture thermal conductivity, plotted earlier in Figure 2-9 from data given by Lounasmaa (1974) and fit to a power law by Miller (2005), is nearly independent of temperature from 0.6 K to 1.2 K. Although some portions of the recuperator will

be subjected to temperatures extending below 0.1 K, any error incurred as a result of the temperature dependence will cause only small errors in the required recuperator length needed to meet a desired mixing chamber cooling load and temperature; such an inaccuracy does not disrupt the underlying physics of the machine and therefore is not detrimental in satisfying the proof-of-concept and first order component sizing goals of the model. The power law fit is given by

$$k_{He}(x) = 0.00145x^{-1.167} \tag{3.77}$$

Determining the thermal conductivity becomes a bit more complex when one or both of the streams contain two phase flow. Looking at the schematic in Figure 3-10, at least some portion of the hot stream in recuperator I must experience two phase flow since the hot stream must be at its saturation temperature when entering the phase separation chamber in order to be operating as a dilution refrigerator. At some pump operating conditions and mixing chamber cooling loads, the cold stream in recuperator I may also experience two phase flow. If the helium mixture for either stream is within the two phase region of the phase diagram, the thermal conductivity is assumed to be constant at a value estimated by Equation 3.77, determined using a ^{3}He molar concentration equal to an average of the ^{3}He molar concentration at the concentrate and dilute saturation lines for the known projected ^{4}He chemical potential of the stream. This approximation is stated as

$$k_{He}(x) = 0.00145\left[\frac{1}{2}\left(x_{sat,conc}(\mu_{4He}) + x_{sat,dilute}(\mu_{4He})\right)\right]^{-1.167} \tag{3.78}$$

Such an estimation is possible because the helium mixture thermal conductivity is no longer a significant function of ^{3}He molar concentration at the high concentrations experienced in the two phase region. Equation 3.77 and Figure 3-10 show this reduced dependence at high ^{3}He molar concentrations as compared to the strong dependence shown at concentrations below about 8 percent.

Estimating the thermal conductivity as a constant through a portion of the heat exchanger length in one or more of the streams at first appears to reduce the degrees of freedom in the coupled set of differential equations by an equivalent amount, but in such a situation the *actual* local ^{3}He molar concentration is no longer uniquely coupled to the temperature at the ^{4}He chemical potential of the stream as it is in Equation 3.69 or 3.70. This in turn frees a different variable in the equation set – the ^{3}He molar concentration of the two phase stream – so the degrees of freedom remains at zero even though the thermal conductivity is fixed in the two phase region. Note that for a constant ^{4}He chemical potential the temperature of a stream remains constant as the concentration changes across the two phase region; this is illustrated by the lines of constant projected ^{4}He chemical potential superimposed on the T-x diagram in Figure 2-7.

It is worth noting here that the two phase flow of ^{3}He-^{4}He superfluid and ^{3}He-^{4}He normal fluid is peculiar even by two phase flow standards. Unlike a typical two phase flow that characterized by large density differences between the components, the components of the two phase ^{3}He-^{4}He mixture are similar in density but may have vastly different thermal transport properties, especially as the temperature approaches zero and the ^{3}He molar concentration of the dilute phase drops to around 0.065. At such an extreme condition, the thermal conductivity likely

varies by an order of magnitude or more between the phases. Such flows have not been characterized or studied in the past and therefore cannot be accurately modeled. These conditions are encountered in some of the simulations completed for this work, in which case the thermal conductivity is simply estimated using Equation 3.78. As with the error attributed to the ignored temperature dependence of the thermal conductivity discussed earlier, such an estimation will not disprove the cold cycle dilution refrigeration concept, but rather increase the error in the predicted mixing chamber cooling powers for a specified recuperator sizing.

3.3.2 Recuperator II and phase separation chamber

The phase separation chamber and recuperator II are attached to the cold end of recuperator I, as illustrating in Figure 2-1. After leaving recuperator I as a two phase flow, the hot stream enters into the phase separation chamber where the ^{3}He-concentrate phase can be preferentially circulated to recuperator III and on to the mixing chamber. Recuperator II is simple tubular duct, thermally linked to the phase separation chamber through welds or brazes, that carries the cold helium stream returning from recuperator III back to recuperator I. The cold helium stream flowing through recuperator II is designed to be in thermal contact with the phase separation chamber this way in order to provide the cooling necessary to maintain a ^{3}He molar concentration increase from the inlet to the outlet of the phase separation chamber at steady flow conditions. In other words, the hot stream two phase mixture that enters the phase separation chamber must increase in ^{3}He molar concentration before it leaves through the exit of the chamber in the ^{3}He-concentrate phase, requiring heat removal if it occurs at steady state (which it does here due to the assumptions stated previously). Figure 3-12 is a simplified schematic of recuperator II and the phase separation chamber setup, with recuperator II represented by the

channel on the left side and the phase separation chamber represented as the channel on the right side. Figure 3-13 is a detailed breakout of the differential and finite control volumes used to apply the first law to recuperator II and the phase separation chamber, respectively.

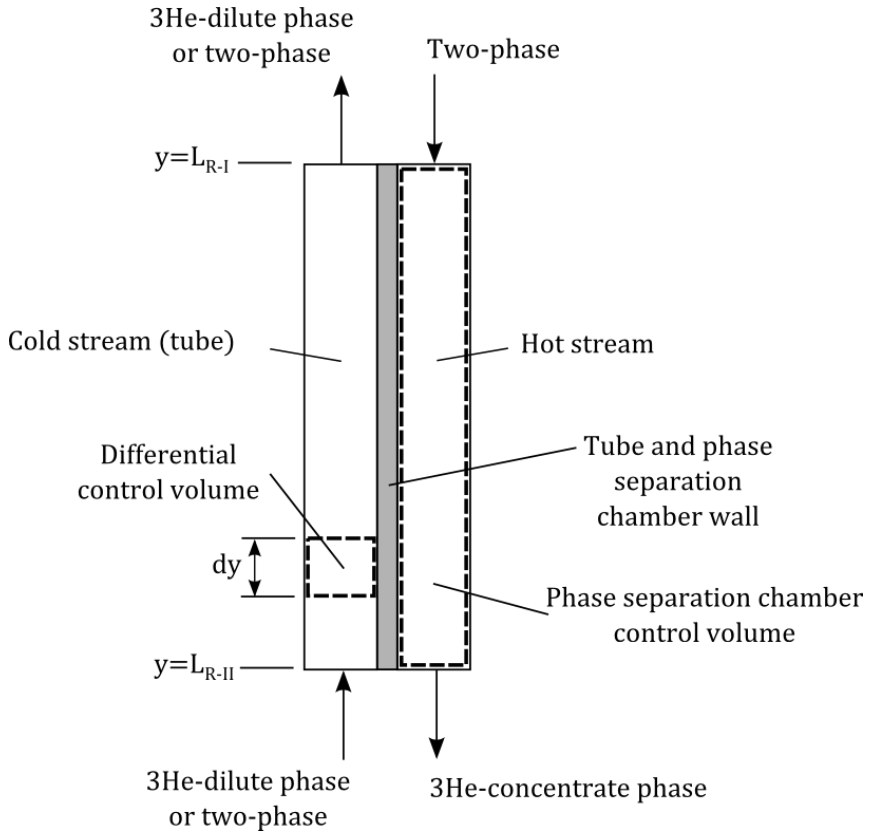

Figure 3-12: Simplified schematic of the overall geometry profile and helium flows for recuperator II and the phase separation chamber. In the actual setup, recuperator II (represented by the differential control volume) is physically wrapped around the cylindrical phase separation (whose control volume is not differential here, but rather consists of the entire helium volume within the chamber).

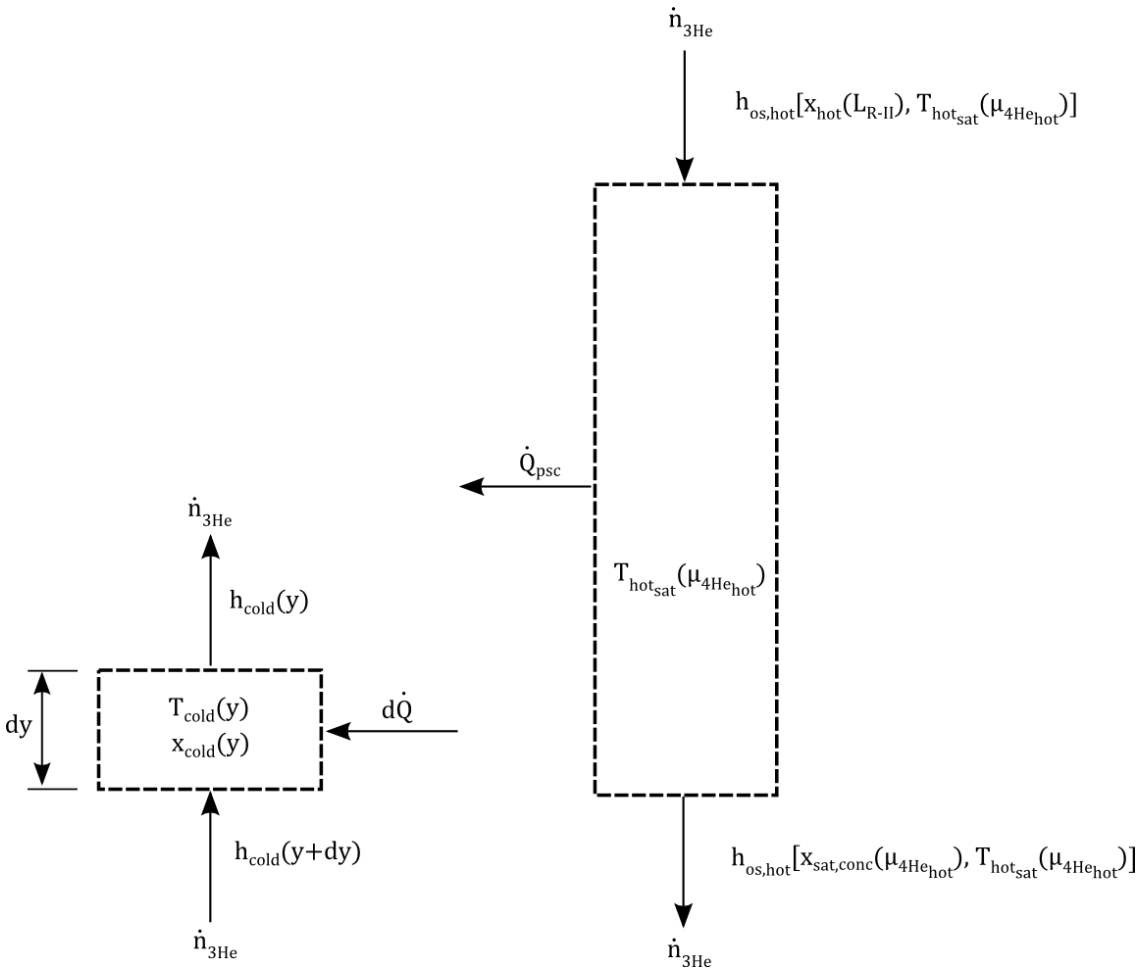

Figure 3-13: Control volumes for (a) recuperator I (differential) and (b) the phase separation chamber (non-differential)

The first law can be applied to recuperator II in much the same way as it was applied to recuperator I, although a few changes must be made to account for the different geometry. A slightly modified form of the recuperator I energy balance for the cold stream, given originally by Equation 3.65 and updated in Equation 3.79, is a good starting point for the derivation. The first few steps featured in the recuperator I derivation are skipped here because the same energy balance and rate equation applies for the recuperator II control volume.

$$\frac{d[h_{cold}]}{dy} = \frac{UA}{\dot{n}_{3He}}[T_{hot} - T_{cold}(y)] \tag{3.79}$$

This expression is identical to Equation 3.65 except that the hot stream temperature is now constant over all axial positions. The hot stream, housed within the phase separation chamber, is at uniform temperature over all axial locations of recuperator II because it is at its saturation temperature corresponding to its projected ^{4}He chemical potential.

The UA product also differs from the recuperator I derivation because of the geometry change, and is given as

$$UA = \frac{1}{\frac{1}{h_i(x_{cold})\pi d_i} + \frac{th_{wall,psc}+\mathrm{d_i}}{k_{ss} d_i}} \tag{3.80}$$

where $th_{wall,psc}$ is the thickness of the phase separation chamber wall and d_i is the inner diameter of the cold stream tube; the other variables are the same as in the recuperator I UA product, Equation 3.66. In the updated equation for recuperator II, the cold stream convection resistance term is identical to that for recuperator I, but the convection resistance for the hot stream has been left out completely and the conduction resistance term has been altered. Since the tube is welded or brazed to the phase separation chamber wall, the heat transfer area per unit length for conduction into the chamber is estimated to be the diameter of the tube. The conduction distance is pessimistically estimated to be the phase separation chamber wall thickness plus the entire tube diameter. Due to the relatively large surface area exposed to the hot stream inside the phase separation chamber coupled with the dominating effect of the conduction resistance, the hot stream convection resistance is assumed to be negligible. The UA product

given in Equation 3.80 then is only a function of the cold stream ^{3}He molar concentration and likely a weak one at that, due to the relatively high concentration that corresponds to the temperatures experienced at this location in the recuperator system.

The local heat transfer coefficient for the cold stream that appears in the expression for the local UA product is also different from recuperator I due to the difference in geometry. Again assuming laminar flow with constant surface temperature through the duct, the Nusselt number for the tubular geometry of recuperator II is given as follows by Incropera (2007)

$$Nu_{cold} = 3.66 \tag{3.81}$$

The local heat transfer coefficient for the cold stream is determined through the definition of the Nusselt number for recuperator II.

$$h_{cold}(x_{cold}) = Nu_{cold}\frac{k_{He}(x_{cold})}{d_i} \tag{3.82}$$

To obtain the dependence of the helium thermal conductivity, k_{He}, on ^{3}He molar concentration, Equation 3.77 developed for recuperator I can again be used here.

With the UA product known as a function of ^{3}He molar concentration, the final form of the differential energy balance for the cold stream can be rewritten in a form similar the final form derived for recuperator I as follows.

$$\frac{d\left[C_{\mu 4_{cold}}\left(T_{cold}(y), \mu_{4He_{cold}}\right)T_{cold}(y)\right]}{dy} = \frac{UA(T_{cold}(y), \mu_{4He_{cold}})}{\dot{n}_{3He}}[T_{hot} - T_{cold}(y)] = d\dot{Q} \quad (3.83)$$

Equation 3.83 can be integrated over then length of recuperator II to determine the temperature of the cold stream as a function of axial position in addition to the heat transfer rate between the phase separation chamber and recuperator II.

$$\dot{Q}_{psc} = \int_{L_{R-I}}^{L_{R-II}} d\dot{Q} \quad (3.84)$$

Note that the model allows for the possibility of two phase flow through the cold stream of recuperator II. At such an operating condition, the temperature of the low stream is fixed because the ^{4}He chemical potential is constant at all axial locations and the ^{3}He molar concentration must be determined by assuming a constant helium thermal conductivity in the two phase region of the heat exchanger. Details for this same scenario discussed in the previous section for recuperator I are also applicable here for recuperator II.

Applying the first law to the phase separation chamber is a relatively effortless process compared to the analysis of the recuperators. For the phase separation chamber, the inclusion of the temperature driven rate equation for heat transfer is avoided because since it has already been included in the governing equation developed for recuperator II. This means that the governing equation for the phase separation chamber can be derived purely in terms of the thermodynamics. Equation 3.85 is a restatement of the general form of the first law for control volumes using a superfluid ^{3}He-^{4}He mixture as the working fluid, originally stated in this thesis by Equation 3.21, with slight adjustments in the subscripts to refer to phase separation chamber

control volume shown in Figure 3-13. Here the total phase separation chamber heat transfer rate $\dot{Q}_{psc}$ couples the ^{3}He concentration process occurring within the phase separation chamber to the heat transfer rate allowed by recuperator II.

$$\dot{n}_{3He,in}h_{os,in} + \dot{n}_{4He,in}\mu_{4He} - \dot{n}_{3He,out}h_{os,out} - \dot{n}_{4He,out}\mu_{4He} - \dot{Q}_{psc} = \frac{dU_{He,psc}}{dt} \tag{3.85}$$

Under the assumptions stated for the recuperator model, the system is at steady state and at constant ^{4}He chemical potential, so the ^{3}He molar flow rate and ^{4}He chemical potential are equal at the inlet and exit of the phase separation chamber. This reduces Equation 3.85 to

$$\dot{Q}_{psc} = \dot{n}_{3He}\left(h_{os,in} - h_{os,out}\right) \tag{3.86}$$

In Equation 3.86, the osmotic enthalpy at the inlet is evaluated at the hot stream ^{3}He molar concentration at the cold end of recuperator I and the hot stream saturation temperature corresponding to its projected ^{4}He chemical potential. Likewise, the osmotic enthalpy at the exit is evaluated at the saturated ^{3}He molar concentration and temperature corresponding to the same hot stream ^{4}He chemical potential. The outlet osmotic enthalpy is evaluated at the saturated concentration because the ^{3}He-concentrate phase is preferentially circulated, by design, from the outlet of the phase separation chamber. Specifying the ^{3}He molar concentration at the phase separation chamber outlet in this way essentially sets one of the two boundary conditions for the recuperator submodel. The inlet and outlet osmotic enthalpies are stated formally stated in the following equations.

$$h_{os,in} = h_{os,in}\left(x_{hot}(L_{R-II}), T_{hot_{sat}}(\mu_{4He_{hot}})\right) \tag{3.87}$$

$$h_{os,out} = h_{os,out}\left(x_{sat,conc}(\mu_{4He_{hot}}), T_{hot_{sat}}(\mu_{4He_{hot}})\right) \tag{3.88}$$

Substituting Equations 3.87 and 3.88 into the energy balance Equation 3.86 completes the governing equation for the phase separation chamber.

3.3.3 Recuperator III

After exiting the phase separation chamber in the ^{3}He-concentrate phase, the hot helium stream is further cooled by the returning cool stream in recuperator III before entering the Joule-Thomson valve. Like recuperator I, recuperator III is a counterflow concentric tube heat exchanger with the hot stream in the inner tube and the cold stream in the annulus. Due to the equivalent geometries, the derivation of the governing equations for recuperator III closely parallels the derivation used previously to find the governing equations for recuperator I, although a few minor simplifications are added to accommodate the preferentially-circulated ^{3}He-concentrate phase in the hot stream of recuperator III. Figure 3-14 is a simplified schematic of the geometry and helium flows in the recuperator while Figure 3-15 details the differential control volumes for both streams and the properties required to apply the first law to each.

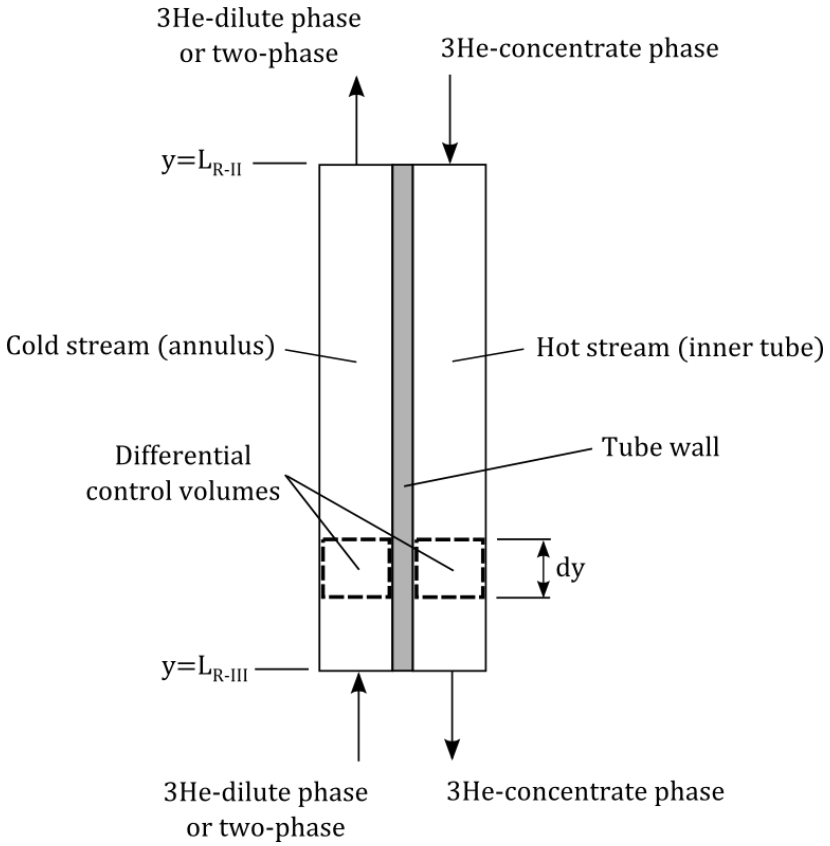

Figure 3-14: Schematic of the overall geometry profile and helium flows for recuperator III

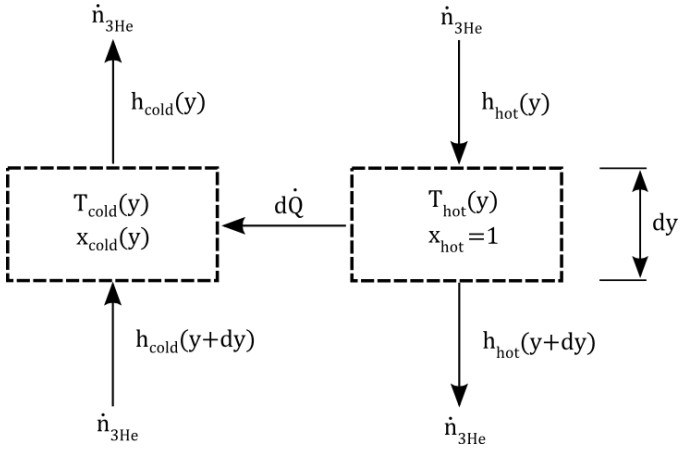

Figure 3-15: Differential control volumes for recuperator III

The differential control volume shown in Figure 3-15 is identical to that shown previously for recuperator I, with an exception for the fact that the hot helium stream is modeled thermodynamically as pure ^{3}He. All other assumptions discussed for recuperator I also apply

here including negligible pressure drop, negligible axial conduction, and laminar flow in both streams. Figure 3-9 defines the diameters here as it did for recuperator I.

The cold stream control volume in Figure 3-15 is identical to that of recuperator I, so little modification is needed to the equation developed previously for the cold stream in recuperator I, Equation 3.71, to apply it in this situation. Equation 3.89 restates that expression, applicable here for recuperator III, for completeness.

$$\frac{d\left[C_{\mu 4_{cold}}\left(T_{cold}(y), \mu_{4He_{cold}}\right) T_{cold}(y)\right]}{dy} = \frac{UA\left(T_{hot}(y), \mu_{4He_{hot}}, T_{cold}(y), \mu_{4He_{cold}}\right)}{\dot{n}_{3He}} \left[T_{hot}(y) - T_{cold}(y)\right] \tag{3.89}$$

In this equation, the UA product is essentially a function of only the hot and cold stream ^{3}He molar concentrations, as shown by Equation 3.66, but the equation is written in terms of the temperature and projected ^{4}He chemical potentials as per the equation of state relations given in Equations 3.69 and 3.70. For recuperator III, the concentration of the hot stream is assumed to be unity at all axial positions, allowing local UA product to lose its dependence on the hot stream temperature and projected ^{4}He chemical potential.

$$\frac{d\left[C_{\mu 4_{cold}}\left(T_{cold}(y), \mu_{4He_{cold}}\right) T_{cold}(y)\right]}{dy} = \frac{UA\left(T_{cold}(y), \mu_{4He_{cold}}\right)}{\dot{n}_{3He}} \left[T_{hot}(y) - T_{cold}(y)\right] \tag{3.90}$$

With no other differences to the recuperator I analysis to address, Equation 3.90 is the final form of the governing differential equation for the cold stream in recuperator III.

Similar changes are made to the governing equation for the hot stream in comparison to the result obtained for recuperator I. As a starting point, a form of the governing equation for the hot stream obtained in the recuperator I derivation, Equation 3.72, is restated as

$$\frac{d\left[C_{\mu 4_{hot}}\left(T_{hot}(y), \mu_{4He_{hot}}\right)T_{hot}(y)\right]}{dy} = \frac{UA(T_{hot}(y), \mu_{4He_{hot}}, T_{cold}(y), \mu_{4He_{cold}})}{\dot{n}_{3He}}[T_{hot}(y) - T_{cold}(y)] \tag{3.91}$$

The same simplification can be made here for the UA product functional dependence as was done previously for the cold stream equation. Since the hot stream for recuperator III behaves thermodynamically as pure ^{3}He and the pressure is considered constant at all axial locations, the specific heat capacity at constant ^{4}He chemical potential $C_{\mu 4_{hot}}$ can be replaced by the specific heat capacity for pure ^{3}He at constant pressure $C_{p_{3He}}$. Equation 3.91 can then be rewritten into the final form of the governing equation for the hot stream.

$$\frac{d\left[C_{p_{3He}}\left(T_{hot}(y)\right)T_{hot}(y)\right]}{dy} = \frac{UA(T_{cold}(y), \mu_{4He_{cold}})}{\dot{n}_{3He}}[T_{hot}(y) - T_{cold}(y)] \tag{3.92}$$

Equations 3.90 and 3.92 are the final set of coupled differential equations for recuperator III that must be integrated numerically over its length to solve for the hot and cold stream axial temperature profiles.

Finally, it is important to note that the local heat transfer coefficients used to determine the local UA product in recuperator III are found using the same Nusselt numbers incorporated in the recuperator I model, given for the hot and cold streams in Equations 3.73 and 3.74, respectively. Also, as with the other recuperators, the model allows for the possibility of two phase flow through the cold stream of recuperator III. As already discussed for the other recuperators, the temperature of the cold stream for the case of two phase flow is fixed because the ^{4}He chemical potential is constant at all axial locations. The ^{3}He molar concentration must then be determined by assuming a constant helium thermal conductivity in the two phase region of the heat exchanger. Details for this scenario discussed in the previous section for recuperator I are again applicable here for recuperator III.

3.3.4 Joule-Thomson valve and mixing chamber

Located adjacent to the cold end of recuperator III is the Joule-Thomson valve and mixing chamber assembly. After traveling through recuperator III, the hot stream – composed of the ^{3}He-concentrate phase – enters the Joule-Thomson valve where it is expanded adiabatically and at constant ^{4}He chemical potential due to the parallel superleak. The expanded ^{3}He-concentrate enters the mixing chamber where it mixes endothermically with the ^{3}He-dilute, by definition requiring an input of thermal energy. The cold stream leaves the mixing chamber as ^{3}He-dilute or a two phase mixture. Figure 3-16 is a simple schematic showing the control volume and helium flows used to analyze these mixing and expansion processes, while Figure 3-17 is a detailed control volume showing all quantities necessary to apply the first law to the system.

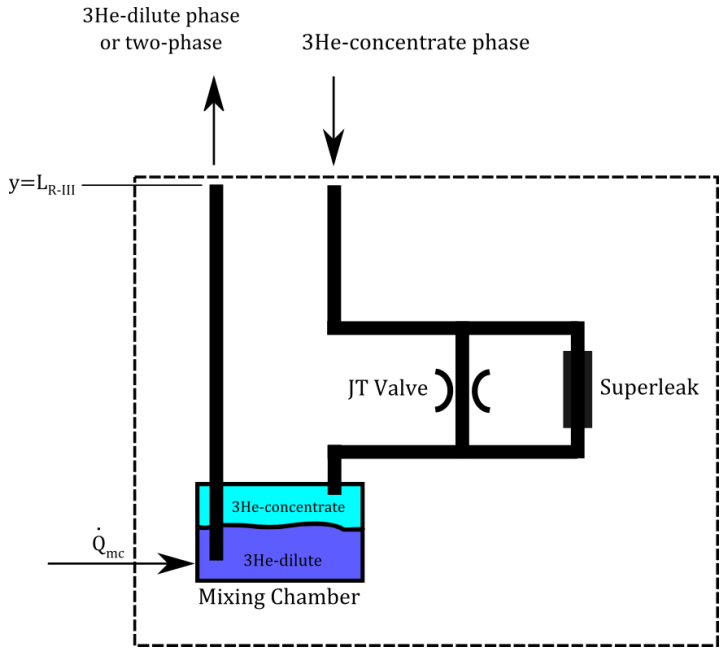

Figure 3-16: Schematic of the Joule-Thomson valve, superleak, and mixing chamber

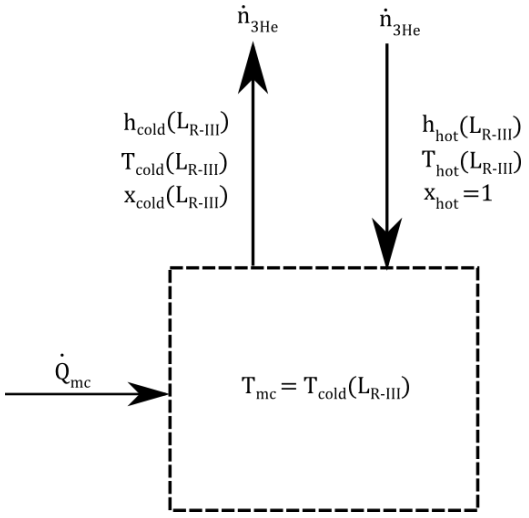

Figure 3-17: Control volume for the Joule-Thomson valve, superleak, and mixing chamber

To begin the derivation, the general form of the first law for control volumes with superfluids as the working fluid, originally given as Equation 3.21, is stated for the control volume consisting of the Joule-Thomson valve, superleak, and mixing chamber shown in Figure 3-17.

$$\dot{n}_{3He,in}h_{os,in} + \dot{n}_{4He,c}\mu_{4He} - \dot{n}_{3He,out}h_{os,out} - \dot{n}_{4He,out}\mu_{4He} + \dot{Q}_{mc} = \frac{dU_{He}}{dt} \qquad (3.93)$$

In this equation the subscripts refer to the helium mixture states at the inlet and exit of the control volume – that is, the inlet is the state of the hot helium stream at the cold end of recuperator III and the outlet is the state of the cold helium stream at the cold end of recuperator III. Since the system is evaluated at steady state conditions, the generic statement of the first law can be reduced to the following expression.

$$\dot{Q}_{mc} = \dot{n}_{3He}\left(h_{os,in} - h_{os,out}\right) \qquad (3.94)$$

Since the Chaudhry equation of state for ^{3}He-^{4}He mixtures used in this model was developed at zero pressure – and the inlet and outlet of the control volume considered here are by design at considerably different pressures – the energy balance in Equation 3.94 should be adjusted to account for the effect of pressure on the osmotic enthalpies. Following the method presented by Miller (2005) for an identical control volume on a superfluid Joule-Thomson refrigerator, the effect of pressure on the osmotic enthalpies can be accounted for by subtracting the pressure difference multiplied by the ^{3}He partial molar volume. The adjusted energy balance is

$$\dot{Q}_{mc} = \dot{n}_{3He}\left[\left(h_{os,in} - h_{os,out}\right) - (P_{in} - P_{out})v_{3He}\right] \qquad (3.95)$$

Here the osmotic enthalpies are evaluated from the ^{3}He molar concentrations and temperatures at the inlet and outlet of the control volume, while the projected ^{4}He chemical potentials for the hot and cold streams must also be specified to calculate the pressure difference between the streams.

An estimate of the ^{3}He partial molar volume can be found using Equation 3.8 along with the average ^{3}He molar concentration over the control volume inlet and outlet. Also, the ^{3}He molar concentration at the inlet is assumed to be unity because the hot stream in recuperator III is nearly pure ^{3}He.

$$\begin{aligned}\dot{Q}_{mc} = \dot{n}_{3He}\big[h_{3He,in}\big(T_{hot_{L-III}}\big) - h_{os,out}\big(x_{cold_{L-III}}, T_{cold_{L-III}}\big)\big] \\ - \big[P_{in}\big(T_{hot_{L-III}}, \mu_{4He_{hot}}\big) \\ - P_{out}\big(x_{cold_{L-III}}, T_{cold_{L-III}}, \mu_{4He_{cold}}\big)\big] v_{3He}\big(x_{cold_{L-III}}\big)\end{aligned} \tag{3.96}$$

Designating the temperature of the cold stream entering recuperator III as the mixing chamber temperature according to Equation 3.97, the energy balance can rewritten in its final form as Equation 3.98.

$$T_{cold_{L-III}} = T_{mc} \tag{3.97}$$

$$\begin{aligned}\dot{Q}_{mc} = \dot{n}_{3He}\big[h_{3He,in}\big(T_{hot_{L-III}}\big) - h_{os,out}\big(x_{cold_{L-III}}, T_{mc}\big)\big] \\ - \big[P_{in}\big(T_{hot_{L-III}}, \mu_{4He_{hot}}\big) \\ - P_{out}\big(x_{cold_{L-III}}, T_{mc}, \mu_{4He_{cold}}\big)\big] v_{3He}\big(x_{cold_{L-III}}\big)\end{aligned} \tag{3.98}$$

Equation 3.98 is the final form of the governing equation for the Joule-Thomson valve and mixing chamber, relating the mixing chamber cooling capacity to the ^{3}He molar flow rate and helium mixture states at the cold end of recuperator III. Note that the mixing chamber

temperature T_{mc}, depending on the cooling load applied to the mixing chamber, may or may not be the saturation temperature corresponding to the projected ^{4}He chemical potential of the cold stream.

3.3.5 Implementation and solution procedure

The governing set of differential and algebraic equations derived for the components in the recuperator submodel must be solved numerically and simultaneously to find the unknown mixing chamber temperature and cooling capacity associated with a given set of pump model parameters. Although each recuperator has a set of two coupled differential equations requiring two specified boundary conditions selected from the four temperatures at the inlet and outlet for both the hot and cold streams in order to solve – these governing equation sets for the individual recuperators and other components can be stitched together due to shared boundary conditions, essentially forming a single set of two coupled differential equations that represent the entire recuperator submodel. For example, the temperatures and ^{3}He molar concentrations occurring in the hot and cold streams at the cold end of recuperator I (at axial position $y = L_{R-I}$) are identical to those occurring at the hot end of the phase separation chamber and recuperator II, respectively. In other words, the states of the hot stream helium mixture leaving recuperator I and entering the phase separation chamber are identical, as are the states of the cold stream leaving recuperator II and entering recuperator I. Similar constraints can be applied to the interface between the phase separation chamber and recuperator II with recuperator III, as well as the recuperator III connection with the Joule-Thomson valve and mixing chamber.

The pair of coupled differential equations resulting from stitching the individual component equations together requires two boundary conditions to solve. These boundary conditions are chosen by specifying the temperature (or ^{3}He molar concentration since it is related to the temperature by the constant ^{4}He chemical potential assumption with Equations 3.69 or 3.70) at any two axial positions within the recuperator submodel for a given pump submodel solution. Values for the boundary conditions are have already been implicitly discussed in the derivations of the governing equations but will now be formally stated. One of the boundary conditions is specified by the assumption of perfect precooler effectiveness – the temperature of the hot stream leaving the precooler and entering recuperator I is always at temperature of the precooling stage.

$$T_{hot}(y = 0) = T_{pc} \tag{3.99}$$

The other boundary condition is specified by the fact that hot stream leaving the phase separation chamber is in the ^{3}He-concentrate phase – that is, the ^{3}He molar concentration of the hot stream leaving the phase separation chamber is constrained to the concentrated saturation line associated with its projected ^{4}He chemical potential, given by Equation 3.100.1. Such a condition also requires that the temperature at this location be at the corresponding saturation temperature, given by Equation 3.100.2.

$$x_{hot}(y = L_{R-II}) = x_{sat,conc}(\mu_{4He_{hot}}) \tag{3.100.1}$$

$$T_{hot}(y = L_{R-II}) = T_{hot_{sat}}(\mu_{4He_{hot}}) \tag{3.100.2}$$

With these constraints set, sufficient information is supplied to numerically solve the coupled set of governing differential equations for the axial recuperator temperature distributions and, of course, the corresponding mixing chamber cooling capacity and temperature. Recall that such a solution to the recuperator submodel is dependent on the pump submodel solution for a fixed set of controllable and design pump parameters. One pump submodel parameter – the lowest ^{3}He molar concentration that occurs in the pumping cycle x_{low}, is designated as the variable that varies with the mixing chamber cooling load if all other pump submodel parameters are held constant. In other words, a single value of x_{low} designated independently in the pump submodel corresponds to a unique mixing chamber temperature and cooling load predicted by the recuperator submodel. Varying x_{low} in the pump submodel then allows the performance of the refrigerator to be characterized by obtaining mixing chamber cooling power $\dot{Q}_{mc}$ versus mixing chamber temperature T_{mc} curves for all a constant set of controllable pump submodel parameters.

The numerical solution to the recuperator governing differential equations is most easily obtained by setting the temperatures of each stream at hot end of the recuperator (at axial position $y = 0$) and marching through the recuperator length, obtaining the temperatures at each axial position. To satisfy the boundary conditions specified by Equations 3.100.1 and 3.100.2 using this solution technique, however, requires iterating on the unknown temperature of the cold stream at the hot end of the recuperator (at axial position $y = 0$). Figure 3-18 highlights the details of the iterative scheme employed by the model to find the solution to the recuperator submodel.

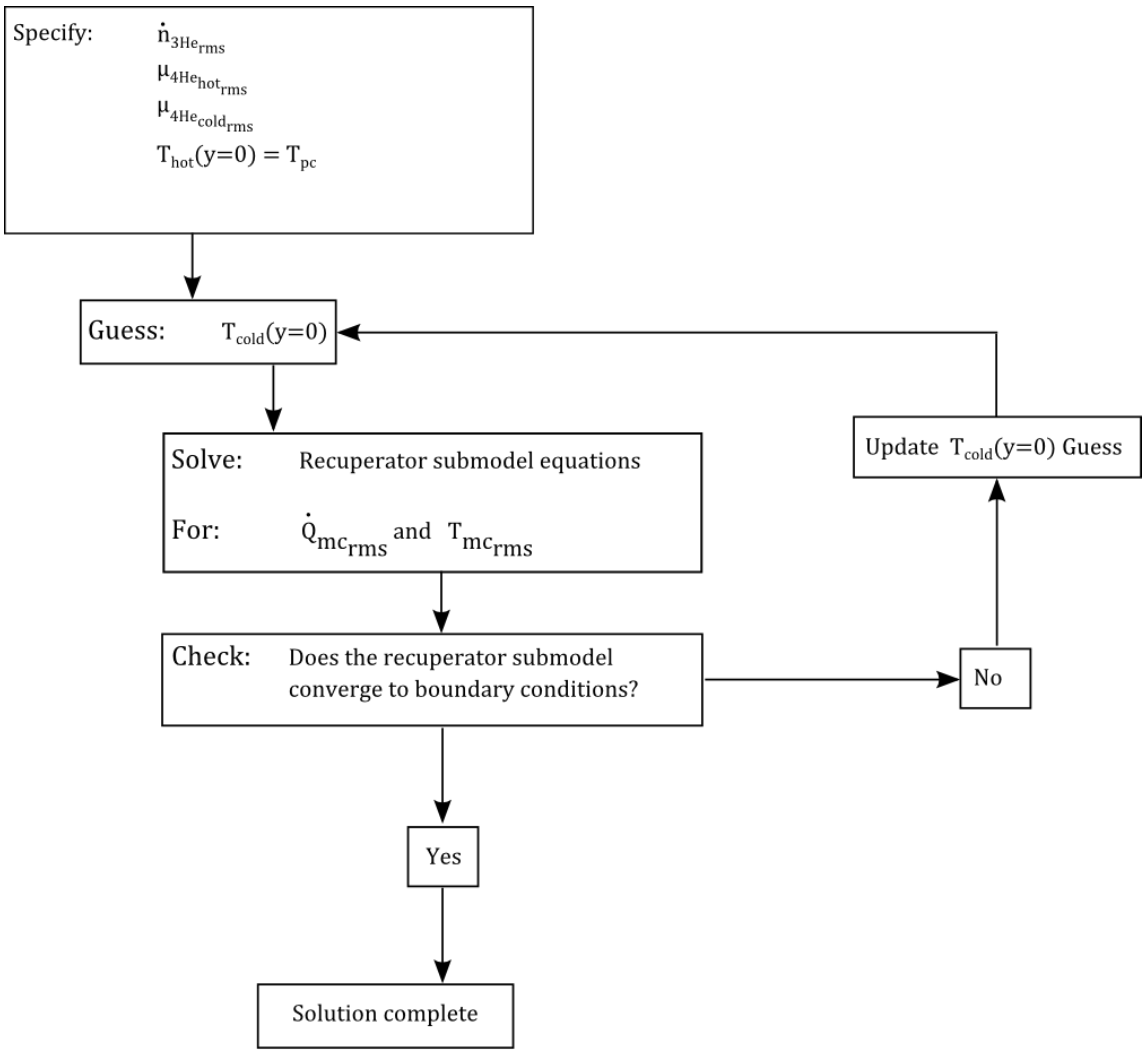

Figure 3-18: Flow diagram representing the iterative routine for the solution of the recuperator submodel

The method outlined in Figure 3-18 corresponds to a single set of pump model parameters, including x_{low}, and thus applies for a single mixing chamber cooling capacity and temperature. Prior to initiating, the solution process requires the RMS ^{3}He molar flow rate, $\dot{n}_{3He_{rms}}$, and projected ^{4}He chemical potentials for the hot and cold streams, $\mu_{4He_{hot_{rms}}}$ and $\mu_{4He_{cold_{rms}}}$, as obtained from the pump submodel solution. Also required is the precooler temperature T_{pc}, which is equal to the hot stream temperature at the hot end of recuperator I, $T_{hot}(y = 0)$. With these values set, a guess is made for the temperature of the cold stream at the hot end of

recuperator I, $T_{cold}(y = 0)$. A custom solution routine written in Matlab checks for convergence of the phase separation chamber boundary condition given by Equation 3.100.2 and updates the guess according. Upon convergence of the boundary conditions, the RMS mixing chamber cooling capacity and temperature are obtained for a given set of constant pump submodel settings and the solution of the recuperator submodel is complete.

3.4 References

Chaudhry, G., Thermodynamic properties of liquid ^{3}He-^{4}He mixtures between 0.15 K and 1.8 K, Ph.D. Dissertation, Massachusetts Institute of Technology, 2009.

Ebner, C. and Edwards, D., "The low temperature thermodynamic properties of superfluid solutions of ^{3}He in ^{4}He", Physics Reports, 2, 77-154, 1971.

Hayt, W. et al., Engineering circuit analysis, McGraw Hill, 2007.

Incropera, F. et. Al., Fundamentals of heat and mass transfer, Wiley and Sons, 2007.

Lounasmaa, O., Experimental principles and methods below 1 K, Academic Press, 1974.

Miller, F., "A simple method for the analysis of sub-Kelvin refrigerators that use a dilute superfluid ^{3}He-^{4}He mixture as a working fluid", Cryogenics 41, 311-318, 2001.

Miller, F., The development of a proof of principle superfluid Joule-Thomson refrigerator for cooling below 1 Kelvin, Ph.D. Dissertation, Massachusetts Institute of Technology, 2005.

Perry, D. and Phillips, S., Handbook of inorganic compounds, CRC Press, Boca Raton, 1995.

4 Results and discussion

Using the model developed in the previous sections, simulations were completed to analyze the performance of the cold cycle dilution refrigeration cycle for a variety of design and operating conditions. Table 4-1 lists the base set of model parameters held constant over all of the simulations in this chapter, unless otherwise noted. Each of the upcoming plots varies one of the parameters in this table from its base value while holding the others constant to study its effect on the performance of the system.

Parameter	**Symbol**	**Value**
High pump temperature	T_{high}	1.5 K
Precooler temperature	T_{pc}	1.1 K
Pump period	t_{pump}	2 min
Maximum applied field strength	B_{max}	3.0 T
GGG porosity	γ	38 %
Cylinder volume	V_{cyl}	12 cc
Recuperator I length	L_{R-I}	15.0 cm
Recuperator II length	L_{R-II}	8.0 cm
Recuperator III length	L_{R-III}	15.0 cm
Recuperator outer tube inner diameter	D_i	7.0 mm
Recuperator inner tube outer diameter	d_o	4.0 mm
Recuperator inner tube inner diameter	d_i	3.5 mm
Phase separation chamber volume	V_{psc}	2 cc
Mixing chamber volume	V_{mc}	2 cc

Table 4-1: Base case model parameters used for the simulations in this chapter

It is important to review here that the parameters in Table 4-1, as discussed in the model solution procedure in section 3.6.2, are controlled constants for all values of RMS mixing chamber temperature (and thus the coupled RMS mixing chamber cooling capacity). This means that for any of the upcoming plots where the RMS mixing chamber temperature or the coupled RMS

mixing chamber cooling capacity is independently varied, the parameters in Table 4-1 remain constant over the entire range of the independently varied quantity. Such a decision to hold the operating parameters in Table 4-1 constant when analyzing the performance of the refrigerator is a simple control scheme chosen for the proof-of-concept analysis of this work. More elaborate control schemes where the controllable operating parameters – for example the high pump temperature or pump period – can be adjusted for different cooling loads are possible but are beyond the scope of this thesis.

4.1 Cooling power and ^{3}He molar flow rate curves

Dilution refrigerator performance is best characterized by a plot of the cooling capacity as a function of the temperature at the cooling location for two reasons: (1) the available cooling capacity is constrained by the temperature at which the cooling is provided, and (2) the cooling capacity is crucial in determining the maximum size of the experiment requiring the refrigeration. For the cold cycle dilution refrigerator modeled in this work, this relation – simply referred to as a cooling power or capacity curve from this point forward – can be produced by plotting the RMS mixing chamber cooling capacity as a function of the RMS mixing chamber temperature for different sets of the model parameters listed in Table 4-1. Cooling power curves are compared in the forthcoming pages for various pump cylinder sizes, GGG porosities, precooler temperatures, pump periods, and recuperator lengths that vary from the base set of model parameters given in Table 4-1. To aid in explaining the cooling power trends, plots of the RMS ^{3}He molar flow rate as a function of the RMS mixing chamber temperature corresponding to each cooling power curve are also included.

4.1.1 Effect of pump cylinder volume

The effect of pump cylinder size on the cooling power curves is shown in Figure 4-1a, which plots cooling power curves for three different cylinder volumes, while Figure 4-1b plots the ^{3}He molar flow rate variation corresponding to the cooling curves listed in Figure 4-1a. To aid in understanding the cooling power curves, first observe the ^{3}He molar flow rate variation with mixing chamber temperature. The ^{3}He molar flow rates range from about 50 μmole/s to 140 μmole/s, depending on both the mixing chamber temperature and cylinder volume. Larger cylinder volumes produce larger flow rates at constant mixing chamber temperatures because both the GGG volume and void volume increase, allowing more ^{3}He to be pumped using the larger cylinder volumes for a fixed value of maximum field strength. The decrease in ^{3}He molar flow rate seen with higher mixing chamber temperatures is caused by the increase in ^{3}He molar concentration at the pump inlet as the cold end of the system reaches higher temperatures. Such a shift in concentration at the pump inlet is caused by the pressure increase of the low temperature stream associated with the temperature rise in the mixing chamber, coupled with the fact that the low temperature stream at the pump inlet is always fixed at the precooler temperature. Since the maximum field strength remains constant when the concentration shifts, more of the available field strength change must be used to cycle the pump temperature in processes I and III due to the increased heat capacity of the helium mixture at higher concentration, leaving less available field strength change to ramp during the pumping-intake processes II and IV. Decreasing the available field strength change during the pumping-intake processes, with the pumping period held constant, in turn causes a decrease in ^{3}He molar flow rates.

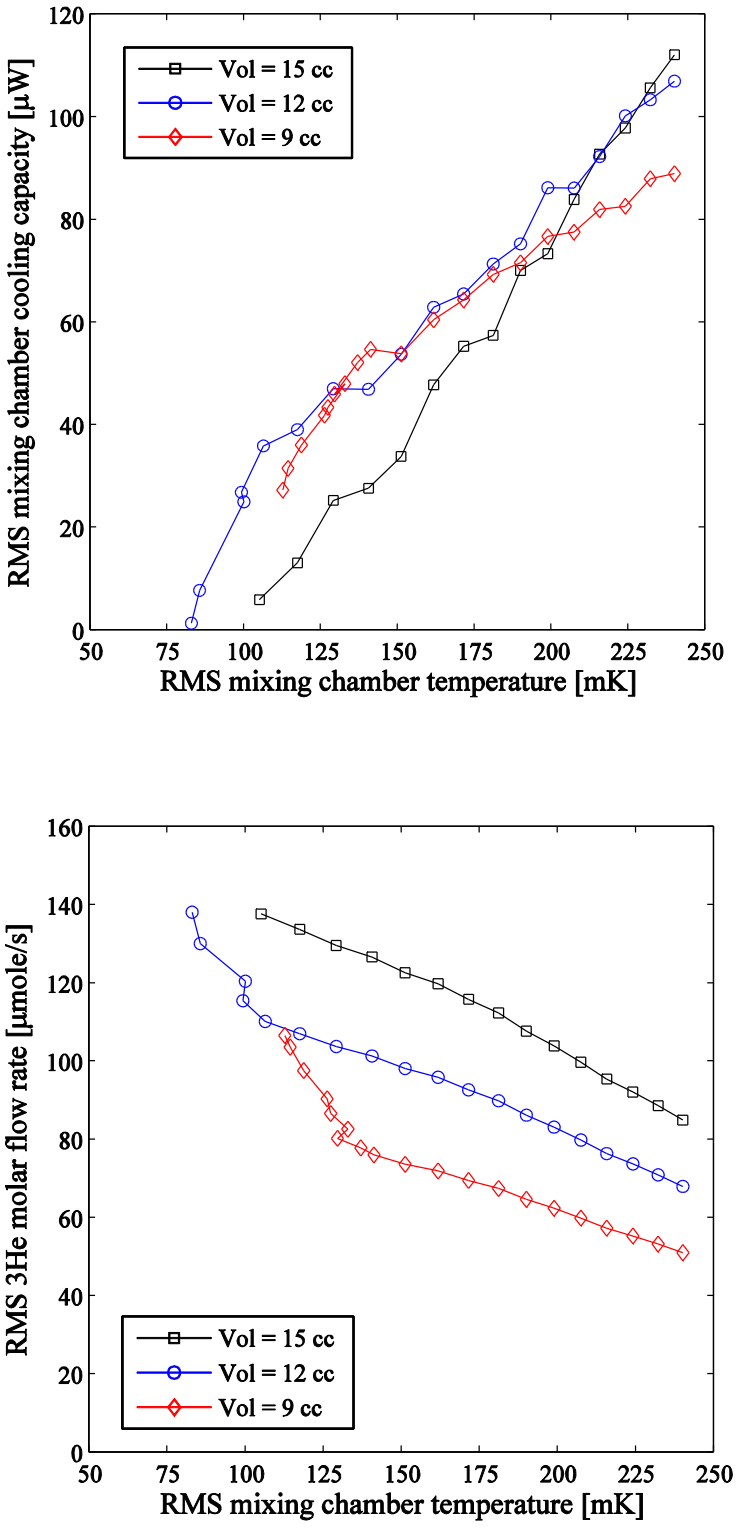

Figure 4-1: (a) RMS mixing chamber cooling capacity and (b) RMS ^{3}He molar flow rate variation with RMS mixing chamber temperature for multiple cylinder volumes and the base parameters given in Table 4-1

The RMS ^{3}He molar flow rates can now be used to help explain the cooling power curves in Figure 4-1a. At high mixing chamber temperatures, the cooling capacity scales with cylinder volume due to the higher ^{3}He molar flow rates associated with the larger volumes. At progressively lower mixing chamber temperatures, the pressure differential decreases significantly, causing any advantage from higher flow rates to be dwarfed by the increasing amount of cooling needed to concentrate the high temperature stream in the phase separation chamber relative to amount of cooling available from the enthalpy of mixing. At low mixing chamber temperatures, this causes the simulations with larger flow rates (the larger cylinder volumes) to have lower cooling capacities because the heat exchangers are less effective compared to the simulations with lower flow rates (the smaller cylinder volumes). Such behavior implies that larger cylinder volumes will allow greater cooling capacities at a given mixing chamber temperature because of the higher associated ^{3}He molar flow rates, given that the recuperator is sized appropriately to maximize the cooling power for the expected ^{3}He molar flow rate. Such an optimization will be studied in an upcoming analysis. Finally, note that for the cylinder volumes tested in these simulations the predicted mixing chamber temperature at no load (zero mixing chamber cooling capacity) varies with the cylinder volume, where the lowest of about 80 mK occurs for the cylinder volume of 12 cc.

The behavior of the cooling power and ^{3}He molar flow rate curves is further complicated by the fact that, for the smaller cylinder volume cases at low temperatures, the recuperators are sufficiently effective that none of the enthalpy of mixing is required to cool the incoming hot stream ^{3}He-concentrate within the recuperator network prior to expansion. This is in contrast to the situation that occurs at higher mixing chamber temperatures and larger cylinder volumes, in

which some portion of the enthalpy of mixing is required to cool the incoming high temperature ^{3}He-concentrate stream. In the latter case, some length of the low temperature recuperator stream must experience two phase flow at the same temperature as the mixing chamber, in turn causing the mixing chamber cooling capacity to be less than the enthalpy of mixing because some of the endothermic mixing enthalpy change is used to cool the hot stream in the recuperator rather than contribute to the cooling load in the mixing chamber. Conversely, the former case results in a single phase throughout the low temperature stream in the recuperator network, but the maximum temperature that occurs in the mixing chamber is greater than the saturation temperature for the low temperature stream. This occurs because the enthalpy increase associated with the temperature rise of the single phase superfluid within the mixing chamber contributes to the mixing chamber cooling capacity, in addition to the enthalpy of mixing. As a result, the reported cooling capacity is greater than the enthalpy of mixing but the temperature at which some of the cooling occurs is higher than the saturation pressure. The highest temperature occurring in the mixing chamber is always the temperature plotted for the cooling power and ^{3}He molar flow rate curves above, even if some portion of the cooling occurs at the lower saturation temperature. This is analogous to superheating a pure refrigerant in the evaporator of a vapor-compression cycle and reporting the superheated temperature, instead of the saturation temperature, as the evaporator temperature.

The transition between these cooling regimes, as they will be referred to from this point forward, can be seen most easily with the abrupt change in slope of the ^{3}He molar flow rate in Figure 4-1b. For the 12 cc case, this transition happens around 100 mK; for the 9 cc case it occurs at about 125 mK. To the right of the transition – at higher temperatures – some of the enthalpy of mixing

is used to cool the incoming hot recuperator stream, causing the cooling capacity to be lower than the enthalpy of mixing. To the left of the transition, the enthalpy change associated with raising the temperature of the single phase superfluid within the mixing chamber causes the cooling capacity to be larger than the enthalpy of mixing but raises the maximum temperature at which cooling occurs above the saturation temperature. At the discontinuity, the cooling capacity is equal to the enthalpy of mixing. The shift in these cooling regimes occurs at lower mixing chamber temperatures for higher pump volumes and is responsible for the crossover in the cooling power curves for the 9 cc and 12 cc simulations occurring near 130 mK in Figure 4-1a.

4.1.2 Effect of GGG porosity

The effect of another adjustable design parameter, the GGG porosity, on the cooling power curves is studied next. Figure 4-2a shows the cooling power curves for three values of GGG porosity, while Figure 4-2b plots the ^{3}He molar flow rate variation corresponding to the cooling power curves listed in Figure 4-2a. At each porosity tested, the same trends hold true for the ^{3}He molar flow rate and cooling capacity for increases in the mixing chamber temperature as did in the previous analysis; the ^{3}He molar flow rate decreases and the cooling capacity increases as the mixing chamber temperature rises. Such trends occur for the same reasons as discussed for Figure 4-1. The key consequence of increasing the porosity, however, is to decrease the ^{3}He molar flow rate at a given mixing chamber temperature – seen in Figure 4-2b. This happens because the ratio of GGG mass to helium mass within the cylinder decreases as the porosity increases, reducing the amount of thermal energy that can be transferred to the helium mixture for a given change in field strength, reducing the ^{3}He molar flow rate.

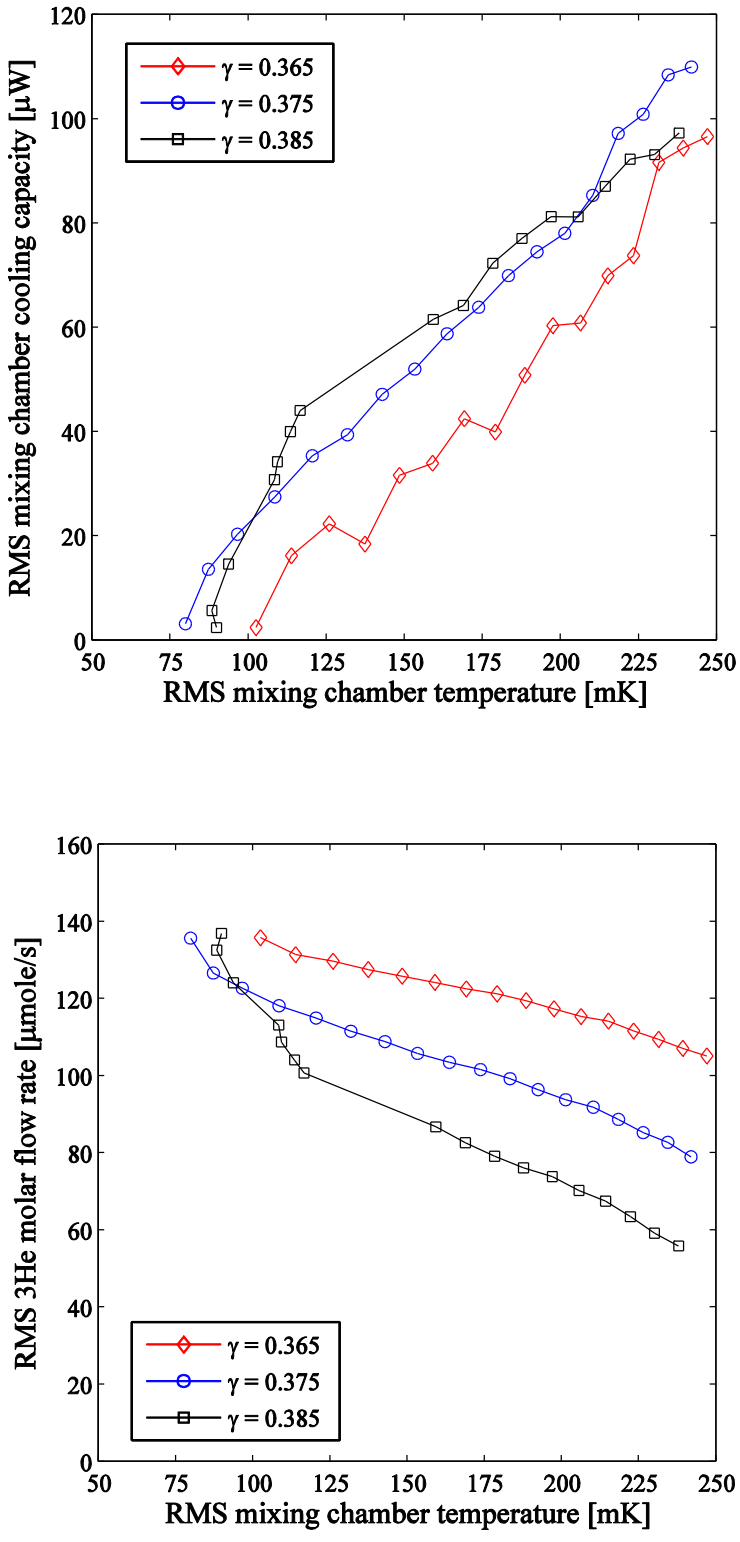

Figure 4-2: (a) RMS mixing chamber cooling capacity and (b) RMS ^{3}He molar flow rate variation with RMS mixing chamber temperature for multiple GGG porosities and the base parameters given in Table 4-1

The effect of the GGG porosity on the cooling capacity is a bit less clear, however, since the same phenomenon occurs here as did for the previous analysis over multiple cylinder volumes – the increase in recuperator effectiveness caused by the lower ^{3}He molar flow rates dominates over any effect of the porosity change on the pressure differential. As a result, the GGG porosity cases with the lowest ^{3}He molar flow rates produce the highest cooling capacities over most of the mixing chamber temperature range in Figure 4-2a. At lower mixing chamber temperatures, crossover is again seen between the two lower flow rate cooling power curves because of the change in cooling regimes. Most importantly, however, is that an optimum recuperator size exists that maximizes the cooling capacity exists for a given GGG porosity, as it did for the different cylinder volumes, due to the relation between the GGG porosity and the ^{3}He molar flow rate. Again, finding this optimum will be addressed in an upcoming analysis.

4.1.3 Effect of precooler temperature

With the effect of two design parameters on the refrigerator performance addressed, it is worthwhile to study the effects of some of the key controllable operating parameters on the cooling power and ^{3}He molar flow rate curves. In this section, the consequences of varying the precooler temperature are analyzed. Figure 4-3a shows the cooling power curves for three precooler temperatures, while Figure 4-3b plots the ^{3}He molar flow rate variation corresponding to the cooling curves listed in Figure 4-3a.

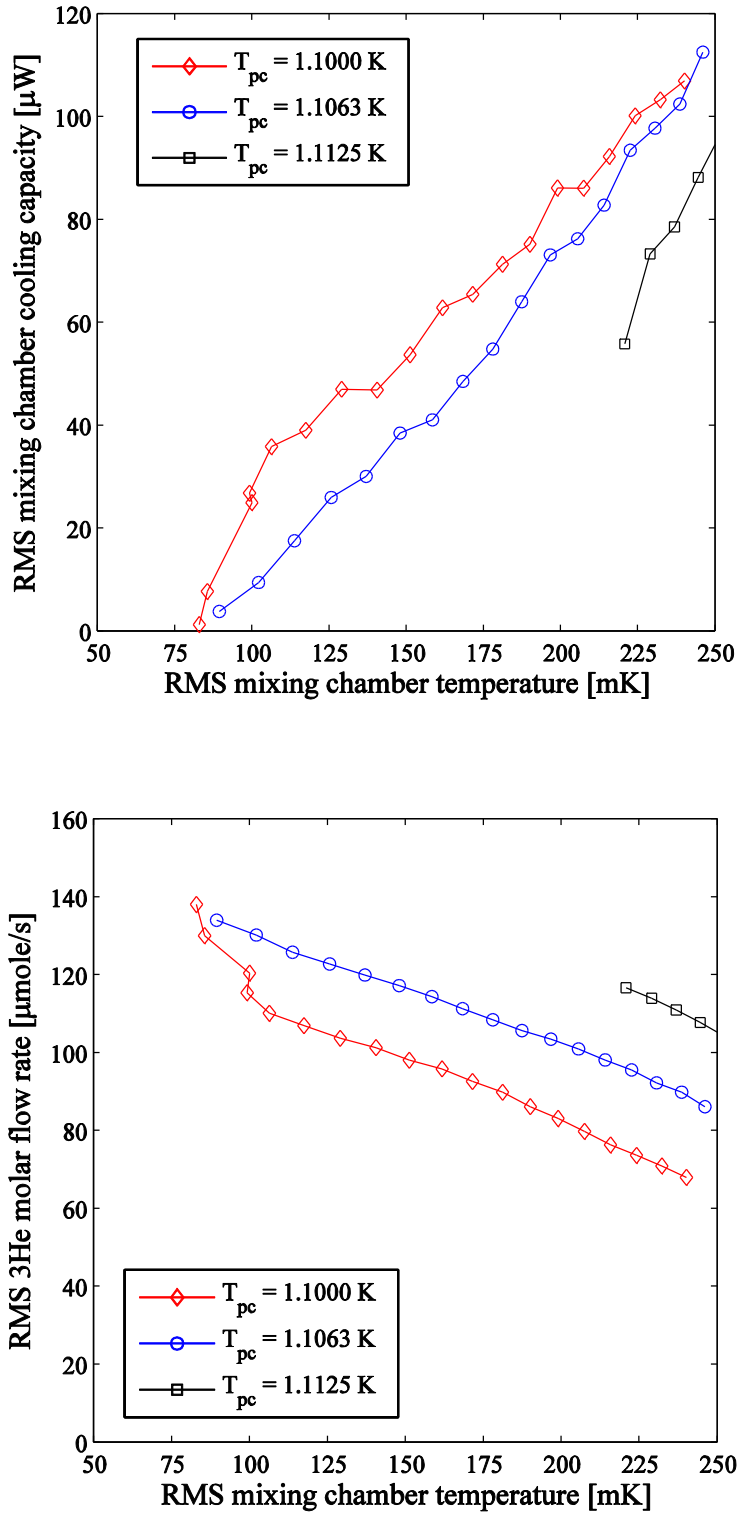

Figure 4-3: (a) RMS mixing chamber cooling capacity and (b) RMS ^{3}He molar flow rate variation with RMS mixing chamber temperature for multiple precooler temperatures and the base parameters given in Table 4-1. For these plots V_{cyl} = 9 cc, which varies from the base case.

For each precooler temperature studied, as with the plots for the previous simulations, the cooling capacity and ^{3}He molar flow rates increase and decrease, respectively, with the mixing chamber temperature. Decreasing the precooler temperature, however, results in lower ^{3}He molar flow rates. This happens because the helium returning to the pump is colder, and thus has less internal energy, when the precooler temperature drops. Consequently, more heat must be transferred to the low temperature helium charge in process I to raise its temperature when the precooler temperature is decreased, leaving less available field strength change for the pumping-intake processes. Since the maximum field strength is held constant, lower ^{3}He molar flow rates result. This same effect is responsible for constraining the system such that low mixing chamber temperatures cannot be attained at high precooler temperatures, as is the case for the simulation with the 1.1125 K precooler temperature in Figure 4-3. Also, note the extreme sensitively of both the cooling power curves and ^{3}He molar flow rate curves to small changes in the precooler temperature.

As with the plots for the previous simulations, the behavior of the cooling power curves is influenced greatly by the effect of the ^{3}He molar flow rate on the recuperator effectiveness. The highest cooling capacity at a given mixing chamber temperature in Figure 4-1a occurs with the precooler temperature that produces the lowest flow rate, which also has the highest recuperator effectiveness. The cooling regime transition seen with the other simulations is again observed here, particularly for the 1.100 K precooler temperature case, although its effect is not as pronounced through the range of investigated precooler temperatures as it was in the prior simulations.

4.1.4 Effect of the pump period

In this section, the effect of varying the pump period is analyzed. Figure 4-4a shows the cooling power curves for three different pump periods, while Figure 4-4b plots the ^{3}He molar flow rate variation corresponding to the cooling curves listed in Figure 4-4a. Again, for each of the pump periods studied here, the cooling capacity and ^{3}He molar flow rate dependence on the mixing chamber temperature is unchanged from simulations already studied. Knowing that all other parameters are held constant, the flow rate dependence on the pump period seen in Figure 4-4b is rather straightforward, with reduced pump periods causing increased ^{3}He molar flow rates. This happens because the same amount of thermal energy must be removed from the high temperature cylinder during the pumping-intake process for each of the three pump period cases, but it must be removed faster as the pump period decreases. Increased ^{3}He molar flow rates are the only way to achieve this heightened pace of thermal energy removal.

The cooling curve behavior for the different pump periods is analogous to the curves presented earlier for various cylinder volumes. At high mixing chamber temperatures, the cooling capacity scales with the ^{3}He molar flow rate, whereas the pump periods with lower flow rates have higher cooling capacities at lower mixing chamber temperatures because the recuperator effectiveness dominates at the lower pressure differentials associated with the lower mixing chamber temperatures. The crossover of the 120s and 250s pump period cooling curves at low mixing chamber temperatures is again caused by the cooling regime transition, illustrated in the ^{3}He molar flow rate plots of Figure 4-4b.

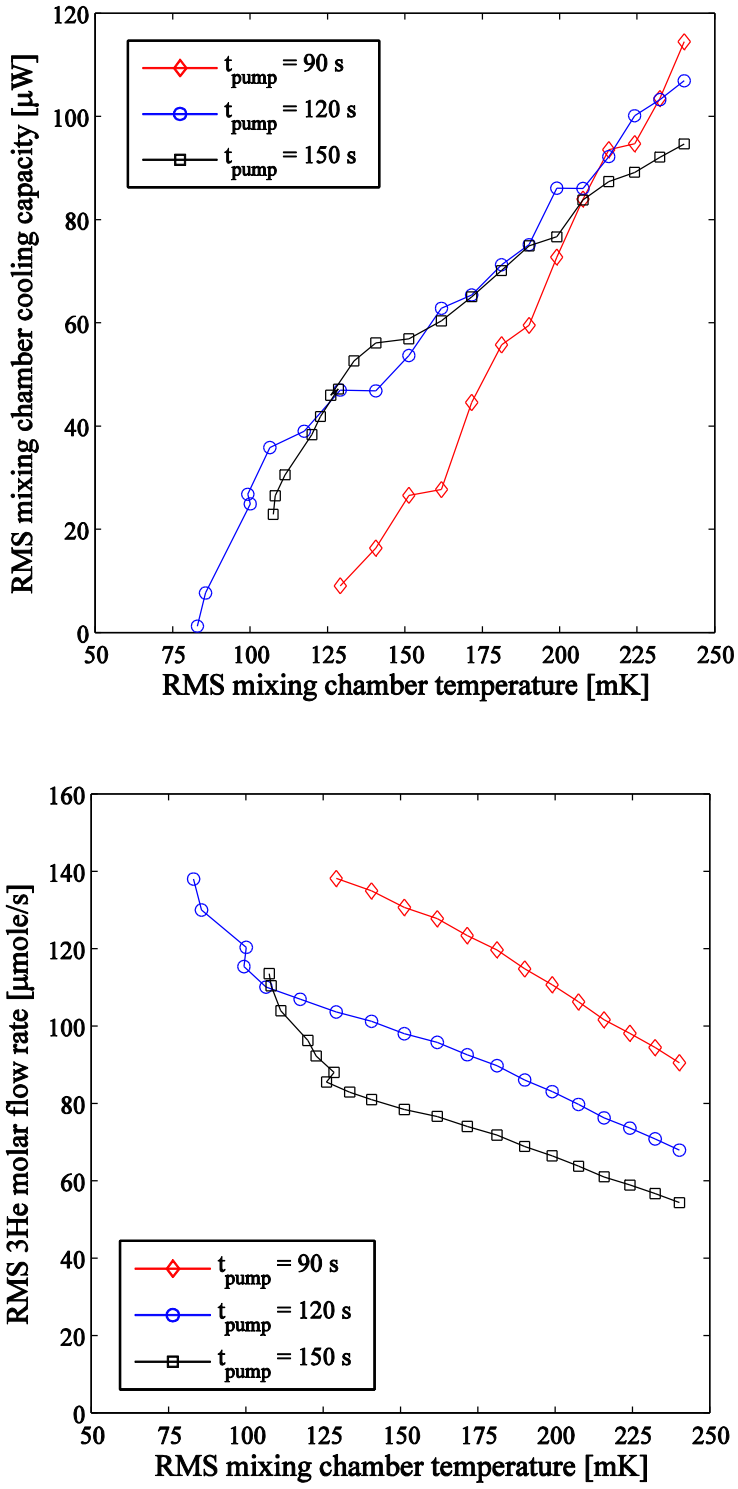

Figure 4-4: (a) RMS mixing chamber cooling capacity and (b) RMS ^{3}He molar flow rate variation with RMS mixing chamber temperature for multiple pump periods and the base parameters given in Table 4-1

4.2 Effect of the recuperator system on the refrigerator performance

At this point, following the analysis of the cooling power and ^{3}He molar flow rate curves for various model parameter combinations, it is clear that the recuperator size plays a critical role in determining the cooling capacities and lowest attainable mixing chamber temperature for a given pump design and operating set point. To illustrate this further, Figure 4-5 shows cooling power curves for various lengths of recuperator I with all other parameters held constant at the base conditions of Table 4-1.

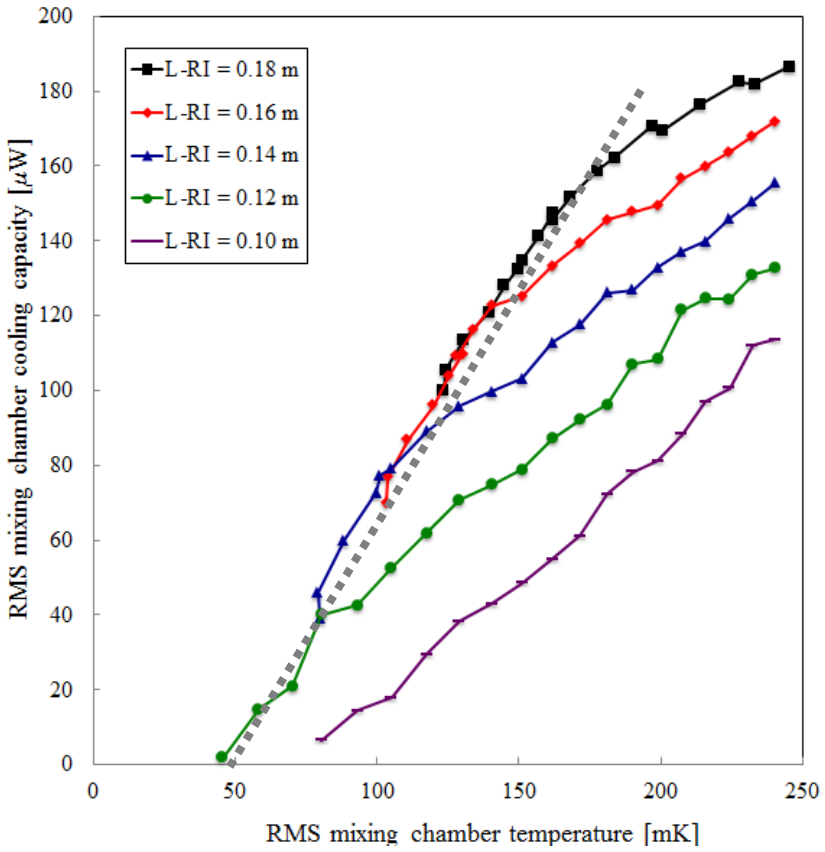

Figure 4-5: RMS mixing chamber cooling capacity as a function of RMS mixing chamber temperature for multiple lengths of recuperator I and the base parameters given in Table 4-1.

The three cooling regimes discussed with the simulation results shown previously are easily observed in the map of cooling power curves displayed in Figure 4-5. To the right of the grey

dashed line, all operating points fall into the cooling regime where some portion of the enthalpy of mixing is needed to cool the incoming high temperature stream in the recuperator; this means that some length of the low temperature recuperator stream experiences two phase flow, and that the mixing chamber cooling capacity is less than the enthalpy of mixing. At the intersection of the grey dashed line with each recuperator's cooling power curve, the enthalpy of mixing is equal to the cooling capacity. In these two regimes, the reported mixing chamber temperature is the saturation temperature corresponding to the cold stream projected ^{4}He chemical potentials at each operating point.

The third cooling regime, where the mixing chamber cooling capacity is augmented by the enthalpy rise (and thus temperature increase) of the single phase superfluid within the mixing chamber, extends linearly for each recuperator length from the cooling power curve intersection with the grey line to the zero cooling capacity mixing chamber temperature. In this region, the cooling power curves for the larger recuperators do not visibly extend all the way down the linear path to the zero cooling capacity mixing chamber temperature because the reported mixing chamber temperature is not the saturation temperature associated with the operating point; rather, the reported mixing chamber temperature is *higher* than the saturation temperature because of the enthalpy rise of the single phase superfluid within the mixing chamber. If the cooling capacity is instead defined as the fraction of cooling provided at the saturation temperature associated with the operating point, the cooling power curves in this region for all recuperator sizes would visibly extend down the dashed line to the zero capacity mixing chamber temperature. The remaining fraction of the mixing chamber cooling capacity, provided by the

enthalpy rise of the single phase superfluid, would need to be provided at higher temperature than the saturation temperature, however.

With this knowledge, Figure 4-5 shows that extending the length of recuperator I increases the cooling capacity for a given design and operating set point if operating in the region to the right of the dashed line. Increasing the recuperator length in this region increases the effectiveness of the heat exchange, in turn requiring less of the enthalpy of mixing to cool the hot stream in the recuperators. With a smaller portion of the enthalpy of mixing needed to cool the hot stream, more is available to contribute to the mixing chamber cooling capacity. Also highlighted here is another important design issue: if undersized, the recuperator can restrict the zero capacity mixing chamber temperature. For the base set of model parameters in Table 4-1 used to compute the curves in Figure 4-5, this critical length for recuperator I is around 0.12 m; at shorter lengths, the recuperator system is too ineffective to operate in the region where the entire enthalpy of mixing goes towards the mixing cooling capacity. Instead, at these short lengths, some fraction must always contribute to the cooling of the hot recuperator stream. For a given set of design parameters and estimated operating set points, the recuperator system should be designed such that the critical size is exceeded so that the recuperator network does not place a lower bound on the zero capacity mixing chamber temperature. In such a case where the recuperators are adequately effective, the lowest attainable temperature is no longer restricted by the recuperator size, but rather by the other design parameters affecting the pressure difference developed over the superleak in the pump.

Before concluding the discussion of the recuperator system, it is useful to briefly discuss the behavior and implications of the temperature and ^{3}He molar concentration profiles that occur within the three recuperators. Figure 4-6 shows such profiles as a function of position from the hot end of the recuperator network, with the vertical lines indicating the transitions between the individual heat exchangers. Profiles are shown for both the hot and cold streams at two different cooling capacities, 7.64 μW (dashed lines) and 100.13 μW (solid lines), using the base set of model parameters given in Table 4-1.

Observe first the temperature profiles in Figure 4-6a, where several interesting observations can be made. Notice that the hot stream always begins its phase separation at a higher temperature than the low stream since it is always at a higher pressure. Since heat must be removed from the hot stream in the phase separation chamber as it increases in ^{3}He molar concentration at constant temperature on its way to recuperator III, the low temperature stream, which in the *single phase* superfluid region in recuperator II, rapidly warms on its way to the pump because it is not constrained to a constant temperature. Also of note in this plot is the pinching of the temperature profiles at the cold end of recuperator III. This is caused by the large discrepancy in capacitance rates between the hot stream, which is nearly pure ^{3}He and thus has a large specific heat capacity, and the cold stream, which has an order-of-magnitude smaller specific heat capacity because it is in the superfluid phase. Oversizing recuperator III thus has no negative effect on the performance of the machine, although it is kept at a reasonable length in the model to speed simulation time and avoid convergence issues.

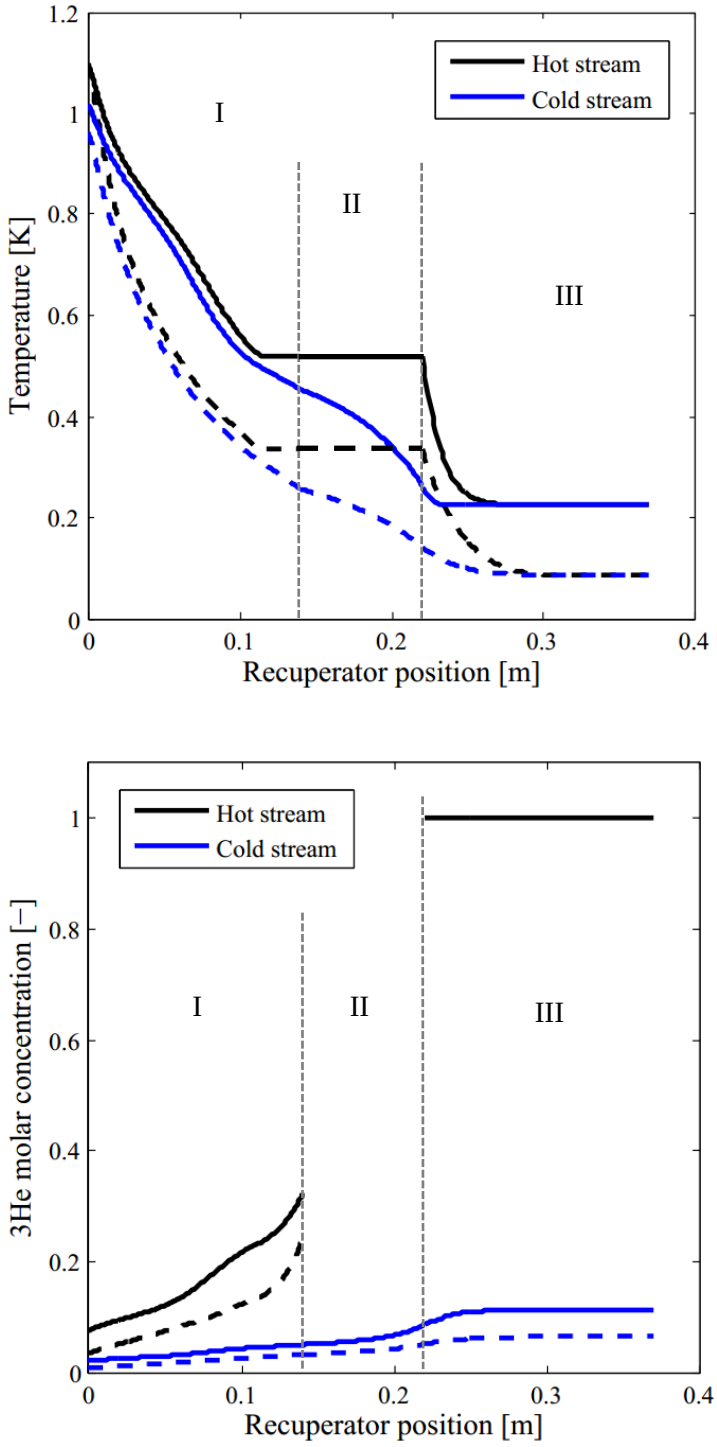

Figure 4-6: (a) RMS temperature and (b) RMS ^{3}He molar concentration profiles for the hot and cold streams in the recuperator system at mixing chamber cooling capacities of 7.64 μW (dashed lines) and 100.13 μW (solid lines) at the base model parameters given in Table 4-1. These two operating points are pulled from the 12 cc pump volume cooling power curves in Figure 4-1. Note that the recuperators are counterflow, with the hot stream flowing towards the cold end and the cold stream flowing to the hot end.

Like the temperature profiles, the ^{3}He molar concentration profiles in Figure 4-6b also illustrate some interesting system behavior. The most striking takeaway from the plot is that, for both cooling capacities, the hot stream undergoes a much larger change in ^{3}He molar concentration over the length of the recuperator system. This is the expected behavior since one purpose of the recuperator network and phase separation chamber is to increase the ^{3}He molar concentration of the hot stream before it arrives at the mixing chamber. Remember here that the ^{3}He molar concentration is not defined as a function of position within the phase separation chamber (the hot stream in section II) for reasons stated in the model development section. Finally, note that the concentration profiles for either stream do not shift much with the change in cooling power.

4.3 Reject heat considerations

With the discussion of the recuperator plots complete, just a few additional, yet important comments are needed to fully characterize the performance of the refrigerator. Figure 4-7 is a plot of the RMS heat rejection to the precooling stage as a function of RMS mixing chamber temperature for different cylinder volumes, obtained from the same simulations used to calculate the cooling power and ^{3}He molar flow rate curves for these same cylinder volumes Figure 4-1. This plot should therefore be taken in context with the discussion of those simulations. Two key observations are made from these curves. First, the reject heat increases as the mixing chamber temperature decreases; this means that the thermal efficiency drops at higher rate as the mixing chamber temperature drops. This is an expected behavior for any refrigerator, which helps affirm the validity of the calculations. Secondly, and perhaps more importantly from a design perspective, the maximum RMS heat rejection load on the precooler never exceeds about 12 mW

for this set of simulations. Such a cooling load is easily achievable by the cryocoolers used to remove this heat from the precooling stage (Jahromi 2011).

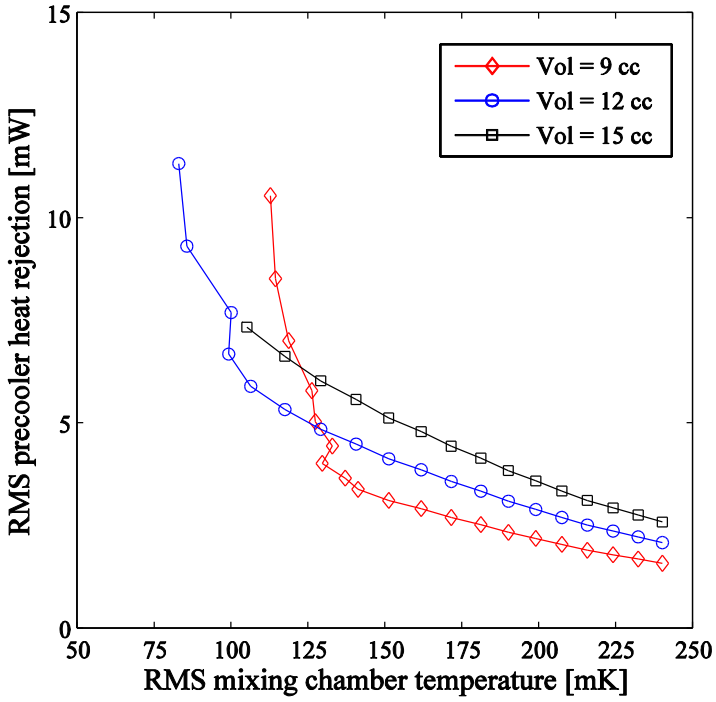

Figure 4-7: RMS precooler heat rejection variation with mixing chamber temperature for multiple cylinder volumes at the base parameters given in Table 4-1

4.4 Superleak pressure differentials induced by the pump

Figure 4-8 shows the pressure differential across the pump superleak as a function of the mixing chamber temperature for the same three cylinder volumes (and simulations) used in the previous plot for the reject heat. As addressed several times prior, the pressure differential decreases as the mixing chamber temperature decreases; this is the key trend responsible for driving the cooling capacity down as the mixing temperature decreases. An interesting note here, which is not true for various values of the other parameters already investigated, is that the pressure difference is

independent of the cylinder volume for a given mixing chamber temperature. This is because the porosity is held constant for each of the volumes shown here. The deviation from this behavior at low mixing chamber temperatures is again the result of the cooling regime switch and the definition of the mixing chamber temperature – if the pressure difference is plotted against saturation temperature, instead of the maximum mixing chamber temperature, corresponding to each operating points, there would be no variation at the low mixing chamber temperatures.

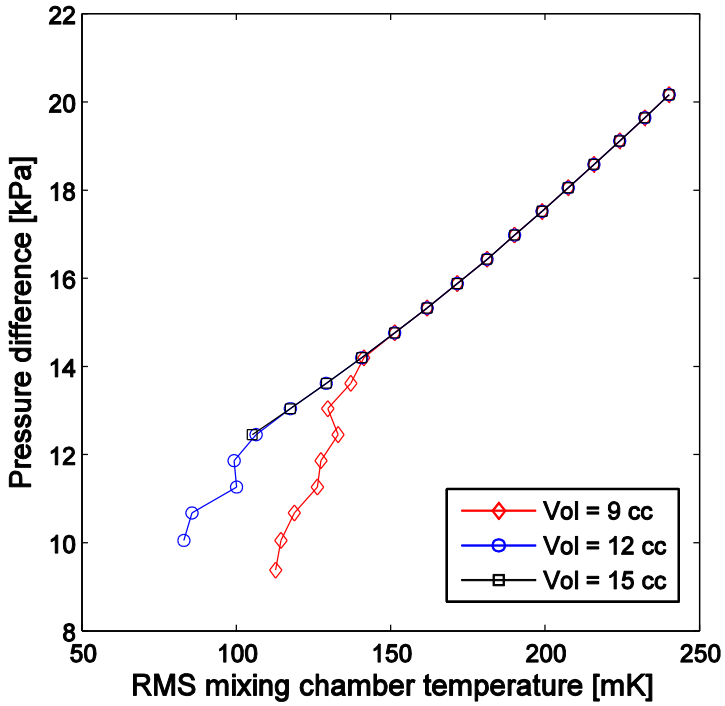

Figure 4-8: RMS pressure differentials for multiple cylinder volumes at the base parameters given in Table 4-1.

4.5 Estimation of the minimum required ^{3}He molar charge

Finally, it is critical for both cost and experimental reasons to obtain an estimate for the amount of ^{3}He needed to charge the system if the cooling capacities reported in the previous sections are to be achieved. Figure 4-9 shows the estimated required ^{3}He molar charge as a function of

mixing chamber temperature, corresponding to the same simulations for the same cylinder volumes used in the last two plots. This minimum ^{3}He molar charge is calculated by first estimating, and then summing, the amount of ^{3}He in all of the system components at each operating point. Assumptions are made that the ^{3}He-concentrate phase occupies no volume in both the phase separation chamber and the mixing chamber, which gives a minimum estimate of the amount of ^{3}He stored in each of those components. The general trend of the curves in Figure 4-9 show that the required initial ^{3}He concentration decreases as the mixing chamber temperature decreases for each of the volumes investigated. This is because the temperature, and thus ^{3}He molar concentration, of the phase separation chamber increases as the mixing chamber temperature increases. This behavior was shown previously by the ^{3}He concentration profiles at different cooling loads in Figure 4-6b. Slightly different charges are needed for the different cylinder volumes because the concentration profiles within the recuperators shift slightly for each case. To allow the operation of the machine over the entire range of mixing chamber temperatures of the curves in Figure 4-9, the machine must initially contain the maximum charge shown – about 18 percent ^{3}He. Should the cooling capacity and mixing chamber temperature decrease when the machine is charged to this high concentration, the additional ^{3}He would sink to the cold end of the machine, being stored in some increased volume of ^{3}He-concentrate within the mixing chamber or phase separation chamber.

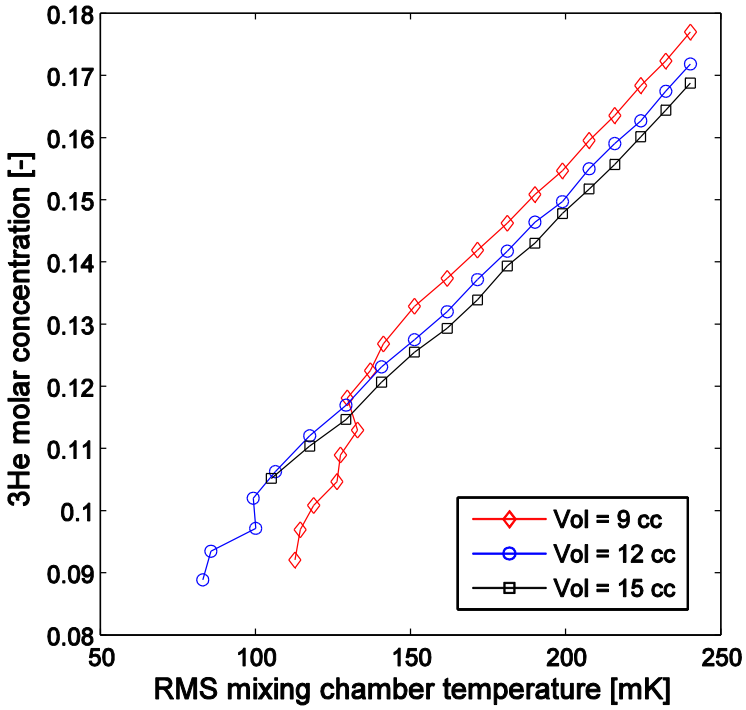

Figure 4-9: Estimated minimum ^{3}He molar concentration charge needed for different cylinder volumes at the base parameters given in Table 4-1.

4.6 Conclusions

Using the cold cycle ^{3}He-^{4}He dilution refrigerator model developed in this thesis, initial proof-of-concept simulations provide strong evidence that the proposed design is indeed capable of providing refrigeration at temperatures below 100 mK. The refrigerator performance has been characterized in detail, with cooling power and ^{3}He molar flow rate curves presented over a range of mixing chamber temperatures for various sets of design and operating parameters. With an adequately designed recuperator network for the base set of model parameters used in the simulations, results show that about 80 μW of cooling can be expected at a mixing chamber temperature of 100 mK. This is a significant increase over the 20 μW at 100 mK for a typical laboratory helium dilution refrigerator as cited by Enss (2005) and Lounassma (1974). It is likely

that additional optimization of the design and operating parameters – an analysis that is beyond the scope of this work – would result in further performance gains.

4.7 Recommendations for future work

Many opportunities exist to enhance the accuracy of the cold cycle ^{3}He-^{4}He dilution refrigerator model developed in this work. Following is a list of suggestions to improve the model if greater accuracy is required for future simulations. Although the benefits of the ideas presented here vary, and some may be more difficult to implement than others, they are listed in no particular order.

1. Use a more accurate equation of state for ^{3}He-^{4}He solutions. The thermodynamic properties used in this work originate from the Chaudhry (2009) combined equation of state, which is pieced together from a small sample of experimental measurements. Developing a highly accurate state equation is unlikely, however, due to the difficulty (and expense) in obtaining accurate thermodynamic data over the entire operating range of the cold cycle dilution refrigerator.
2. Increase the property table resolution. The Matlab code uses interpolation to find ^{3}He-^{4}He properties from tables created using the Chaudhry equation of state. This strategy significantly lowers simulation times but limits the resolution of property data to the step sizes chosen for table creation. Increasing the property table resolution will make the model more accurate (and the cooling power curves smoother) but will also increase simulation times. A rough compromise on this issue was attempted for the simulations in this work, but some further optimization on this issue could be achieved.

3. Optimization of the overall design. As mentioned previously, a detailed parametric study could be completed to find the best pump design by varying all of the relevant parameters within the design constraints of the system. This work did not attempt this due to time constraints.

4.8 References

Enss, C. and Hunklinger, S., Low temperature physics, Springer, New York, 2005.

Jahromi, A., Development of a 1 K facility and modeling of a superfluid magnetic pump with no moving parts, Master's Thesis, University of Wisconsin – Madison, 2011.

Lounasmaa, O., Experimental principles and methods below 1 K, Academic Press, 1974.